TESLA-FEL 2008-04

Universität Hamburg

Investigations into the FLASH Infrared Undulator as an Electron Beam Diagnostic Tool

Diploma Thesis

submitted to
Institut für Experimentalphysik
Universität Hamburg

by
ARIK WILLNER

Hamburg
April 2008

HELMHOLTZ GEMEINSCHAFT

Dedicated
to
My dear Father

Abstract

The operation of a free electron laser in a wavelength regime down to 6 nm requires a high electron beam quality. Thus, the electron beam diagnostics, especially the determination of the electron bunch length which defines the peak current, is an important task.
The Free-Electron-Laser in Hamburg (FLASH) at DESY has been complemented by an electromagnetic infrared undulator as a new tool for analysing the longitudinal profile of the short electron bunches characteristic for FLASH using coherent diagnostic techniques. This undulator has a maximum K-Value of 44 corresponding to a maximum wavelength of 200 µm at an electron energy of 500 MeV. For the characterization of the emitted radiation and for the analysis of correlations between machine or undulator parameters and undulator spectra, an experimental set-up has been developed and installed in the FLASH Experimental Hall containing a dispersive spectrometer as a main instrument. The spectrometer is designed for THz spectra using reflective blazed gratings as dispersive elements and a pyroelectric detector.
The final goal is the reconstruction of the longitudinal bunch shape by tuning the undulator through the wavelength range of the electromagnetic device and measuring the intensity of the infrared radiation. The measurements discussed in this thesis are important preparative investigations for this diagnostic technique.

Zusammenfassung

Der Betrieb eines Freien-Elektronen-Lasers bei kurzen Wellenlängen erfordert eine hohe Strahlqualität eines Linearbeschleunigers. Somit ist die Diagnose u.a. für die Bunchlänge, welche den Spitzenstrom bestimmt, ein wichtiges Feld innerhalb der Beschleunigerforschung. Der Freie-Elektronen-Laser in Hamburg (FLASH) am Deutschen-Elektronen-Synchrotron (DESY) wurde durch einen elektromagnetischen Infrarot-Undulator erweitert, mit dem das longitudinale Profil der für FLASH charakteristisch kurzen Elektronenpakete mit Hilfe von Techniken der kohärenten Diagnose untersucht werden soll. Dieser Undulator hat einen maximalen K-Wert von 44, was einer maximalen Wellenlänge von 200 µm bei einer Elektronen-Energie von 500 MeV entspricht. Für die Charakterisierung der emittierten Strahlung und für die Untersuchung der Korrelation zwischen Maschinen- bzw. Undulatorparametern und Undulatorspektren wurde ein Experiment in der FLASH-Experimentierhalle entwickelt und aufgebaut, welches ein dispersives Spektrometer als hauptsächliches Instrument enthält. Dieses Spektrometer ist mit 'Blaze'-Gittern und einem pyro-elektrischen Detektor speziell für THz- Strahlung entworfen worden.
Das Fernziel ist die Rekonstruktion des longitudinalen Bunch-Profils allein durch das Durchfahren des Wellenlängenbereichs des elektromagnetischen Undulators und jeweiliger Intensitätsmessung. Die in dieser Arbeit diskutierten Messungen sind wichtige vorbereitende Untersuchungen für diese Art der Diagnostik.

Contents

1 Introduction **3**
1.1 FLASH . . . 6
1.1.1 Laser driven RF-gun . . . 6
1.1.2 Superconducting linear accelerator (linac) . . . 7
1.1.3 Bunch Compressors . . . 8
1.1.4 FEL undulator . . . 11
1.1.5 Photon beamlines and diagnostics . . . 11
1.2 Longitudinal Bunch Diagnostics . . . 11
1.2.1 Time-Resolved Methods . . . 11
1.2.2 Frequency-Domain Techniques . . . 13
1.3 Different types of coherent radiation . . . 16
1.3.1 Coherent Synchrotron Radiation (CSR) . . . 16
1.3.2 Coherent Transition Radiation (CTR) . . . 17
1.3.3 Coherent Diffraction Radiation (CDR) . . . 18

2 Undulator **19**
2.1 Basic Concepts . . . 19
2.2 Infrared Undulator at FLASH . . . 25
2.2.1 Design of the IR Undulator . . . 25
2.2.2 Magnetic Measurements in Dubna and Hamburg . . . 27
2.2.3 IR Undulator as Coherent Diagnostic Tool . . . 30
2.3 Further Application of IR Undulator . . . 34

3 Design and Construction of the Experiment **36**
3.1 Infrared Beamline . . . 36
3.2 The Spectrometer . . . 39
3.2.1 The Gratings . . . 40
3.2.2 The Pyroelectric Detector . . . 42
3.2.3 The Final Spectrometer Design . . . 43
3.3 The Optics Calculations . . . 46
3.3.1 Gaussian Optics . . . 47
3.3.2 Undulator radiation as a laser-like beam . . . 51
3.3.3 *ZEMAX* as Simulation Tool . . . 53
3.3.4 Optical Design . . . 54
3.4 The Experimental Station . . . 61

4 Measurements and Results **66**
4.1 Commissioning of IR Undulator . . . 66
4.2 Spectral Investigations into the IR undulator . . . 74

4.2.1 Wavelength calibration 74
4.2.2 Wavelength shift 75
4.2.3 Multiple peak spectra 79
4.2.4 Full scan 85
4.2.5 Background studies 88
4.2.6 Influence of correction coils 90
4.3 Beam Profile Measurements 90

5 Conclusion and Outlook **93**

A Appendix-
Response measurements of steerer magnets **95**

B Appendix-
Magnetic field measurements of undulator coils **97**

C Appendix-
Transmission curve of polarizer P03 **99**

References **100**

1 Introduction

Investigation of matter with high resolution obtained a new impact, when physicists discovered that synchrotron radiation, the 'wasted' energy at accelerators, provides a useful tool, for example, for solid state physics and medical or chemical experiments. In the beginning, only synchrotron light produced by the bending magnets was used. Later, one started to construct explicit synchrotron light sources with an improved radiation quality by using wigglers and undulators, which are devices generating an alternating transverse magnetic field [1]. A further step towards high brilliance light sources was the invention of Free-Electron-Lasers (FELs).

The radiation emitted by electrons during the passage of a magnetic device like undulators is based on spontaneous uncorrelated radiation of all the electrons within a bunch. In this case the emitted radiation power is N times the power of a single electron with N being the number of electrons within the bunch [2]. In order to increase the power and the coherence of the radiation, the electrons have to be forced to radiate coherently by compressing them into a length small compared to the emitted wavelength. To produce coherent radiation in wavelengths in order of nanometers, one needs to compress the bunch length to the same scale, which is not possible by magnetic bunch compression [3]. Thus, instead of compressing a bunch the Free-Electron Laser (FEL) imprints a modulation into the bunch in longitudinal phase space. This process is called *micro bunching* and it leads to coherent emission, because these micro bunches within the electron bunch are small compared to the wanted wavelength. The FEL is an undulator which forces the particles on an oscillatory path by its sequence of alternating magnetic fields (see Section 2). Following this trajectory, the electrons radiate in a narrow bandwidth with a wavelength in the first harmonic being

$$\lambda_{ph} = \frac{\lambda_U}{2\gamma^2}\left(1+\frac{K^2}{2}\right) \tag{1}$$

where λ_U is the undulator period, $\gamma = E/(m_e c^2)$ the relativistic factor and $K = eB_0\lambda_U/(2\pi m_e c)$ the undulator parameter, B_0 being the peak magnetic field. This emitted radiation interacts with the electrons again inducing the periodic charge density modulation in the electron bunch with the period given by the resonance wavelength λ_{ph}. When this micro-bunching structure is once established, most of the electrons start to radiate coherently with the wavelength λ_{ph}. As a consequence, the intensity increases over the length of the FEL-undulator. FELs working with the spontaneous undulator radiation overlapping with the electrons are so-called *Self-Amplified Spontaneous Emission (SASE)*-FELs.

One divides FELs into two categories: *Low-gain FELs* and *high-gain FELs*.

In low-gain FELs the radiation is enhanced only marginal during one passage. An optical cavity is used to amplify the radiation. The principle is similar to laser-cavities, where the light gets amplified by being reflected bidirectionally by mirrors. This method works well for the infrared, visible and soft ultraviolet radiation. For wavelength shorter than that, no suitable mirrors necessary for the optical cavity are available. In this case, a high-gain FEL is the only possible solution. The lasing is achieved within a single passage of the electron beam through the undulator and thus, no mirrors are needed. In the end, free-electron-lasers are powerful light sources by producing strongly coherent light with a high brilliance.

The Free-Electron-Laser in Hamburg (FLASH) is a high-gain FEL user facility at DESY[1] operating in the photon wavelength range from vacuum ultra-violet to soft x-rays. It is driven by a superconducting linac and the generation of the FEL radiation is based on the SASE process. In autumn 2007 FLASH reached its design goals being an electron energy of 1 GeV and lasing down to 6.5 nm photon wavelength [4].

For a high-gain FEL like FLASH the following parameters of the electron beam are of great importance: First, the energy of the electron beam defines the produced photon wavelength assuming a fixed gap of the undulator. Thus, the photon wavelength can be tuned by changing the electron energy. Secondly, the longitudinal charge distribution within the bunch and the transverse electron beam size are crucial factors within the lasing process of FELs. This is based on the dependence of the *FEL-gain* on the peak current and on the transverse beam size. Having a gain in the FEL undulators of

$$G(z) \propto \exp\left(\frac{z}{L_G}\right)$$

with z being the longitudinal position, the dependence on the beam parameters is contained within the *gain length* L_G which is defined as

$$L_G = C\gamma\left(\frac{\sigma_t^2}{I_0}\right)^{1/3}$$

where C is a constant determined by the undulator, γ the relativistic factor, σ_t the transverse RMS size of the bunch and I_0 the peak current of the charge distribution. Therefore, a small beam size (or emittance) and a high peak current are required to obtain a short gain length necessary for high-gain FELs.

As seen above, the peak current or longitudinal charge distribution is an important electron beam parameter for the lasing process of high-gain FELs. In

[1] Deutsches-Elektronen-Synchrotron

order to obtain the required high peak current, the electron bunch needs to be compressed. For a proper analysis of the FEL process and operation, longitudinal bunch diagnostics with high resolution for sub-picoseconds bunches are required. Many different techniques investigating the bunch longitudinally using time- and frequency-resolved methods have been developed. For the time-resolved diagnostics there are, for example, streak cameras using optical radiation [5] or longitudinal phase space tomography tilting the phase space distribution in a dispersive element and measuring the resulting projection [6]. In the frequency domain, techniques using coherent radiation produced by a bunch in the chicane [7] or with screens are used [8]. Even though the design performance of FLASH was reached without adequate longitudinal diagnostic tools, it is of great importance to investigate the longitudinal bunch structure to support the commissioning of future FELs and to obtain a further understanding of the processes within a FEL.

Many groups are involved in longitudinal diagnostics inventing and investigating new diagnostic techniques and methods. Despite the progress in this field, none of the already used techniques provides all information needed for adequate structure analysis [9].

Since summer 2007 there is a new tool for longitudinal bunch diagnostics at FLASH. Right after the FEL, an electromagnetic infrared (IR) undulator was installed producing radiation from 1-200 µm for an electron beam energy of 500 MeV [10]. The aim is, that one can reconstruct the longitudinal bunch profile by tuning the undulator to certain wavelengths and measuring the intensity at these points. The advantage compared to the broad band techniques is, that the IR undulator can be tuned to a certain wavelength with a small band width.

The subject of the thesis was on the one hand the development of an experimental setup for spectral investigations of the IR undulator. Part of this development was the design and construction of a spectrometer based on the concepts from [11] as well as the design and construction of an experimental station in the FLASH experimental hall containing this spectrometer. On the other hand, the commissioning of the IR undulator and first spectral investigations of the produced radiation formed the second part of the work done for this thesis.

The thesis is subdivided into six chapters. In the first, a general introduction to the FLASH facility, the task of bunch length and the question of coherent diagnostics is given. The second chapter deals with the undulator: An introduction to the basic concepts of undulators and wigglers is followed by a detailed description of the FLASH infrared undulator and its further application to electron beam diagnostics. As third part of the thesis, the design and construction of the spectrometer and the experimental setup in the experimental hall will be described accurately before the measurements and results of the undulator commissioning and spectral investigations will be presented in the fourth chapter. The fifth chapter deals with the future use of the experimental station in the FLASH hall and gives a general

outlook concerning coherent bunch diagnostics with the infrared undulator.

1.1 FLASH

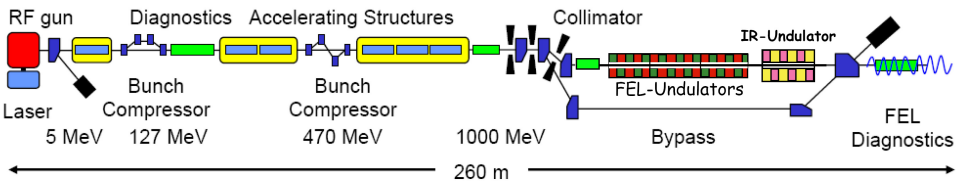

Figure 1: Schematic layout of FLASH - not to scale.

The Free-Electron-Laser in Hamburg (FLASH) is a high-gain FEL based on the SASE process. It consists of a laser driven RF-gun[2], six superconducting accelerator modules, two magnetic chicanes as bunch compressors, an undulator section and photon beamlines. A schematic layout is shown in figure 1.

1.1.1 Laser driven RF-gun

The first part of the accelerator is the injector system: a laser driven RF-gun followed by the first acceleration module [12]. It provides a rapid acceleration from the cathode and allows to generate a low emittance beam from the source with transverse normalized emittance smaller than 2 mm mrad for a charge of 1 nC [12]. This is crucial because low emittance is required for the FEL amplification process. The RF-gun is a 1.5 cell normal conducting L-band cavity with a resonance frequency of 1.3 GHz. The cavity is powered by a 5 MW klystron over a longitudinal coaxial RF coupler. A Cs_2Te (Cesium-Tellurid) photo cathode which is inserted in the RF gun backplane is used as electron source. The cathode can be changed if required [13]. A pulsed, transversally and longitudinally Gaussian-shaped laser, which is synchronized to the 1.3 GHz RF of the accelerator, interacts with the cathode and releases electrons due to photo-electric effect. The laser is based on a Nd:YLF mode-locked pulse train oscillator. The gun cavity then accelerates the bunch to a beam energy of 5 MeV. In order to reduce space charge induced emittance growth, the electron beam is focused by a solenoid magnet. This first section defines the initial conditions which are imprinted in the bunch for the whole acceleration and thus also in the radiation produced by the bunch in the FEL undulators.

[2] **RF**=**R**adio **F**requency

The combination of fast acceleration and the focusing elements counteract the emittance blow-up by space charge forces which are strong at low electron energy (proportional to $1/\gamma^2$) [14]. Choosing the right rf phase, the electrons released from the cathode undergo their first modulation due to velocity distribution within the bunch leading to a reduction of the bunch length. The effect is that leading electrons are less accelerated than trailing ones, because they see different parts of the oscillating electric field in the gun cavity. This is a technique for bunch compression only applicable in the low energy range, like in the gun section, because afterwards the electrons rapidly reach almost the speed of light, so that there is no difference in velocity within the bunch anymore.

The typical charge per bunch is 0.5-1 nC. The system produces bunch trains up to a length of 800 µs with a repetition rate of max. 5 Hz. The number of bunches is selectable from 1 to 800. The repetition rate of the bunching is usually 1 MHz, but frequencies of 500 kHz, 200 kHz and 100 kHz are also possible.

1.1.2 Superconducting linear accelerator (linac)

The linac of FLASH consists of six superconducting accelerator modules which are hold at a temperature of 2 K by bath-cooling with superfluid helium within a cryo-module. Each module has eight TESLA type cavities with nine superconducting niobium cells each with a resonant frequency of 1.3 GHz [15]. After the RF gun the beam is matched into the first superconducting acceleration module. This module boosts the electron bunch to an energy of ≈130 MeV before it enters a magnetic chicane, the first *bunch compressor* (see section 2.1). To avoid strong transverse focusing leading to disturbing space charge effects, the gradient of the first four cavities are operated with a moderate gradient whereas the following four structures have a higher gradient with 20 MV/m in average. The moderate gradient is chosen due to emittance damping scheme which means, that it provides the best balance between emittance growth due to space charge effects and increase of emittance due to lack of sufficient acceleration [12].

The first magnetic chicane which follows ACC1 (see 2.1) is located in front of two further accelerator modules increasing the beam energy up to approximately 470 MeV. After the second bunch compressor, another three accelerator modules are situated. The maximum achievable beam energy after the last modules is 1 GeV[3]. FLASH can be operated with electron beam energies between 450 MeV and 1000 MeV depending on the photon wavelength requested by FEL users.

[3] All new data about the actual status of FLASH after the shut down in summer 2007 are taken from [4].

1.1.3 Bunch Compressors

In order to achieve a peak current exceeding 1 kA, as required for the lasing process, a compression of the bunch using magnetic chicanes is done at FLASH [14]. In addition to that, the beam transverse normalized slice emittance and the final energy spread should not exceed a limit of 2.0 mm-mrad and $\approx$ 1 MeV, respectively. These conditions put a high demand on the bunch compression system. The electron bunch leaves the injector section with a length approximately 40

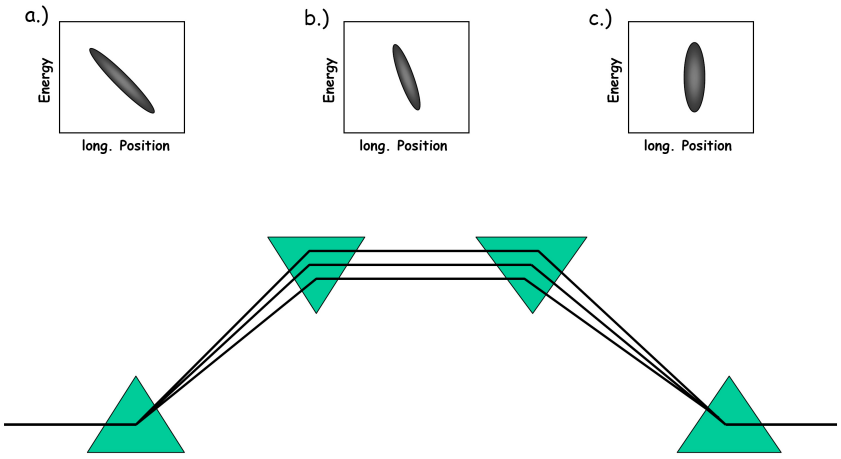

Figure 2: The first bunch compressor. The bunch arrives with an energy chirp (a). After the first bending magnets the electrons with a higher energy have a different trajectory than the ones with lower energy which results in a compression (b). After the chicane the bunch is compressed to approximately 200 µm (c).

times longer than required by the SASE process. This is due to the fact, that the transverse projected emittance must be small at the front-end of the injector. This long bunch leaves the first accelerator module with a non-linear longitudinal phase space distribution [16]. The longitudinal phase space in accelerator physics is defined as the coordinate system spanned by the longitudinal position and the energy. It is planned to install a third harmonic cavity behind the first module in order to make the phase space distribution linear. This would avoid the resulting leading spike in the longitudinal density distribution or peak current after the first compression.

The compression is done by two magnetic chicanes. To get the best compression performance for a femtosecond FEL mode, the choice of chicane position

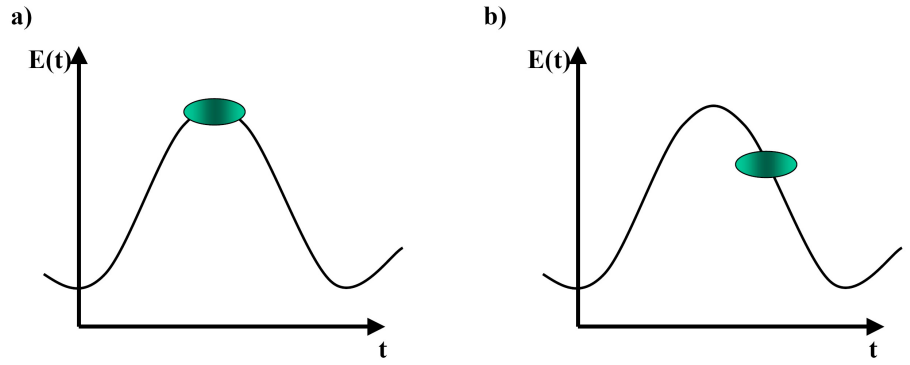

Figure 3: a) on-crest drive of the linac b) off-crest mode of the module

(in terms of beam energy), energy spread, RF phase of preceding linacs and the bending angle of the dipoles are crucial.

The first chicane (see figure 2) is placed after the first acceleration module ACC1 where the beam has an energy of 130 MeV. The compressor consists of four dipole magnets. The bunch is compressed longitudinally only, when ACC1 is operated *off-crest*. If one considers the electric field in the module being a sinewave, then *on-crest* means that the center of the bunch is on the top of the wave (figure 3a). Accelerating electrons off-crest implies that the phase of ACC1 is changed so that the center of the bunch is on the sloping part of the wave (figure 3b). Using the negative slope after the crest (timewise), electrons at the tail get more energy than at the leading ones [14]. This leads to an energy-dependent path length variation within the magnetic chicane. Electrons with higher energy (at the tail) have a shorter path through the chicane than the low-energy electrons at the head. The result is a compression down to an rms length of 200 µm and a leading peak in the longitudinal structure due to non-linearity [17]. In figure 2 the process in the first compressor is illustrated. Vertically, the bunch is focused by the effect of weak focusing characteristic for dipoles.

The second bunch compressor is located after the accelerating section ACC2/3, where the electron energy is 470 MeV. It is a 4-bend S-shaped chicane (figure 4). The energy spread is provided by the off-crest operation of the linac modules 1 and 2/3. The bending angle can be varied ($1.5° < \Theta < 5.4°$) so that several combinations of acceleration phase and compression factor are possible [14]. After this chicane the bunch has its final rms length of around 50 µm necessary for the lasing process.

The different shape of the second compressor is due to a multi-particle effect called *Coherent Synchrotron Radiation (CSR)*. The difference to the first chicane is, that at its location the bunch is much shorter [18, 14]. The field emitted at a

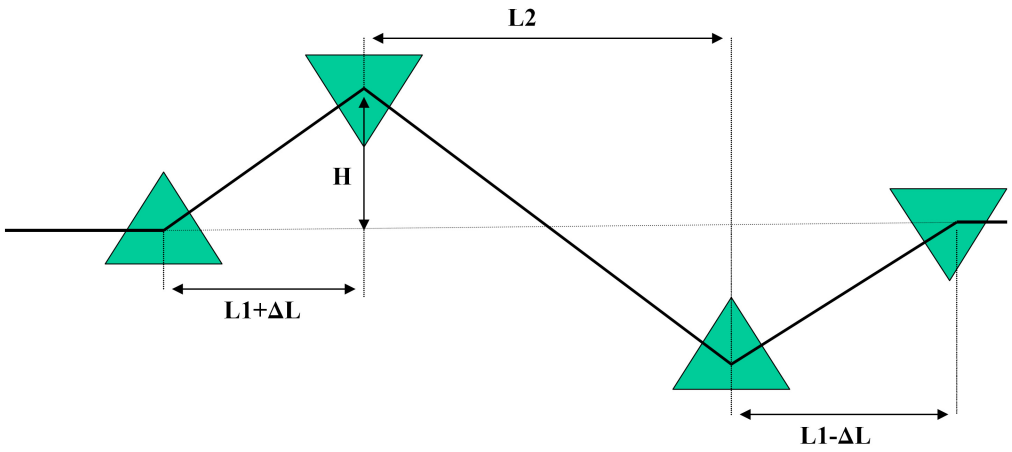

Figure 4: Sketch of the S-chicane of the second bunch compressor.

certain time can overtake the bunch by traveling with the speed of light along a chord whereas the electron beam has a velocity with β being only close to unity and travels along an arc. Thus, this radiation can interact with electrons in the head of the bunch. This effect becomes important when the path in the bending magnet is comparable with the so-called *overtaking length*

$$l_o = (24\sigma_z\rho^2)^{1/3}$$

where σ_z is the rms bunch length and ρ the bending radius. Additionally, the radiated CSR power scales like $1/\sigma^{4/3}$ and thus the shorter bunch length at the second bunch compressor compared to the first compressor has an impact on the emittance. The CSR field emitted on a curved trajectory in the second compressor induces energy offsets in the dispersion section which is followed by an emittance growth. The only way to reduce the total emittance is the reduction of the compression factor which would have an increasing energy spread as unwanted side effect. To balance these two counteracting phenomena, the idea of an s-shaped chicane was invented [18]. A minimum for the slice emittance is obtained with a converging beam having its waist close to the third and fourth dipole. The two inner dipoles of opposite deflection provide the main advantage of a s-shaped chicane compensating each other's effect on the correlated emittance. An optimization of this compensation is reached by moving these two magnets both towards the end of the chicane (along the accelerator axis) by a length ΔL (figure 4). Thus, the compression factor of the second dipole, where only a weak effect from CSR occurs because of longer bunch length, increases and the factor of the third magnet

producing more CSR decreases. The total compression factor of the second compression system remains constant over the whole length. Even though the dipole strengths are tunable for varying the compression factor, it is more convenient to change compression by tuning the phases of ACC1 and ACC2/3 [16].

1.1.4 FEL undulator

FLASH is operated as a high-gain FEL, which leads to a long undulator system. Six undulators with a length of 4.5 m each comprise the FEL system. They consist of permanent NdFeB magnets with a gap size of 12 mm producing a peak magnetic field of 0.48 T. The undulator period is designed to be 27.3 mm.

1.1.5 Photon beamlines and diagnostics

After the FEL undulators photon beamlines and diagnostics are installed. The first device is the new infrared undulator which will be discussed later in more detail. The undulator is followed by the photon beamlines transporting the photons into the experimental hall outside the tunnel. In between there are photon diagnostic stations. Three separate photon beamlines are installed: The vacuum ultra-violet (VUV) beamline transports the FEL radiation to user experiments situated in the experimental hall. Secondly, there is the synchrotron light beamline, which transports the light from the last dipole magnet to the hall. Finally, a new infrared beamline is installed transporting the infrared light from the new undulator to several diagnostic stations (see section 3.1).

1.2 Longitudinal Bunch Diagnostics

As discussed above, the peak current within an electron bunch is an important parameter for the lasing process. Therefore, the investigation into the longitudinal charge distribution along the bunch is of great interest. Many different techniques have been used or are currently under development. However, no individual technique provides all the information that is needed. Thus, several methods for longitudinal diagnostics are often used in parallel [9]. In this subsection, a few examples of different approaches and a description of the ideas behind coherent diagnostics will be discussed.

1.2.1 Time-Resolved Methods

One technique to measure bunch lengths in the time regime uses a *streak camera* and optical radiation produced by the electron beam [5]. A streak camera provides

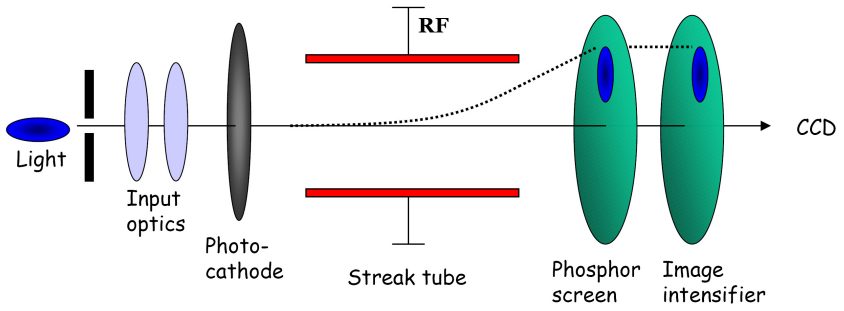

Figure 5: The principle of a streak camera measuring bunch lengths.

a convenient way to measure the electron bunch length in the sub-millimeter-regime (≈200 µm). The working principle of a streak camera is sketched in figure 5. The light pulse arrives at a horizontal slit which has the function to reduce either the horizontal or vertical transverse dimension of the image. After passing input optics, the pulse impinges on a photo cathode. The incident light produces photo electrons whose distribution is proportional to the intensity of the incoming light pulse. After the cathode there is a steak tube, in which the electrons get accelerated and deflected transversally. This deflection is dependent on the arrival time of the electrons into the tube and gives thus a direct measurement of the time structure of the light pulse, which is proportional to the time structure of the electron bunch generating this light pulse. At the end, the electrons are again converted into photons on a screen, whose intensity gets amplified before being recorded by a CCD camera. The disadvantages of such a device are an explicit limit in resolution and the high costs.

Another technique is the use of a transverse deflecting cavity. The electron bunch passes through an rf-structure in which the bunch is deflected by an electric and magnetic field in such a way, that 'top-view', i.e. longitudinal, pictures of the electron bunch can be visualized on a screen. The electrons are deflected transversely with a strength proportional to their longitudinal offset from the bunch center and thus proportional to their arrival time. This leads to a tilt of the bunch and therefore, the longitudinal-transverse projection is observable. The longitudinal bunch profile becomes visible by using an *Optical Transition Radiation* screen (OTR). At FLASH the resolution of this technique is limited to 26 µm [19]. Another disadvantage is that for accurate measurements a special beam optics is needed, and therefore bunch length measurements cannot be performed parasiticly

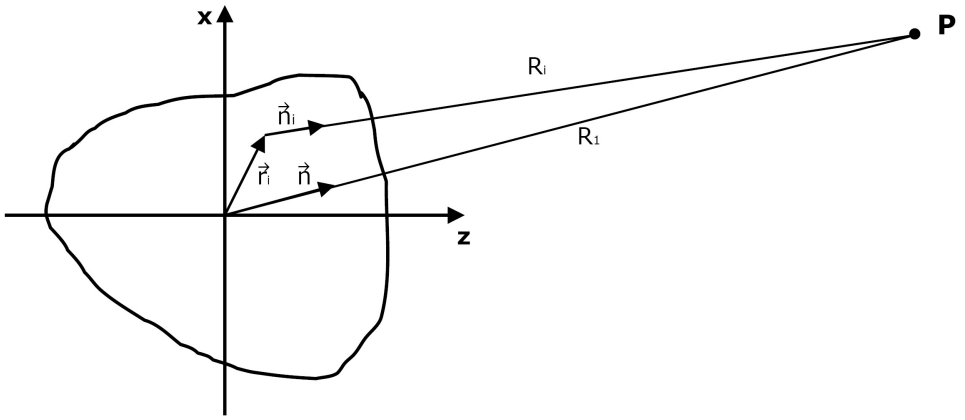

Figure 6: An arbitrary bunch profile with a reference electron sitting in the center. The distance of observation is large compared to the bunch size. In this far-field approximation the two vectors $\vec{n}$ and $\vec{n}_i$ are almost parallel.

to normal beam operation. Nevertheless, very useful results have been obtained using this technique [19, 20].

The third time-resolved method is longitudinal phase space tomography. The idea of tomography is to reconstruct a distribution in a n-dimensional space by combining projections from a (n-1)-dimensional subspace. The longitudinal phase space is spanned by the energy and the longitudinal position. Thus, the input for the reconstruction is the projection onto the energy axis, which can be realized by implementing an energy chirp within a cavity (off-crest operation) and measuring the energy profile with a magnetic spectrometer [6].

1.2.2 Frequency-Domain Techniques

In the case of FLASH, structures well below 30 µm have to be resolved. When the wavelength is comparable to the bunch length or longer, the spectral intensity is strongly enhanced by the effect of coherence. This means, that electrons within a bunch radiate in phase and thus the light waves from each electron interfere constructively. The following derivation of the principles of coherent diagnostics are taken from [21] and [22].

Let us consider a charged particle in the center of mass system of a bunch at the position $r = 0$ (figure 6). The distance to the observation point (for example to the detector) is long compared to the size of the bunch. The reference electron emits the electric field $\vec{E}_1$ with the pulse energy of U_1. The considered bunch contains

N electrons. Thus, the electric field for the bunch is just the superposition of all the single fields

$$\vec{E}(t) = \sum_{i=1}^{N} \vec{E}_i$$

The spectrum is obtained with the Fourier transform

$$\vec{E}(\nu) = \int_{-\infty}^{\infty} \vec{E}(t) e^{-2\pi i \nu t} dt$$

One assumes that all the N particles radiate the same electric field except for time-delays Δt_i caused by their spatial distribution, which defines a far-field condition, where the distance between observation point and radiation origin is large compared to the size of the bunch. The Fourier transform thus becomes

$$\begin{aligned}
\vec{E}(\nu) &= \int_{-\infty}^{\infty} \sum_i \vec{E}_i(t) e^{-2\pi i \nu t} dt = \sum_i \int_{-\infty}^{\infty} \vec{E}_1(t + \Delta t_i) e^{-2\pi i \nu t} dt = \\
&= \sum_i \int_{-\infty}^{\infty} \vec{E}_1(\tilde{t}) e^{-2\pi i \nu (\tilde{t} - \Delta t_i)} dt = \sum_i e^{2\pi i \nu \Delta t_i} \int_{-\infty}^{\infty} \vec{E}_1(\tilde{t}) e^{-2\pi i \nu \tilde{t}} d\tilde{t} \\
&= \vec{E}_1(\nu) \sum_i e^{2\pi i \nu \Delta t_i} \qquad (2)
\end{aligned}$$

For a derivation of an expression for Δt_i, the sketch in figure 6 is helpful. The time delay between the reference electron and electron i is

$$\Delta t_i = (R_i - R_1)/c.$$

With the far-field condition the distance to the observation point is large compared to the size of the bunch which results in $\vec{n}$ and $\vec{n}_i$ being parallel, if these vectors are the unit vectors directed to the point of observation. Since $\vec{r}_i + R_i \vec{n}_i = R_1 \vec{n}$ one gets for R_i

$$R_i = R_1 \vec{n} \cdot \vec{n}_i - \vec{n}_i \cdot \vec{r}_i \approx R_1 - \vec{n} \cdot \vec{r}_i \qquad (3)$$

With (3) the time delay becomes

$$\Delta t_i = -\vec{n} \cdot \vec{r}_i / c \qquad (4)$$

Combining (4) and (2) and using $\nu = \omega/2\pi$ for the frequency, the electric field becomes

$$\vec{E}(\omega) = \vec{E}_1(\omega) \sum_{i=1}^{N} \exp\left(\frac{i\omega}{c} \vec{n} \cdot \vec{r}_i \right).$$

Since the time-averaged Poynting vector U, referring to the energy per unit area and frequency, is proportional to $\left|\vec{E}\right|^2$, one gets

$$U = U_1 \left| \sum_{i=1}^{N} \exp\left(\frac{i\omega}{c}\vec{n}\cdot\vec{r}_i\right)\right|^2 \tag{5}$$

where the squared absolute value can be transformed into a double sum:

$$U = U_1 \left[\sum_{i=1}^{N}\sum_{k=1}^{N} \exp\left(\frac{i\omega}{c}\vec{n}\cdot(\vec{r}_i-\vec{r}_k)\right)\right]$$

For further evaluation one divides the double sum into a single sum with $i=k$ and another double sum with $i\neq k$. The first sum with $i=k$ has as its result the number of electrons N, because the argument of the exponential functions vanishes in all cases. Thus, one gets

$$U = U_1 \left[N + \sum_{i\neq k}^{N} \exp\left(\frac{i\omega}{c}\vec{n}\cdot(\vec{r}_i-\vec{r}_k)\right)\right]. \tag{6}$$

For a sufficiently large number of particles N and by using the normalized charge density distribution $\rho(\vec{r})$ the sum can be written as an integral and (6) becomes

$$U = U_1 \left[N + N(N-1)\int\int d\vec{r}d\vec{r}'\rho(\vec{r})\rho(\vec{r}')\exp\left(\frac{i\omega}{c}\vec{n}\cdot(\vec{r}-\vec{r}')\right)\right] \tag{7}$$

The charge distributions $\rho(r)$ and $\rho(r')$ are the same for N or $N-1$ particles due to the fact that the probability distribution of N and $N-1$ electrons are identical, if one assumes uncorrelated electrons. The longitudinal form factor is defined as the Fourier transform of the longitudinal charge distribution $\rho(z)$

$$F(\omega) = \int \rho(z)\exp\left(\frac{i\omega}{c}\vec{n}\cdot\vec{z}\right)dz \tag{8}$$

Thus (7) transfers to the simple form

$$U = U_1\left[N + N(N-1)\left|F(\omega)\right|^2\right] \tag{9}$$

which is the expression for the radiation spectrum.

One can easily see that (9) is divided into two parts: The first term is the incoherent part which is proportional to the number of electrons N. The second term shows the coherent part of the spectrum being proportional to $N(N-1)$, which is $\approx N^2$ when N is large. The form factor $F(\omega)$ determines which part is the dominate one. If the emitted wavelength is much smaller than the bunch length, the

form factor is negligible and the spectrum contains mainly the incoherent radiation. If one considers a wavelength in the range of the bunch length or longer, $F(\omega)$ will dominate and one has coherent radiation. Measuring the spectrum in that regime one can extract the form factor and thus the charge distribution. Being exact, the spectrum only delivers the absolute value of the form factor. The phase has to be reconstructed using mathematical methods. One is the *Kramers-Kronig-relation*. An overview of the derivation is given in [21].

1.3 Different types of coherent radiation

As discussed above, one can extract the longitudinal bunch profile from the spectrum of coherent radiation produced by the electron bunch. There are several techniques to produce such a coherent radiation. One of the techniques is the use of an infrared undulator, which, being in the main emphasis of the thesis, will be considered in detail in the following chapters. Below, a short overview of other types of coherent radiation is given.

1.3.1 Coherent Synchrotron Radiation (CSR)

Synchrotron radiation (SR) is produced, when a charged particle is accelerated by a force perpendicular to its velocity resulting in a change of the direction of motion [23], as it is the case in a bending magnet of an accelerator like in the magnetic chicanes. The total radiated power is proportional to E^4/R^2 where E is the electron beam energy and R the bending radius. Coherence, as discussed before, is reached with a wavelength comparable to or longer than the bunch length. For example, the bunch length at the first bunch compressor at FLASH results in wavelengths $\lambda \geq 200\,\mu$m which corresponds to the far infrared regime. In contrast to incoherent radiation the coherently emitted power is highly dependent on shape, charge and length of the bunch [7]. Figure 7 shows the spectrum of synchrotron radiation. At a critical frequency $\omega_c = (3/2) \cdot (\gamma^3 c/R)$ the spectrum is divided into two parts of identical

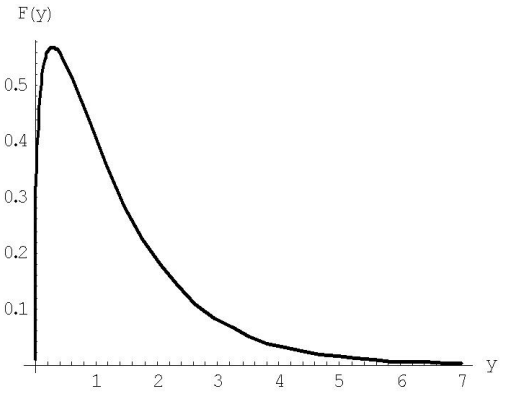

Figure 7: Normalized spectrum of synchrotron radiation $(1/I)(dI/dy) = \int_y^\infty K_{5/3} dx$, with $y = \omega/\omega_c$ and $K_{5/3}$ being a Bessel function [23]. I represents the intensity.

integrated power. This incoherent spectrum is negligible if a coherent emission is present.

In [23] it is shown that the angular distribution at ω_c is concentrated in a small cone with

$$\left\langle \Theta^2 \right\rangle^{1/2} \approx 1/\gamma.$$

Θ is called the *opening angle* of the synchrotron radiation.

1.3.2 Coherent Transition Radiation (CTR)

A charged particle which moves uniformly in a spatially inhomogeneous medium emits *transition radiation* because of the distortion of its electric field. This is the case when the particle crosses a boundary between two media with different dielectric behavior. In practice, this is realized with a thin mirror-like wafer. At FLASH, a polished silicon wafer and a silicon wafer with aluminum coating are used [24]. The incoherent radiation with optical wavelengths is called optical transition radiation (OTR) and is typically used for transverse electron beam diagnostics. The screen is placed directly in the vacuum chamber which makes this method destructive in contrast to CSR. A camera for OTR or a detector for CTR is used to image the radiation (figure 8). In addition to incoherent light especially short bunches also emit coherent radiation and thus one can use this method for coherent diagnostics [7]. A specialty of the CTR is the independence of the emitted power from frequency (U_1 in Eq. (9) is constant). Furthermore, the radiated power is confined in a small opening angle in forward and backward direction. Both forward and backward TR can be used for beam diagnostics. However, backward OTR provides a more simple experimental situation: backward TR is emitted in the neighborhood of the specular reflection, e.g., if the incidence angle of the beam to the screen is 45°, the radiation is emitted with an 90° angle with respect to the beam direction and it is easy to transmit it out of the beam pipe.

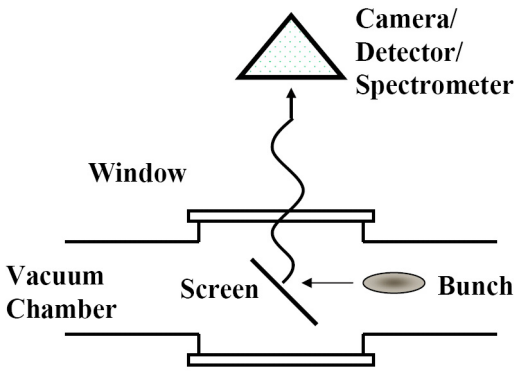

Figure 8: Schematic view of TR production

1.3.3 Coherent Diffraction Radiation (CDR)

Diffraction radiation (DR) is emitted, when an electron bunch crosses a hole or slit in a metallic screen or passes such a screen close to its edge. Coherent diffraction radiation (CDR) is more intense than incoherent DR and can be utilized in beam diagnostics. In contrast to TR, it is a non-destructive diagnostic tool [25].

2 Undulator

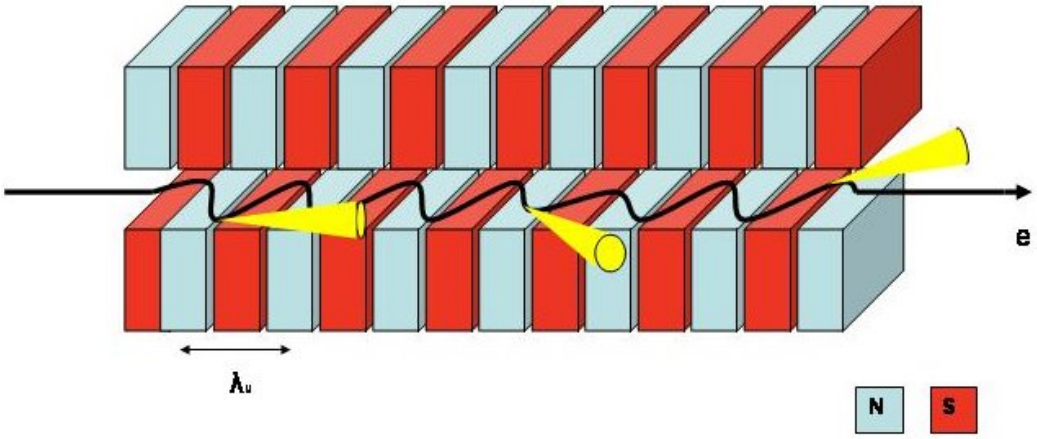

Figure 9: Sketch of an undulator. A periodic magnetic field forces electrons to pass a curved trajectory and to radiate into a cone.

An *undulator* is a common insertion device in accelerator based light sources (see figure 9). The properties of a photon beam from such a source are mainly defined by electron beam characteristics like beam dimensions, positional stability, charge etc. and additionally by undulator field and period [26]. In contrast to synchrotron sources like bending magnets, undulators kind of 'wiggle' the electron beam in such a way that the radiation is concentrated to a few frequencies. That is why the term *wiggler* was first only known for these devices. Undulators, however, are an advancement of the wiggler concept and the difference to wigglers is that the radiation is emitted in a narrow cone and a small frequency range.

The discussion in this chapter is about how undulators work, in which cases wigglers or undulators are used and why an undulator could provide the longitudinal bunch shape. Secondly, the infrared undulator at FLASH will be presented and a short description of a further usage will be given.

2.1 Basic Concepts

Undulators are insertion devices which generate a periodic magnetic field along the electron beam trajectory. The integral of the magnetic field vanishes over one undulator period and the velocity of the electron is also a periodic function of the longitudinal coordinate s (electron trajectory). In this subsection, the simplest undulator is considered in detail: *the planar undulator* (figure 9). The derivations follow the approach of [26].

For the next derivations, a moving coordinate system is considered, which sticks to the average velocity of the moving electron with transverse coordinates X and Y and longitudinal coordinate s. The longitudinal position s substitutes the time t with d/dt = c·d/ds. For simplicity an undulator with vertical sinusoidal magnetic field $\vec{B}$ is considered being

$$\vec{B} = \left(0, -B_0 \sin\left(2\pi \frac{s}{\lambda_U}\right), 0\right) \tag{10}$$

where λ_U is the period of the undulator. This expression for the magnetic field sticks to the longitudinal electron coordinate s in order to satisfy Maxwell's Equations. Note, that if one deviates transversely from this, the assumption of (10) is not valid anymore. The horizontal and vertical velocity at the longitudinal coordinate s normalized to the speed of light can be derived from the Lorentz force, which acts on the electron during undulator passage. The Lorentz force is

$$F_L = -e \cdot c\vec{\beta} \times \vec{B}. \tag{11}$$

with $\vec{\beta} = \vec{v}/c$, which is close to unity in longitudinal direction for an ultrarelativistic electron. The general expression for F comes from the time derivative of the momentum, which is defined as $\gamma mc\vec{\beta}$. As defined above, time derivatives transform to derivatives to s in this coordinate system. With all these information, (11) will become

$$\gamma mc^2 \cdot \frac{\mathrm{d}}{\mathrm{d}s} \begin{bmatrix} \beta_x \\ \beta_y \\ \beta_s \end{bmatrix} = -e \cdot c \cdot \begin{bmatrix} \beta_y B_s - \beta_s B_y \\ \beta_s B_x - \beta_x B_s \\ \beta_x B_y - \beta_y B_x \end{bmatrix}. \tag{12}$$

Thus, with $\beta_s \approx 1$ and $B_s = 0$ it follows, that the transverse velocities can be written as a function of the horizontal and vertical magnetic field:

$$\beta_x(s) = \frac{e}{\gamma mc} \int_{-\infty}^{s} B_y(s')ds' \qquad \beta_y(s) = -\frac{e}{\gamma mc} \int_{-\infty}^{s} B_x(s')ds' \tag{13}$$

where γ is the electron energy normalized to the rest energy mc^2. From the intention, that the undulator does not introduce a net deflection of the electrons after the passage, the integrals in (13) should vanish for one period. The velocities (13) can be solved with (10) to first order in $1/\gamma$

$$\vec{v} = (v_x, v_y, v_s) \approx c \cdot \left(\frac{K}{\gamma} \cos\left(2\pi \frac{s}{\lambda_U}\right), 0, 1\right) + C \tag{14}$$

with K as a dimensionless parameter called the *deflection parameter* or *undulator parameter*. C is a quantity smaller than $1/\gamma$. K is proportional to the product of the magnetic field amplitude and the undulator period

$$K = \frac{eB_0\lambda_U}{2\pi mc^2} \tag{15}$$

or

$$K = 0.0934 B_0[T]\lambda_U[mm] \tag{16}$$

With the fact that $\beta^2 = 1 - 1/\gamma^2$ and that $\vec{v} = c \cdot (\mathrm{d}\vec{x}/\mathrm{d}s)$ with $\vec{x} = (x, y, s)$ the horizontal and vertical position in respect to s can be derived from (14):

$$x(s) = \frac{K\lambda_U}{2\pi\gamma} \sin\left(2\pi\frac{s}{\lambda_U}\right) + C \qquad y(s) = C \tag{17}$$

The question to be solved is, how a single particle radiates when it follows the path s with transverse coordinates (17). In time domain, the electric field of an ultra relativistic charged particle in the moving frame is given by [27]

$$\vec{E}(z,t) = \frac{e}{4\pi\varepsilon_0 cz}\vec{n} \times \left(\vec{n} \times \frac{\mathrm{d}}{\mathrm{d}t}\vec{\beta}\right), \tag{18}$$

where z is the distance between source and observer and $\vec{n}$ the normalized vector directed from the source to the observer. Let the angles Θ_x and Θ_y be small. The opening angle of synchrotron radiation in longitudinal direction is given by $1/\gamma = \sqrt{1-\beta^2} \approx \sqrt{1-(\Theta_x^2+\Theta_y^2)}$, whereby the vector $\vec{n}$ becomes

$$\vec{n} \approx \left(\Theta_x, \Theta_y, \sqrt{1-\Theta_x^2-\Theta_y^2}\right) = \left(\Theta_x, \Theta_y, 1 - \frac{\Theta_x^2}{2} - \frac{\Theta_y^2}{2}\right) \tag{19}$$

To get the electric field for an ultra relativistic electron in an undulator which is transverse to the direction of observation, expressions (14) and (19) have to be insert into (18). Thus, the electric field becomes

$$\begin{bmatrix} E_x(\Theta_x, \Theta_y, t) \\ E_y(\Theta_x, \Theta_y, t) \end{bmatrix} = \frac{e}{4\pi\varepsilon_0 cz}\frac{d}{dt}\left(\frac{2\gamma}{1+(Kcos(2\pi(s/\lambda_U)) - \gamma\Theta_x)^2 + (\gamma\Theta_z)^2}\begin{bmatrix} Kcos(2\pi(s/\lambda_U)) - \gamma\Theta_x \\ -\gamma\Theta_y \end{bmatrix}\right) \tag{20}$$

where z is the distance to the source. In the plane of motion ($\Theta_y = 0$) the vertical component of (20) vanishes.

In the frequency domain the expression for the emitted wavelength, dependent on the electron energy, undulator parameters and angle of observation is given by

$$\lambda_1 = \frac{\lambda_U}{2\gamma^2}\left(1 + \frac{K^2}{2} + \gamma^2\Theta_x^2 + \gamma^2\Theta_y^2\right) \tag{21}$$

where the subscript 1 indicates to the first harmonic called the *fundamental*. A harmonic[4] is an integer multiple of the basic frequency. One can interpret (21) in the following way [27]:

1. The first term $\lambda_U/2\gamma^2$ is the slack between the radiation velocity c and the electron velocity βc
2. The term $(\lambda_U/2\gamma^2)\cdot(K^2/2)$ stands for the slack due to the oscillation in the undulator
3. The two terms $(\lambda_U/2\gamma^2)\cdot(\gamma^2\Theta_x^2)$ and $(\lambda_U/2\gamma^2)\cdot(\gamma^2\Theta_y^2)$ describe the slack owing to the observation under a certain angle.

Thus, λ_1 is the distance, which the electron falls behind during one undulator period compared to the photons.
From (20) one can derive that for small K values the field seen by the observer is quasi-sinelike. This results in a strong fundamental peak at a frequency $\omega_1 = 2\pi c/\lambda_1$. As K increases one gets a distortion of the symmetric sine wave which results in higher harmonics because the field pulse gets narrower. The higher the K value the larger the distance between two successive peaks resulting in a decreasing frequency of the fundamental. On-axis ($\Theta_x = 0$ and $\Theta_y = 0$), the emission for the even harmonics vanishes because in that case the pulses of positive and negative electric fields are equidistant in the time domain and thus they cancel each other. Having even harmonics in the spectra is always a sign that one is not on-axis as an observer. The relative width $\Delta\omega/\omega$ of the lines in the undulator spectrum for a single particle and an observation at a single point is given

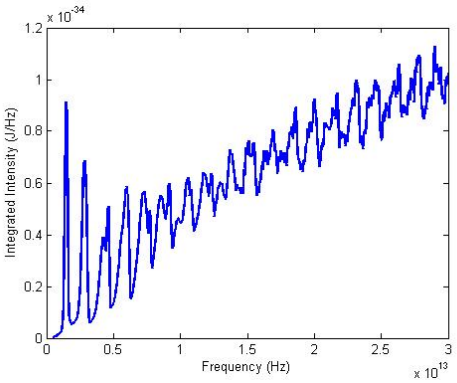

Figure 10: Spectrum of a high K device. Intensity is integrated over a small area, electron energy 511 keV, coil current 435 A corresponding to K = 44. The higher the photon frequency, the more it resembles to synchrotron spectrum.

[4]The name comes from the acoustics, where notes being an integer of the basic frequency sounds harmonicly when played together.

by $1/kN$ at a frequency of $\omega_k = k\omega_1$, where k is the harmonic number and N the number of undulator periods and where the width $\Delta\omega$ is the full width half maximum (FWHM) of the peak [28]. At the same time, the emission cone decreases by a factor of $1/\sqrt{kN}$ compared to the opening angle of synchrotron radiation $1/\gamma$. The field of a planar undulator, observed on-axis, is linearly polarized. The plane of polarization is chosen by parameters like the direction of emission or the harmonic number. In forward direction, the vertical field component is, as derived from (20), alway zero so that this provides horizontally polarized radiation.

Undulators with its small K have a dominant first harmonic. Small K means from (15) small undulator period λ_U or small B_0. This leads to a small oscillation amplitude of the electrons and thus the emitted light cones interfere. An observer on-axis sees a permanent light spot slightly fluctuating in intensity. Increasing K makes this fluctuation more and more obvious and slower so that one can finally see the light cone only in a certain moment while it is invisible in between. The reason is the lack of interference of the cones produced by different periods because of the large oscillation angle of the electron trajectory. A wiggler is therefore nothing else than a high K undulator. In figure 10, the spectrum is plotted in dependence of the frequency for a given K value, undulator period and electron energy. The spectrum smooths out for large energies and resembles more to a synchrotron radiation spectrum. There are several reasons for the smoothing [26]:

- Angular acceptance: As known from Eq. (21), the wavelength is dependent on the angle. With a sufficiently large angular acceptance it occurs, that the $(k+1)$th harmonic off-axis can overlap with the kth harmonic on-axis. This is the case, if $\gamma^2\Theta^2 \geq (1+K^2/2)/k$. This contribution is dominant.

- Electron energy spread: From (21) it is further known, that the wavelength depends on the square of electron energy. Energy spread will smooth out the spectrum, if $\Delta E/E \geq 1/2kN$.

- Magnetic field errors: Imperfections in the magnetic field distribution result in an imperfect constructive interference especially for high harmonics which has an enhancing effect on the smoothing.

- The wavelength acceptance: One last broadening effect is due to the fact that an observer interested in collecting a large flux always integrates the spectral flux over a finite aperture while the resonance frequency varies from one point to another because of the different angles of observation. If the bandpass exceeds the relative distance of the harmonics to each other ($\Delta\omega/\omega = 1/k$), the harmonics will smooth out.

Up to now a single electron or filament beam was assumed. With effects like energy spread within a bunch, a thick beam with all connected collective effects is

the more realistic description. The spectrum produced by a filament electron beam in a certain direction is made up of a series of harmonic peaks. It was derived for a planar undulator that the frequency of the fundamental is given by

$$\omega_1 = \frac{2c\gamma^2}{\lambda_U(1+(K^2/2)+\gamma^2\Theta_x^2+\gamma^2\Theta_z^2} \tag{22}$$

where Θ_x and Θ_z stand for the angles between the electron trajectory and the observer. While one could get for a filament beam very narrow peaks in the spectrum, there are the limitations given above for getting such small harmonics for a thick beam.

There is a difference between the broadening effect from an energy spread and the effect of emittance and aperture size. The energy spread σ_γ/γ can comprise the whole bunch which leads with (22) to a frequency spread σ_ω/ω for each harmonic towards smaller and larger frequencies. In contrast to that, the angular spread only induces a shift of ω_1 to lower frequencies. In total, one observes the following situation: The peak of an odd harmonic seen on-axis presents a steep slope on the high energy side determined by kN, as mentioned earlier in this chapter, and σ_γ/γ from the energy spread. On the low energy side one observes a reduced slope determined by beam parameters like the emittance and external parameters like apertures. In low energy machines like FLASH with only 1 GeV electron energy and small emittance the peak broadening is dominated by the energy spread within the bunch.

Collecting the radiation emitted on-axis, one can tune the spectrum in different manners. The frequency ω_k can be changed by jumping from one harmonic to the next within the series $k = 1,3,5....$ Tuning of the spectrum continuously is done by changing the K-parameter by varying the peak field of the device. In a permanent magnet undulator the magnetic field is changed by varying the gap between the poles. The peak field of electromagnetic devices can be controlled by the magnet current. The upper limit of the K value is determined by the minimum possible gap in the case of a permanent magnet undulator and in a electromagnetic undulator by the maximum available current and by the minimum gap.

The last basic concept in this chapter is the treatment of the radiation emitted by an electron bunch passing by an undulator. G. Geloni et. al. presented a concept treating undulator radiation as a laser-like beam [29].

Assuming that the resonance condition (22) of a planar undulator is satisfied, one gets from (13) the transverse velocity of an electron on its path s, if $s = 0$ is defined as being the position right in the center of the device:

$$\vec{v}_\perp(s) = -\frac{cK}{\gamma}\sin(k_U s)\vec{e}_x \tag{23}$$

where K is again the undulator parameter and $k_U = 2\pi/\lambda_U$ the undulator wavenumber. Following the light emitted during the passage brings the observer into the so-called far-field zone. This region is reached, if the distance between the observer and the source is much larger than the undulator length [30]. The far-field allows a convenient approximation: Radiation from an ultra relativistic charged particle can be interpreted as radiation from a *virtual source*, which produces a laser-like beam. To be clear: the electrons passing the undulator emit light in every undulator period. In the far-field region, however, the observer cannot distinguish anymore, whether the radiation is emitted within the first or last period. Thus, the light can be thought of being produced by a source in the middle of the insertion device. In the next chapter there is a detailed discussion about this concept, because the treatment of the synchrotron light out of an undulator as a laser-like beam opens the possibility to use Fourier optics to propagate the beam and accordingly to use simulation tools like *ZEMAX* developed for laser setups. This is due to the characteristic of laser light forming a plane wave at the source point which leads to a Fourier transform relationship between the field and content of the plane wave at this point.

2.2 Infrared Undulator at FLASH

FLASH has been equipped with a new infrared (IR) undulator in summer 2007. In March 2003, the idea of using an undulator as a diagnostic tool for longitudinal bunch shape measurements was first published in [30]. The University of Hamburg thus started the development of an undulator, adequate for this purpose, with the Joint Institute for Nuclear Research (JINR) in Dubna (Russia).

In the first part of this section an overview about the technical features of the new device is given, followed by a description of the commissioning in Dubna and Hamburg. Then, the idea of bunch diagnostics using the infrared undulator will be presented before a further application of the device is discussed. The technical parameters of the undulator and the results of preparatory magnetic measurements are taken from [31] and [32].

2.2.1 Design of the IR Undulator

The infrared undulator at FLASH was designed by the Russian institute JINR in Dubna. It is constructed as a mid to far infrared coherent source for the special demands of the FLASH accelerator facility. In contrast to the FEL undulators, which are permanent magnet devices, the new undulator is a planar electromagnetic undulator having 9 full periods with a length of 40 cm each. A peak magnetic field of 1.2 T is reached with a maximum coil current of 435 A. Figure 11 shows the general design of the undulator while figure 12 is a picture taken during the

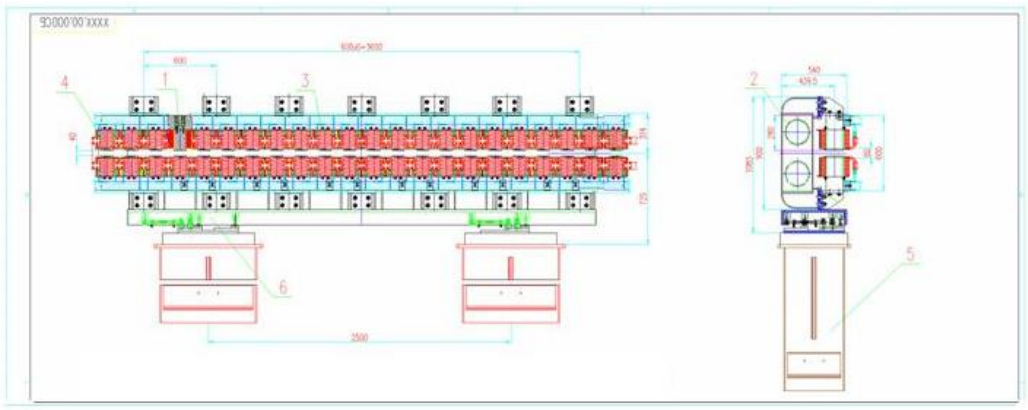

Figure 11: Drawing of the new infrared undulator at FLASH (courtesy of JINR, Dubna).

magnetic field measurements in Hamburg. Important parameters of the device are listed in table 2. The undulator has 44 poles and a K-value from 1 to 44 which corresponds to a maximum wavelength of 200 µm at an energy of 500 MeV or 50 µm at the design energy of 1 GeV.

The local conditions in the FLASH tunnel defined some of the characteristics of the device. The weight is restricted by the limitation of the transportation crane in the tunnel to 5 tons. A limit in the height is given by the bypass beam line of the accelerator above the IR undulator. This height limitation had consequences for the whole construction. As one can see in figure 11 and 12 the undulator's basic construction is a C-shaped support made of a non-magnetic steel, which holds the magnetic yoke. The yoke consists of two ferromagnetic girders of steel. Each girder contains 22 poles. Due to limitations in height, weight and also power supplies, the yoke thickness is less than required for a gap field of 1.2 T which leads to an oversaturated magnetic field within the yoke of 1.9 to 2.1 T. Due to the oversaturation, the magnetic field in the center of the gap depends for high excitations on the individual positions of every coil. Therefore, the coils are designed to be slightly mobile in a range of

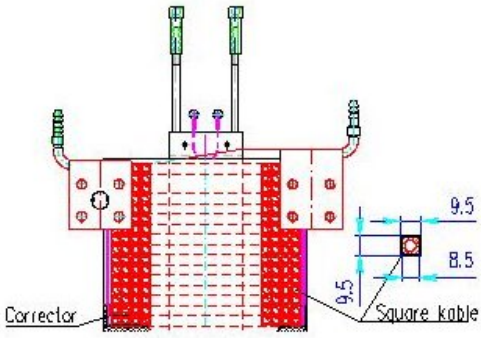

Figure 13: Drawing of a main coil of the undulator. One can see the structure of main and correction windings.

Figure 12: IR undulator at a measurement bench at DESY Hamburg. Previous magnet measurements were done in Dubna and Hamburg for finding optimum settings for correction coils and windings.

1 mm to compensate vertical positioning errors.

The poles are constructed with a precision of 50 µm, where each has a width of 100 mm. The C-shaped yoke limits the flexibility of the gap size necessary due to magnetic forces to less than 20 µm. Pole pairs 3 to 20 represent the main coils of the undulator. They consist of four layers with 16 turns each, the windings are of square copper pipe with cooling channels. The cooling is done with desalinated water which is also used for the accelerator. Between the windings there is an insulation layer of 0.8-1 mm thickness. In figure 13 a cross-section of a main coil is presented. This picture shows an additional layer of correction windings which are necessary to compensate magnetic perturbations due to imperfections of the whole magnetic system of the undulator.

The first and last pair of coils have only 1/8 of the turns of the central coils. The second and second-last have 1/2 of the turns (see figure 14 a) and b) for the cross-sections of these coils). Additionally, these coils have also correction windings. These correction coils allow a current of up to 15 A.

2.2.2 Magnetic Measurements in Dubna and Hamburg

In order to reduce the influence of magnetic imperfection of the magnetic system, preparative magnetic measurements have been performed. The perturbations in this system are characterized by the *first and second integrals* of the vertical field:

$$I_1 = \int_{-\infty}^{s} B_z ds' \qquad I_2 = \int_{-\infty}^{s} ds' \int_{-\infty}^{s'} B_z ds'' \tag{24}$$

Parameter	**Value**
Type	Electromagnetic
Gap	40 mm
Period length	40 cm
Pole length/width	10/14 cm
Number of full periods	9
Number of poles	44
Overall length	4.455 m
Maximum K-Value	44
Maximum field	1.2 T
Good field region	$\pm$10 mm
Number of turn main coils	64
Number of turn 1./2. coil	10/34
Maximum current undulator coils	435 A
Maximum current of regular correction coils	2 A
Maximum current of edge correction coils	15 A
Total weight	4490 kg

Table 1: Parameters of the infrared undulator.

The meaning of these integrals becomes clear with the equations (13). The offset and the divergence of the electrons after the passage of the undulator are

$$x' = \frac{e}{\gamma mc} \cdot I_1 \qquad\qquad x = \frac{e}{\gamma mc} \cdot I_2. \tag{25}$$

Thus, the first and second integral give the influence on the electrons during the undulator passage. For a perfect insertion device, these integrals and thus the parameters from (25) are zero. But a magnetic insertion device is even in theory not a parasitic instrument, because the horizontally deflecting fields cause a weak vertical focusing. In reality there are always imperfections caused by construction, material characteristics and influences from the environment. For reducing the perturbations from magnetic imperfections and therefore for minimizing the two integrals, the undulator has additional correction windings.

The two last pole pairs on each side have different numbers of turns. This allows to have the starting condition $x(0) = x'(0) = 0$, which is necessary for a stable motion.

The main work during the first magnetic measurements in Dubna was to find the right currents for the correction coils and to achieve the following goals:

- Values of first and second field integral in each regular period less than $2 \cdot 10^{-4}$ T·m or $2 \cdot 10^{-4}$ T·m^2.

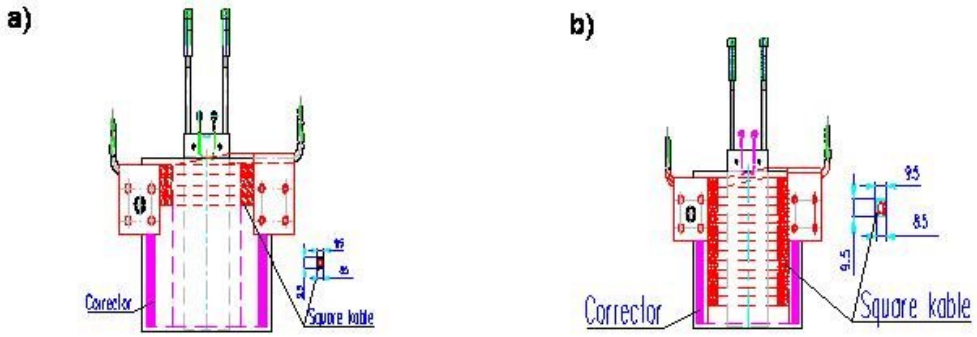

Figure 14: a) First coil of a row has only 1/8 of the turns compared to the main coils. b) Second coil of a row has 1/2 of the turns compared to main coils.

- Second field integral (the electron trajectory) should be as parallel as possible to the undulator axis.
- The above requirements should be valid for the whole current range from 0 to 435 A.
- The number of power supplies for the correction coils have to be minimized.
- One has to have a reproducibility for the tuning within $0.5 \cdot 10^{-4}$ T·m for the first and $0.5 \cdot 10^{-4}$ T$\cdot$ m^2 for the second integral.

All magnetic measurements were done with a Hall probe on a measurement arm, allowing three dimensional measurements. The exact description of the measurements can be found in [32].

In Dubna only measurements in a lower current regime were possible. The finishing of field integral minimization for currents up to the maximum current of 435 A was an important task at the measurement bench in Hamburg (figure 12). A check of reproducibility of the results after shipping showed good agreement which indicates that there have been no damages during transportation. The resulting field integrals from magnetic measurements can be found in figure 15 and 16. One can see that the first integral has its absolute value between $0.1 \cdot 10^{-4}$ and $1.51 \cdot 10^{-4}$ T·m while the absolute value of the second integral is found to be in between $0.15 \cdot 10^{-4}$ and $46.2 \cdot 10^{-4}$ T$\cdot$ m^2. The reproducibility for the integrals without changing the coil currents was $\pm 0.25 \cdot 10^{-4}$ T$\cdot$ m for the first and $\pm 0.5 \cdot 10^{-4}$ T·m^2 for the second field integral.

As mentioned in the previous subsection, the magnetic yokes are made of ferromagnetic steel. It is characteristic for ferromagnets that after an initial magne-

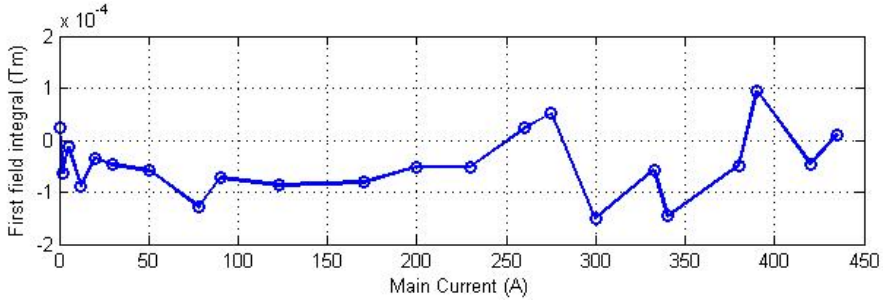

Figure 15: The first field integral measured and optimized during magnetic measurements in Dubna and Hamburg. Values measured in between absolute values of $0.1 \cdot 10^{-4}$ and $1.51 \cdot 10^{-4}$ T·m.

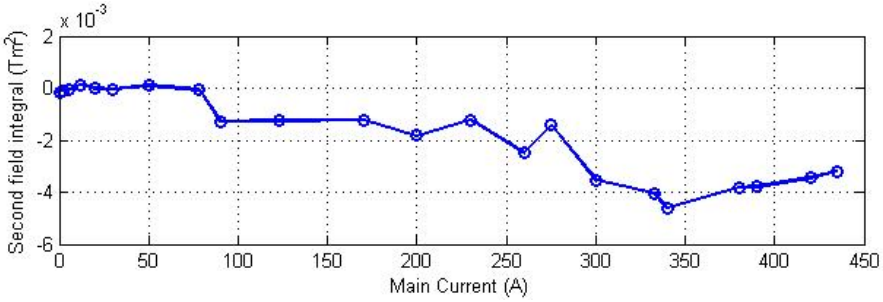

Figure 16: The second field integral.

tization the magnetic field follows the hysteresis curve [33]. To have an adequate reproducibility for the field integrals, one has to follow this curve during the tuning of the undulator. For a first cycling of the magnet, one sets the current from 0 A to 435 A and then back to 0 A. During this, the corrector currents are switched off. Whenever changing the current, the hysteresis curve has to be followed, which means for a decrease of current, that one has to set the main current first to 435 A, then to 0 A, before one can set the desired value.

As it is known from the hysteresis curve, the magnets have a remanent field at zero current. To minimize the remanent field a degaussing procedure is used. With this method the minimum remanent field is approached step by step. The excitation main coil current is set subsequently to the following values in Amps: +400, -400, +200, -100, +50, -40, +30, -20, +15, -13, +11, -9, +7, -5, +4, -3, +2, -1, +0.5, -0.25, 0.

2.2.3 IR Undulator as Coherent Diagnostic Tool

Let us consider an undulator with K>>1. This means that the tuning range is large. Large frequency range results in a high resolution of short structures.

Secondly, the transverse velocity of the electron beam should be small compared to the longitudinal one, so that the total condition can be summed up to: $1<<\mathrm{K}<<\gamma$. To limit the collection of the radiation to the central cone, it is sometimes required to insert an angular aperture. This depends on the divergence of the radiation. The half angle of the coherent central cone is given by

$$\Theta_{cen} = \frac{\sqrt{1+K^2/2}}{\gamma\sqrt{N}} \tag{26}$$

where K is the undulator parameter and N the number of periods. Let the electron bunch pass through the undulator emitting a light pulse of a specific resonant frequency ω_1 depending on the K value to which the undulator is tuned to.

The concept using undulator radiation for longitudinal bunch profile measurements was first published in [30]. The idea is to record the energy of the coherent radiation pulse emitted into the central cone for every wavelength achievable by the undulator. The pulse is recorded by an infrared-sensitive detector. Repeating this measurement for different K values (and thus different resonant frequencies) gives the absolute value of the form factor after deducting the incoherent part from the intensity. From section 1.2 is known that the form factor is the Fourier transform of the charge distribution. Thus, the absolute value of the form factor from the spectrum gives the longitudinal bunch structure assuming that one can somehow reconstruct the phase. The method behind that is subject of this subsection.

The bunch structure is given by the charge distribution and thus by the form factor. From section 1.2 is known, that the form factor is the origin for coherent enhancement. Figure 17 show sketches of arbitrary incoherent single-particle spectra which can be produced by tuning the undulator from small to high wavelengths. First, the fundamental appears. For longer wavelengths also higher harmonics are visible. The main interest is the observation on-axis. As discussed in section 2.1, in this regime there are no even harmonics, but there are strong resonant peaks for $\omega = \omega_1, 3\omega_1, 5\omega_1, ...$ Additionally, the bunch with its longitudinal form factor affects the spectrum with its square modulus. Figure 18 shows the same spectra as in figure 17, but with the form factor included.

As long as the form factor, convoluted into the spectrum, is negligible (this is the case for wavelengths shorter than the effective bunch length), the bunch radiates incoherently and the spectra do not differ from the ones in figure 17. As soon as the wavelength approaches the bunch length, the harmonics are influenced by coherent enhancement caused by the longitudinal form factor. The bold lines in figure 18 are the measurable spectral curves for an electron bunch. Thus, by tuning the undulator through the whole range of K-values with simultaneous measurements of the intensity, one can scan the form factor, because one only sees

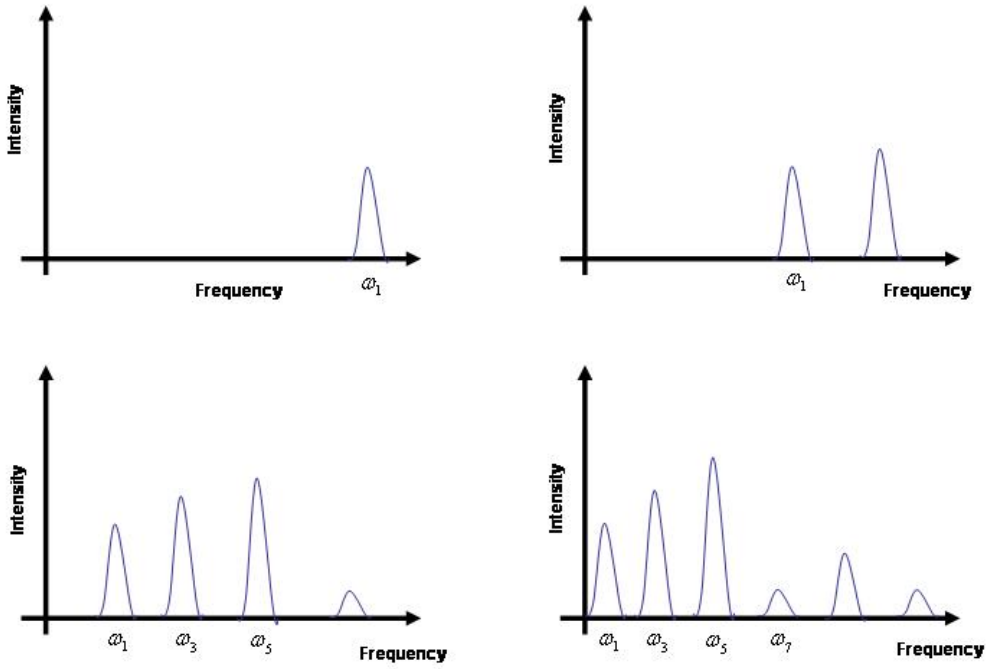

Figure 17: Sketch of arbitrary spectrum of a single particle.

the coherent part of the spectrum. This is due to the domination of the coherent radiation intensity in the spectrum.

Now, a relationship between the expected value of the energy per pulse of the emitted radiation and the square modulus of the bunch form factor $|\bar{F}(\omega)|^2$ is needed for the application of the proposed method.

The form factor decreases more slowly than the sharp resonant peaks (see figure 18). That means, that the function $|\bar{F}(\omega)|^2$ can be replaced by a constant $|\bar{F}(\omega_0)|^2$ at the center of the resonance curve (the fundamental). Thus, for each wavelength or frequency of the undulator, an absolute value of the form factor averaged over the bandwidth is measured. The relationship between measured energy and the absolute value of $|\bar{F}(\omega_0)|^2$ is

$$\Delta W = A \cdot N^2 \, |\bar{F}(\omega_0)|^2 \tag{27}$$

where A is a constant depending on the undulator and electron beam characteristics. One should remember now the expression (9) in section 1.2. With (27) the coherent part of the spectrum, which is proportional to the square modulus of the

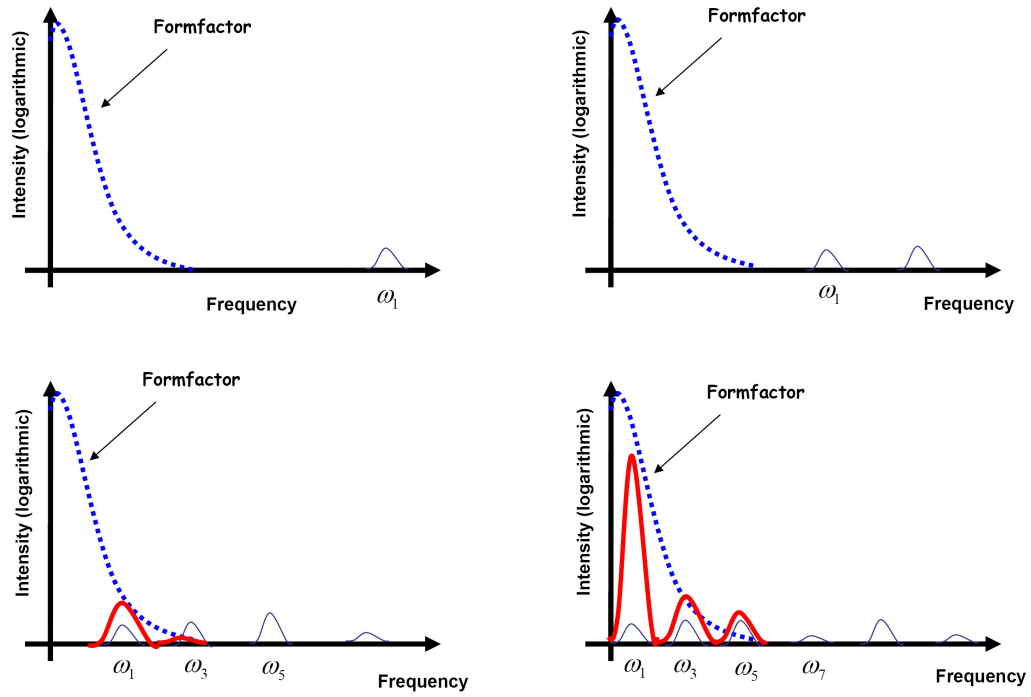

Figure 18: Same spectrum as in figure 17, but now with the longitudinal form factor taken into account. The form factor leads to coherent enhancement of the intensity. Note, that in these spectra a logarithmic scale is assumed for the intensity.

form factor and square of the number of electrons in the bunch, is obtained. The scan of the form factor is done with the following method: First, one tunes to very small wavelength. Then, the wavelength becomes longer by tuning the undulator to higher K-Values. For each wavelength the intensity is measured. As soon as the fundamental reaches the coherent part (or the form factor), one gets a measurable intensity. When the next higher harmonic enters the coherent region, one can get the contribution of the fundamental out of the total intensity by subtracting the intensity of the higher harmonic. This intensity is known from the intensity measurement of the fundamental at the same frequency. This gives a complete scan of the form factor.

Important is the knowledge of the undulator spectrum for knowing the contributions to the total intensity. For this purpose it is necessary to measure spectra first, what is one subject of this thesis.

All these ideas are based on two assumptions: First, the resonance condition is met all the time and secondly, one operates only in the far-field approximation meaning that the distance is longer than the undulator length. In most of the

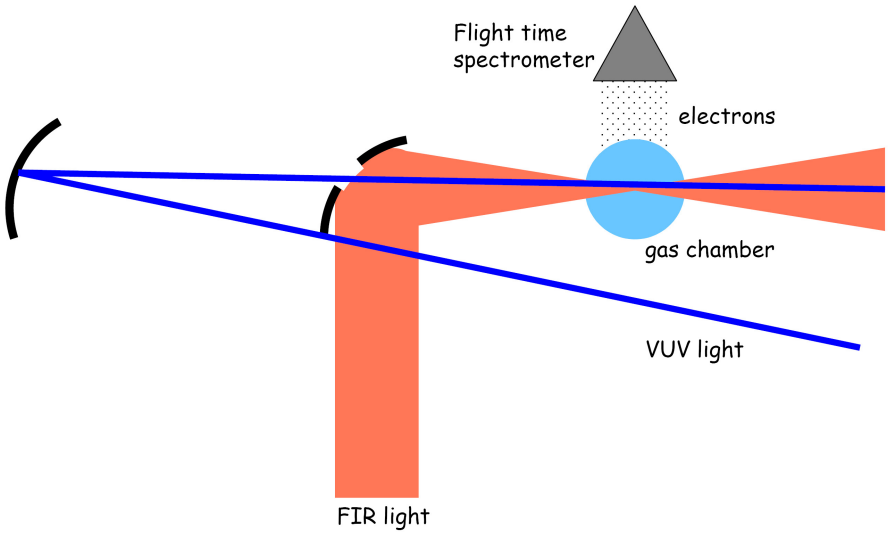

Figure 19: Sketch of THz-Streak-Camera for measuring the time structure of FLASH VUV-pulses

cases, it is impossible to get the phase information out of the spectrum. Only if one has a symmetrical density distribution like a Gaussian shaped bunch, the absence of the phase information is of no importance, since the phase is simply constant. With the present layout of FLASH, without the third harmonic system (see section 1), the longitudinal shape of the electron bunches is far from Gaussian. Therefore, techniques like phase reconstruction with the Kramers-Kronig-Relation [21], which is purely mathematical, or the constrained deconvolution[5] have to be applied, in order to reconstruct the bunch shape.

2.3 Further Application of IR Undulator

The infrared light produced by an electron bunch passing the IR undulator has a very convenient side effect: It is naturally synchronized to the VUV pulse emitted by the same bunch in the FEL undulator. This leads to the opportunity for *pump-probe-experiments*. Up to now, pump-probe experiments at FLASH are done with an optical laser. For example, the optical laser pulse activates a photochemical reaction in a gas or liquid which can be 'pictured' by the VUV pulse of FLASH [34]. The infrared source extends the number of available pump-probe light sources.

[5]The constrained deconvolution method uses the knowledge of the time structure of the bunch after compression. The purpose of the measurement is then to determine the numerical value of the parameters on which such temporal structure depends.

The first experiment with the synchronized IR and VUV pulses will be a THz-Streak camera which can resolve the time structure of the FLASH pulse [35]. Up to now there has been no possibility to measure the shape of the VUV pulse directly. The information about structure and peak intensities is based on simulations and estimations from measured spectra. One expects that the pulse consists of one or more spikes with a shape variation from pulse to pulse. For some experiments it is important to have the information, whether it was a pulse with one or more spikes. For example using the pulse to excite atoms, a second spike can cause a higher excitation. This is often unwanted, but even if it is uncritical or even wished for certain experiments, the exact pulse shape has to be known.

In the THz-Streak camera experiment the VUV pulses are superimposed with the synchronized infrared light in noble gas. In figure 19 the set up is sketched. The VUV pulse comes over a delay line through a hole in a mirror into the chamber. However, the infrared light is focused by this mirror due to larger beam size. The photo-electrons produced by the VUV photons are accelerated by the electric field of the IR light. Thereby, the change in the kinetic energy of the electrons caused by this electric field is dependent on the moment in time of the ionization. Therefore, one can reconstruct the time structure of the FLASH VUV-pulse by measuring the spectra of the photo-electrons recorded by two time-of-flight spectrometers.

3 Design and Construction of the Experiment

One subject of the work for this thesis was the development of a spectrometer based on the concepts from [11]. Furthermore, a new experimental station in the FLASH experimental hall with a setup containing the developed spectrometer had to be designed and constructed. In this chapter, an overview of the infrared beamline, transporting the radiation produced within the IR undulator to the experimental hall, is given with a description of the diagnostic port used for the developed experimental station. This is followed by a section about the new spectrometer designed for the spectral investigations which are part of the second subject of the thesis (see section 4.2). For the experimental setup at the measurement station in the hall, adequate preparative optics were designed to match the requirements of the spectrometer. The related optical calculations are presented in section 3.3, the final setup at the diagnostic port forms the last part of this chapter.

3.1 Infrared Beamline

The light produced by the infrared undulator is transported into the experimental hall by an infrared beamline. The specialty of this beamline is its ability to transport radiation from 1-200 µm without destroying the pico-second time structure of the pulses [35]. The challenge of the beamline construction is the large divergence of the infrared beam with various unavoidable apertures at the same time. This problem has been solved by using several toroidal mirrors as focusing elements for all apertures asides from the electron beam pipe. As one can see in figure 20, the IR pulse first travels along the usual electron beam pipe together with the vacuum ultra violet (VUV) radiation produced in the FEL. It has a much larger opening angle than the VUV pulse which allows the following outcoupling method [36]: 7.7 m behind the IR undulator a mirror with a 10 mm hole in the center is installed. The VUV pulses with their small divergence pass through this aperture, whereas the infrared radiation is deflected 90 degrees sidewards.

Next to the first mirror (M1) there is the first Diagnostic Port (DP1) which has been mainly used for beamline and undulator commissioning in the end of the year 2007. A few meters further downstream is the second diagnostic port (DP2) which will be used for electron diagnostics in the future. As one can see in figure 21, which shows a schematic sketch of the beamline, the infrared radiation is channeled after DP2 into the synchrotron radiation (SR) beamline (transporting the radiation from the last dipole of electron beamline) for passing the tunnel used by the ring accelerator PETRA III. After the PETRA tunnel, the beamline reaches the experimental hall in the *beam distribution area (BDA)*. At the beginning of the BDA, the infrared light is separated from the SR and transported in a beam pipe having an angle of 11.3° with respect to the FEL axis. At 42 m (measured from the

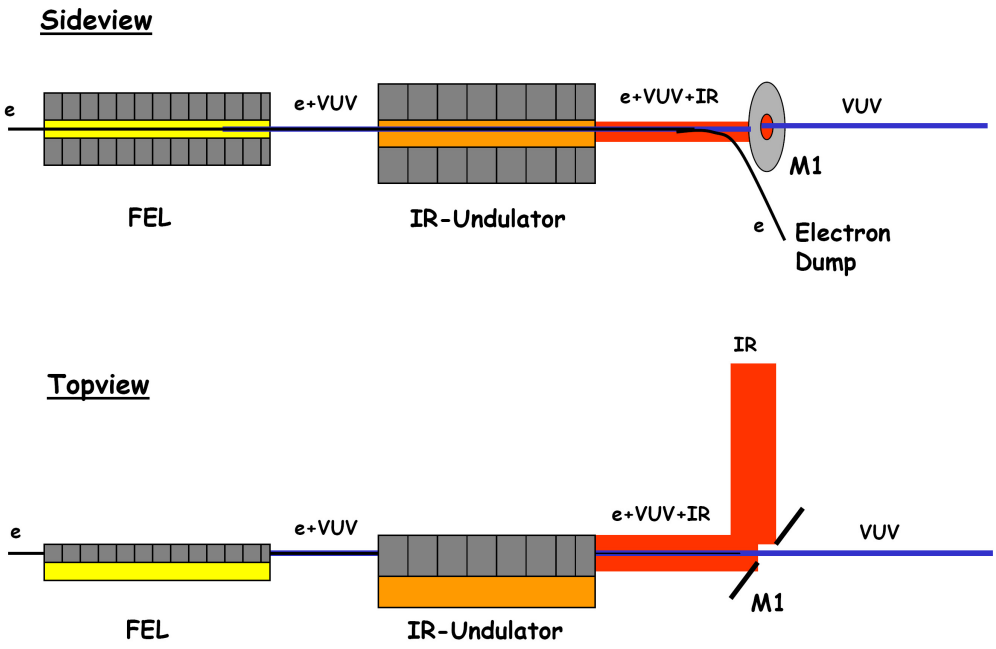

Figure 20: Sketch of the production of radiation and separation of IR and VUV beam after the electron dump.

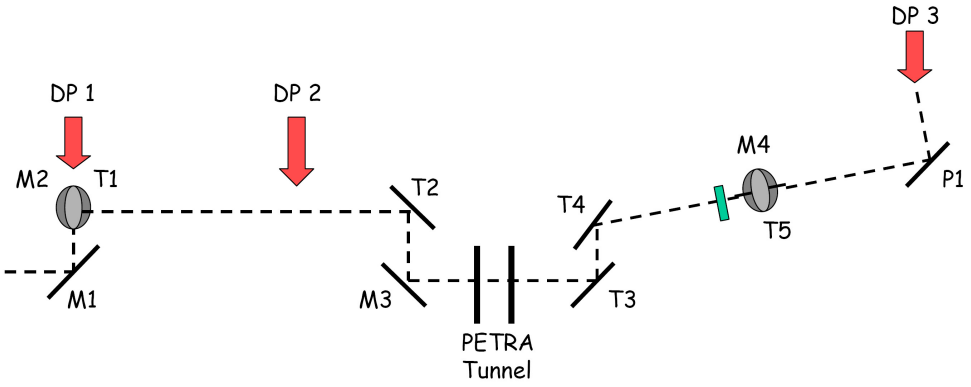

Figure 21: Sketch of the infrared beamline up to electron diagnostic port DP3. Mirrors signed with "M" are planar mirrors, the ones signed with "T" are toroids. The outcoupling mirror at DP3 is a parabolic mirror. M2/T1 and M4/T5 are correcting the height. In front of M4 a diamond window is installed, which separates the HASYLAB vacuum from machine vacuum. The distance between source in the center of the undulator and DP3 is about 50 m.

center of the IR undulator) a diamond window of 50 mm diameter separates the accelerator vacuum from the vacuum system in the experimental hall, which does not have the ultra high vacuum conditions like it is required for the accelerator beam pipe.

At about 50 m, there is the third diagnostic port (DP3) as first port in the experimental hall. Further downstream, at 55 m, DP4, a permanent photon diagnostic station, is installed and at the end of the infrared beamline is DP5 for the THz Streak camera experiment described in section 2.3.

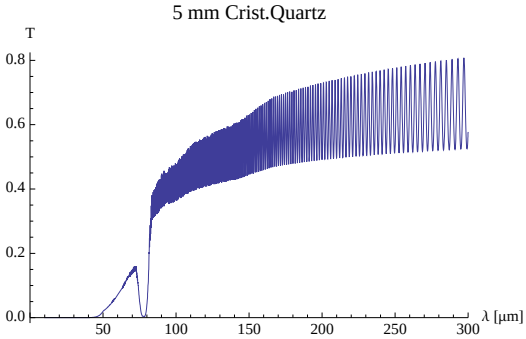

Figure 22: Transmission curve of crystalline quartz. This curve shows interference pattern due to the thickness (Etalon effect)

The measurement station for electron beam diagnostics has been installed at DP3 (figure 21). There, a mirror deflects the beam out of the vacuum pipe of the infrared beamline into the setup at the experimental station through a window that separates the beam pipe vacuum from the atmospheric pressure of experimental setup. Figure 22 shows the transmission curve for infrared radiation for crystalline quartz. Aim of the measurements in this thesis is the investigation of the spectral content of infrared undulator radiation from 1-200 µm.

Due to the cut-off of transmission below 70 µm crystalline quartz windows are not usable. A better solution is the usage of diamond instead. In figure 23 the transmission curve of diamond (thickness=0.6 mm) is presented showing a much better behavior over the whole wavelength range interesting for the spectral analysis. A diamond window of 20 mm diameter is installed at DP3.

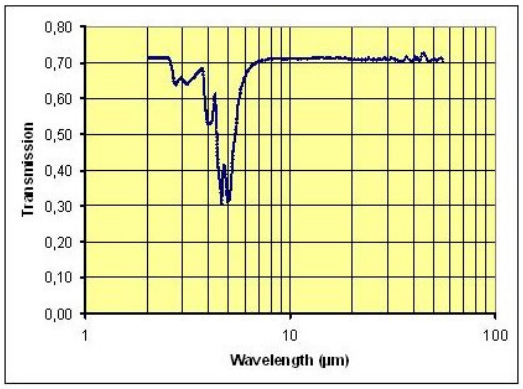

Figure 23: Transmission curve of diamond with a thickness of 0.6 mm.

Assuming horizontal polarization for radiation from the planar IR undulator, one finds the polarization being vertical after the transport by the infrared beamline to DP3.

In total, the beamline transports the light over a distance of up to 65 m with 7

planar and 6 toroidal mirrors. The beamline setup was optimized with simulation tools like *ZEMAX*[6] and *THz-Transport*[7]. Most of the losses occurring for long wavelengths are caused by the small aperture of the electron beam pipe which affects the beam on the first 7.7 m after the IR undulator. For short wavelengths the losses are mostly due to the hole in the first mirror.

3.2 The Spectrometer

The idea of scanning the form factor by measuring the intensity is possible, if the spectrum of the IR undulator is well understood. Thus, a first step has to be an investigation of the undulator spectrum dependency on machine and undulator parameters. For this purpose, a scanning spectrometer has been designed using reflective blazed gratings as dispersive elements and a pyroelectric detector as infrared sensor. The principle of the device is based on the concepts from [11]: The incident infrared beam has to pass a filter grating before it hits on the dispersive element, because otherwise short wavelengths would lead to higher orders in the dispersed radiation. The term 'order' refers to the diffraction order of the dispersed radiation. A rotatable arm with a focusing mirror scans the dispersive section, deflecting the spectral components on the detector.

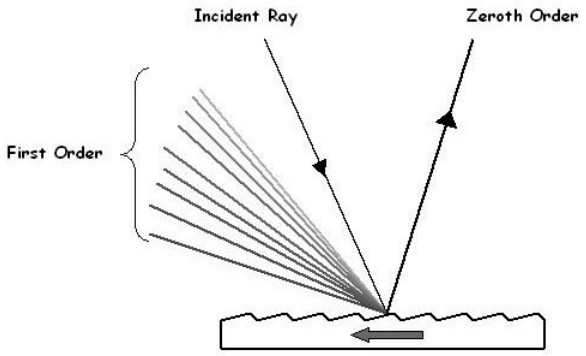

Figure 24: The spectrometer uses reflective blazed gratings as dispersive elements. The special blazed shape of grids allows a very good efficiency. For optimum efficiency, the first order has to go into the direction of the oblate slope.

In the following, the concepts of the gratings, the pyroelectric detector and the final spectrometer design will be presented in separate sections.

[6] www.zemax.com

[7] Developed by Bernhard Schmidt (DESY), www.desy.de/schmidtb/THz-Transport/THzTransport.m

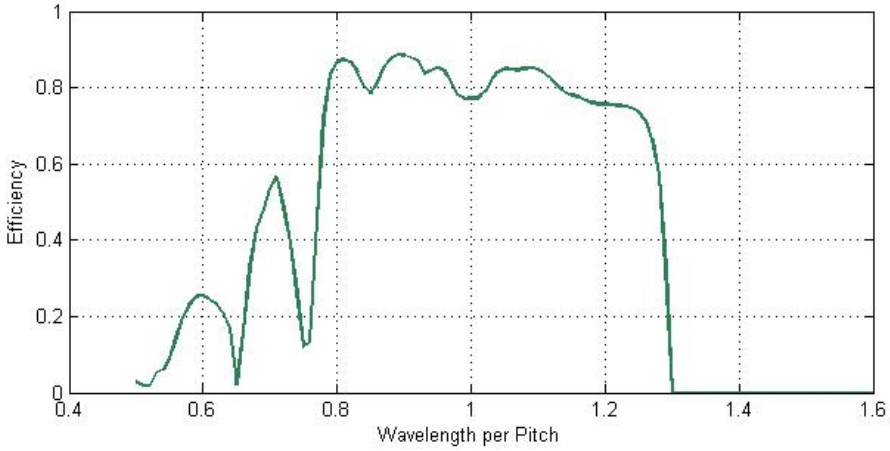

Figure 25: Efficiency curve of reflective blazed gratings for the first order with an assumed incidence angle of 17°. This plot is valid for gratings with a blazed angle of 26.75° of different pitch size. The curve is calculated with GSolver [37].

3.2.1 The Gratings

The gratings used in such a spectrometer setup are reflective blazed gratings (RBGs). The concept of this kind of grating is shown in figure 24. The zeroth order of diffraction is reflected as by a mirror. The first order is dispersed into the quadrant of the incident radiation. The grids have one side with an oblate slope. For optimum grating efficiency one has to make sure, that the oblate slope shows into the dispersive direction.

Coherence is observed at wavelengths equal or longer than the bunchlength. For wavelengths shorter than the bunch, the radiation is incoherent. Thus, the shorter the bunch the more the spectrum is extended to shorter wavelengths. In the case of FLASH, one expects coherence in the infrared range. RBGs are the most efficient way to disperse this kind of radiation [11]. The efficiency curve for an RBG for an angle of incidence of 17° is given in figure 25. The region between 0.7 and 1.3 (wavelength/pitch) shows good efficiency for the first order and is thus called the 'dispersive window' for the grating. Wavelengths longer than this dispersive section are reflected as by a mirror. Thus, the filter grating (also RBG) has to be chosen to match the installed dispersive grating such, that the wavelengths being in the dispersive window for the dispersive grating are reflected into the zeroth order at the filter grating. As a rule of thumb, one has to choose twice the number of grooves/mm for the filter in comparison to the dispersive element to get an adequate filter. The efficiency curve is calculated with GSolver which is a simulation code based on vector diffraction theory [37]. The calculations with

GSolver are in excellent agreement to the measurements [11].

Each wavelength of the incident radiation spectrum is sent to different directions by the reflective grating (compare figure 24). If the arriving radiation has an incident angle of Θ_{in} to the normal of the grating and if Θ_m is the angle in the m-th order, the grating equation is

$$\lambda = d \cdot (\sin\Theta_{in} + \sin\Theta_m) \tag{28}$$

where d is the pitch size of the grating. The zeroth order is the one with mirror-like reflection. With equation (28) every wavelength within a diffraction order can be calculated. In addition, the resolution $\mathrm{d}\lambda/\mathrm{d}\Theta_m$ of a spectrometer can be derived from (28):

$$\frac{\mathrm{d}\lambda}{\mathrm{d}\Theta_m} = d \cdot \cos\Theta_m \tag{29}$$

The main consequence of (29) is that the resolution depends on the angle and therefore on the wavelength, as

$$\Theta_m = \arcsin(\lambda/d - \sin\Theta_{in}).$$

The resolution is then found in the following form:

$$\frac{\mathrm{d}\lambda}{\mathrm{d}\Theta_m} = d \cdot \cos(\arcsin(\lambda/d - \sin\Theta_{in})) = d \cdot \sqrt{1 - (\lambda/d - \sin\Theta_{in})^2} \tag{30}$$

where the trigonometric theorem $\cos(\arcsin(x)) = \sqrt{1-x^2}$ was used. To get an independence of the grating, one defines a normalized wavelength $\bar{\lambda} = \lambda/d$ with which (30) transforms to

$$\frac{\mathrm{d}\bar{\lambda}}{\mathrm{d}\Theta_m} = \sqrt{1 - \left(\bar{\lambda} - \sin(\Theta_{in})\right)^2} \tag{31}$$

3.2.2 The Pyroelectric Detector

The pyroelectric sensor is a thermal detector made of Lithium Tantalate which is known for exhibiting a large spontaneous electrical polarization for temperatures below the Curie-Point due to its ferroelectric characteristic. If the temperature of the $LiTaO_3$ alters, for example due to incident radiation, the polarization changes. This can be converted into an electric signal by placing electrodes at opposite edges of a Lithium Tantalate slice forming a capacitor. The charges induced in the electrodes by a change of polarization cause a voltage across the slice if there is a high external impedance (see figure 27 for visualization). The detector has a time constant of 4 µs, which means that it takes 4 µs until the signal decreased by a factor of $1/e$, where e is the Euler number. Such a signal will cover more than one channel of the analog-digital-converter (ADC), sampling at 1 MHz, even when having only one bunch emitting radiation (see figure 27).

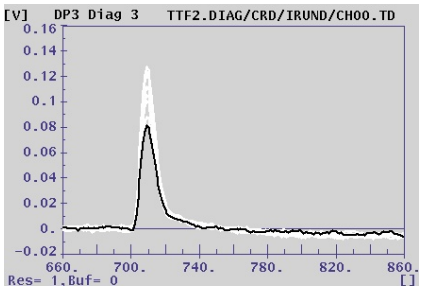

Figure 26: Readout signal of ADC. Due to the time constant the signal covers more than one channel for one bunch.

Due to the optical constants of the crystal and materials of the electrodes, interference occurs and this leads to resonant peaks in detector response. The capacitor is realized by a thin layer of chrome on the sensor (in range of nanometers) and a layer of gold underneath. Because any kind of metal is highly reflective for THz radiation, the fraction of the incident radiation passing through the whole crystal scatters back and causes the interference. Thus, even if one had a monochromatic signal as input radiation, the pyroelectric detector signal would show peaks in frequency domain. This can be measured with monochromatic radiation sources and it was done for the used pyroelectric detector[8]. This mea-

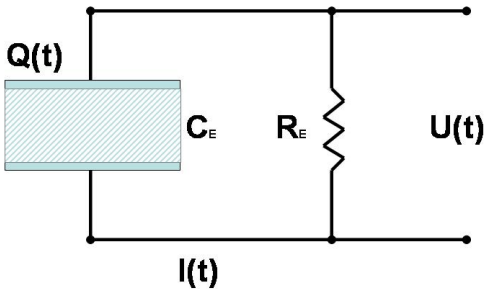

Figure 27: Principle of pyroelectric detectors. A slice of Lithium Tantalate is enclosed by two electrodes forming a capacitor. Altering temperature due to incident radiation causes change of polarization which leads to a voltage, because charges are induced in the electrodes.

[8]The pyroelectric detector used has the internal name X003, provided by the DESY group

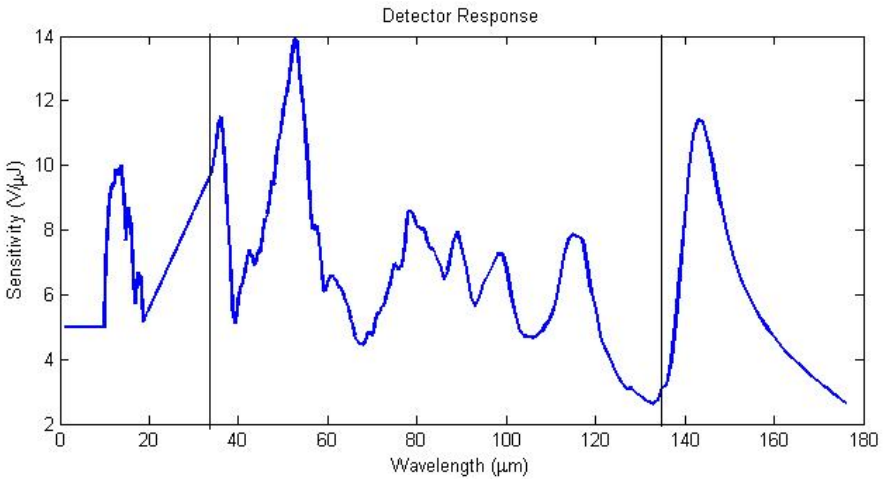

Figure 28: Detector response function. The two lines enclose the measured response. Above this range, the response function is extended to longer wavelengths by a fit due to interference effects of $LiTaO_3$. For short wavelengths measurements for a different but similar detector were used.

surement between 35 µm and 135 µm can be found in figure 28. For extending the response function to lower and higher wavelengths, one has to use both interference theory and data from similar measurements. For longer wavelengths than 135 µm the function is extended by a fit reproducing the resonance behavior of the $LiTaO_3$ layer. For shorter wavelengths below 35 µm, measurements done for a similar detector were used to approximate the response. Every spectrum taken with this pyroelectric detector has to be corrected by this response function.

3.2.3 The Final Spectrometer Design

Figure 29 shows the drawing of the current spectrometer design. The radiation enters the set-up parallel to the edge of the spectrometer's breadboard at the left side of the figure. The first element of the device is the filter grating which filters out all short wavelengths dependent on the grating constant. The angle of incidence Θ_{in} is designed to be 19°, whereas Θ_1[9] varies due to the position of the rotatable arm of the spectrometer (see figure 29). The angle between the normal and the tangent of grating is 58°±0.5°. Thus, Θ_1 =(58°-POS), where POS stands for the motor position with respect to the zero position in degrees. With g being the number of grooves per mm, the grating equation (28) transforms with λ in µm

FLA.

[9]From now, only the first order (m=1, compare with (28)) is considered, because higher orders are filtered by the first grating of the spectrometer.

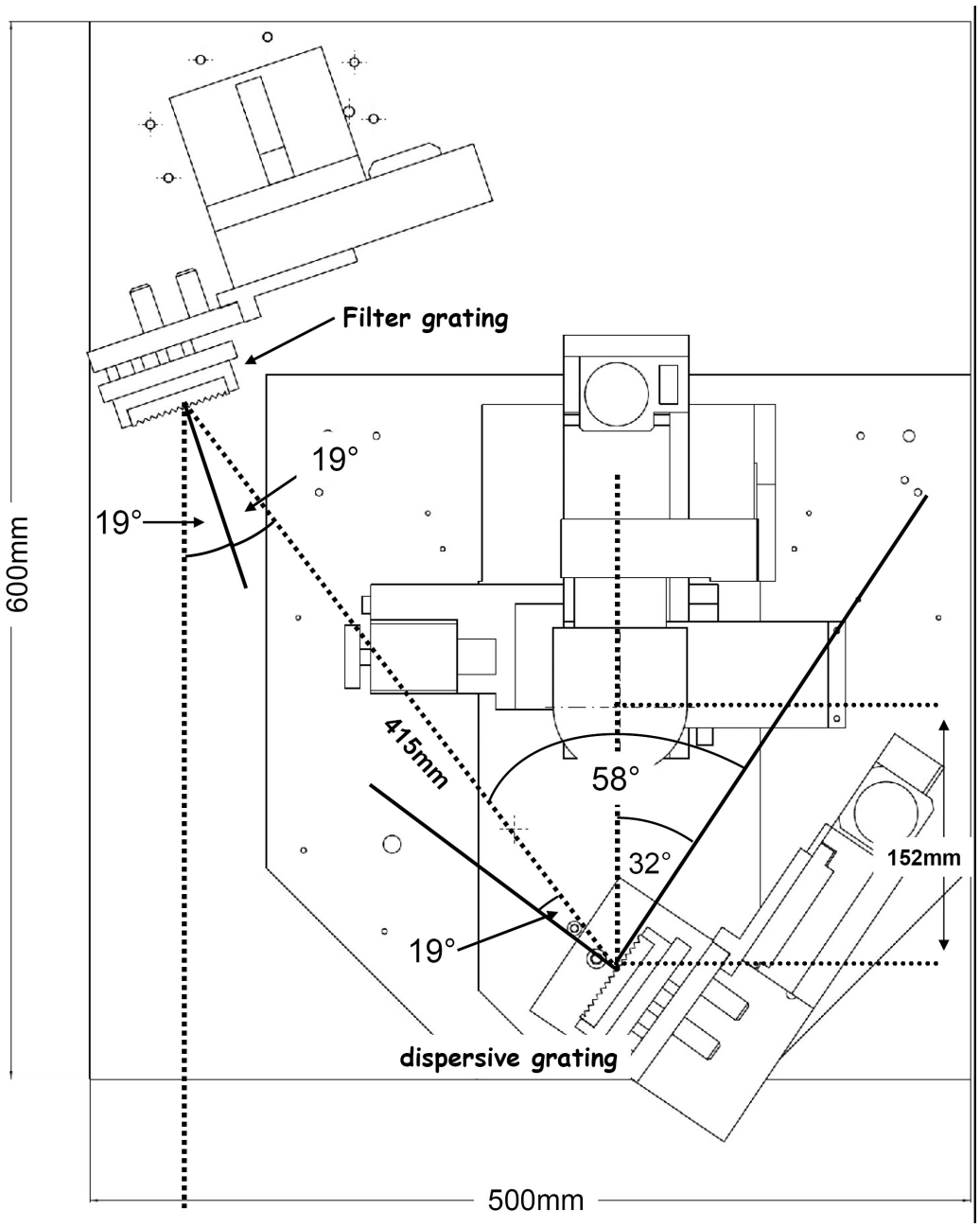

Figure 29: Drawing of current spectrometer design. The angles of incident and reflection are chosen for optimum grating efficiency.

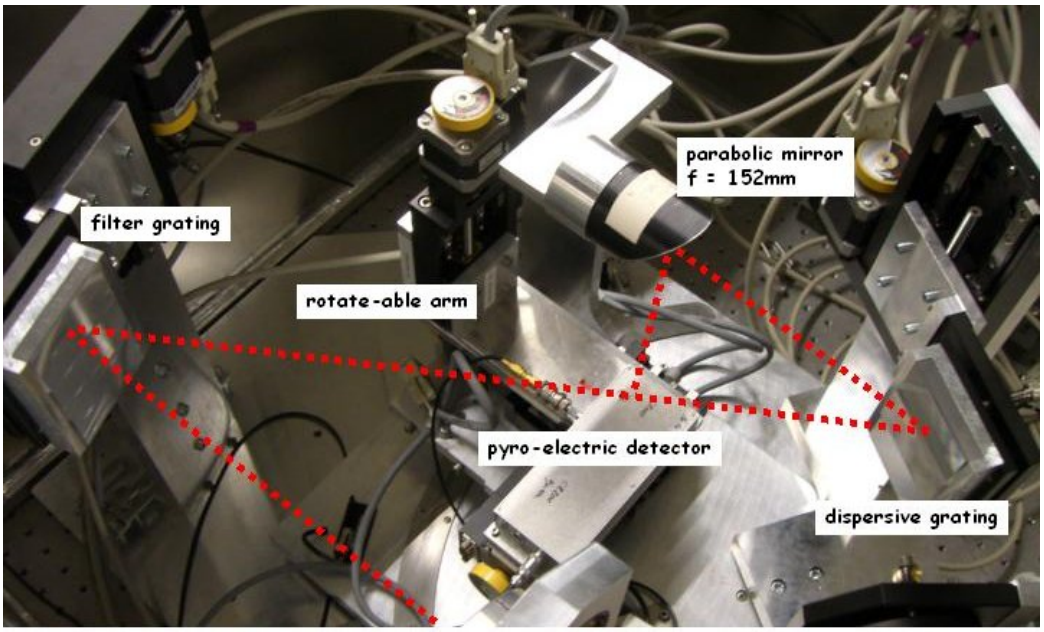

Figure 30: Picture of the spectrometer setup. The beam is indicated by a dashed line. THz radiation enters the device and hits the filter grating where wavelengths longer than the dispersive window of efficiency curve are reflected. The dispersive grating generates the first order which is gathered by a parabolic mirror. The focus coincides with a pyroelectric detector which measures the intensity.

into

$$\lambda = 1000/g \cdot (\sin\Theta_{in} + \sin(58° - \mathrm{Pos})) \tag{32}$$

For this spectrometer design, the rectangular grating dimensions are 28.5 mm x 58 mm. Thus, transverse beam sizes exceeding the grating height of 28.5 mm lead to a loss in intensity. To make sure that no significant cut-off occurs, a beam diameter below ≈25 mm is required. In the spectrometer setup the gratings are installed with grooves being vertical, which requires horizontally polarized light for optimum dispersion. The first order is dispersed into a dispersive section of 53° which has to be scanned by the rotatable arm of the spectrometer. The radiation is gathered by a parabolic mirror with an effective focal length of 152 mm. The pyroelectric detector is installed underneath the mirror at its focal point. In order to ensure a good focusing of the paraboloid, the incident radiation hitting on the mirror should be a parallel beam.

Another necessary information about the spectrometer is the resolution which can be calculated with equation (31). For a final treatment of the resolution $d\bar{\lambda}$,

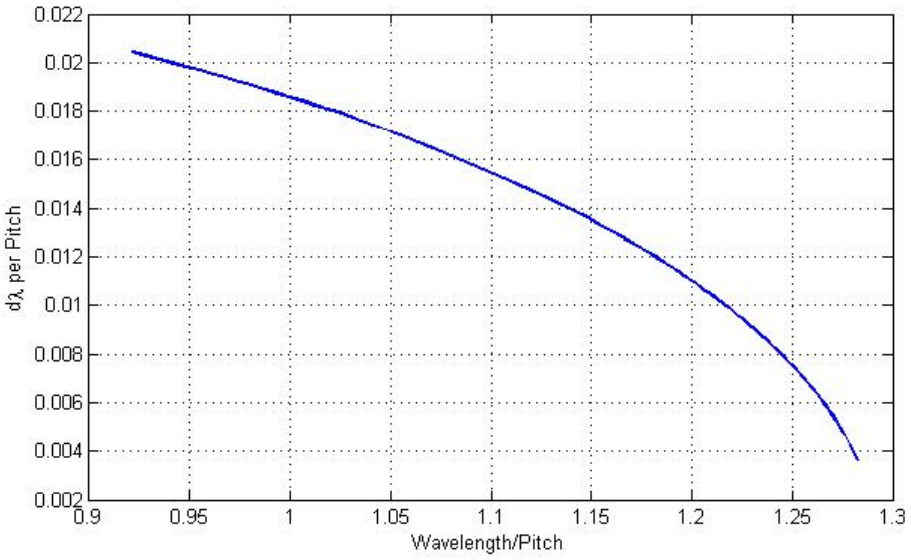

Figure 31: Resolution function of the spectrometer in dependence of the wavelength. Both axes are normalized to the pitch size.

one needs to determine the geometric acceptance $\Delta\Theta_1$ of the detector which follows from its width of 4 mm. With a distance of 152 mm to the parabolic mirror the angular acceptance is 26 mrad. Figure 31 shows the resolution function in dependence of the wavelength normalized to the pitch size for generalization.

Note, that the small value of the resolution function for long wavelengths per pitch leads to large uncertainties, if the intensity to be corrected within a spectrum at these wavelengths is small. Because the spectral intensity has to be divided by the resolution, a small value of the resolution function increases the intensity enormously, resulting in large errorbars and in the need of weighted fits, because the peak of the fit would move towards longer wavelengths, otherwise.

3.3 The Optics Calculations

By having a new spectrometer available for investigations of the infrared radiation from the IR undulator, an experimental setup in which the spectrometer can be operated must be designed. The main task of the development is the design of a preparative optical system which fulfills the requirements of the outcoupling port (e.g. aperture of the diamond window) and the spectrometer.

For this purpose, optics calculations and simulations have to be done to find the optimum set of mirrors and their optimum arrangement. In the first part of this section, definitions necessary for the treatment of optics are introduced. The

connection between optics and undulator radiation follows in the next section, where the theory of the treatment of undulator radiation as a laser-like beam is outlined. After the introduction into the simulation program used for the design, the calculations are presented in the last part of the section.

3.3.1 Gaussian Optics

There are several ways of analyzing optical systems mathematically. The most familiar approach is the theory of *geometrical optics*, which deals with radiation in the limit of a point-like focus ($\lambda \rightarrow 0$). Thus, all wave characteristics are neglected. However, in principle the wavelength dimension could be in the order of the dimensions of the optical system, which implies that the effect of diffraction determines the propagation of radiation.
Thz-radiation is in between the two limits of ($\lambda \rightarrow 0$) and ($\lambda \cong$ system dimension). Thus, the theory of *quasioptics* becomes applicable [38]. Quasioptics fills the gap between the two limitations by taking the beam diameter only moderately large compared to wavelength. A special case of the quasioptical treatment is the Gaussian beam propagation theory which includes the effect of diffraction in not such a strict manner. The treatment of optical systems within this formalism plays an important role in optical laser theory and in longer wavelength systems like the infrared sources.

From now, a highly collimated beam of radiation is considered having a well defined direction of propagation with some transverse deviations. With such a beam the so called *paraxial wave equation*, which is the basis of Gaussian beam propagation, will be developed.
The electric field component of an oscillation can be expressed as

$$E(x,y,z) = u(x,y,z)\exp(-ikz) \tag{33}$$

with z as the direction of propagation, $k = \frac{2\pi}{\lambda}$ the wave number and $u(x,y,z)$ the complex scalar function defining the non-plane part of the wave. Every single element of an electromagnetic wave propagating in a uniform medium satisfies the Helmholtz equation whose definition in Cartesian coordinates is

$$\frac{\partial^2 E}{\partial x^2} + \frac{\partial^2 E}{\partial y^2} + \frac{\partial^2 E}{\partial z^2} + k^2 E = 0, \tag{34}$$

which can be transformed to the so called *reduced wave equation* by applying (33) on (34)

$$\frac{\partial^2 u}{\partial x^2} + \frac{\partial^2 u}{\partial y^2} + \frac{\partial^2 u}{\partial z^2} - 2ik\frac{\partial u}{\partial z} = 0 \tag{35}$$

If the variation of the amplitude u along the path is small over a distance comparable to the wavelength and to the variation perpendicular to the axis of motion, the third term in (35) can be neglected. Thus, it follows

$$\frac{\partial^2 u}{\partial x^2} + \frac{\partial^2 u}{\partial y^2} - 2ik\frac{\partial u}{\partial z} = 0 \tag{36}$$

which is the *paraxial wave equation*. The solutions to the paraxial wave equations are the basis of the quasioptical theory - the Gaussian beam modes. These solutions are derived by switching to an axially symmetric cylindrical coordinate system which is the most convenient one for a system treated within Gaussian beam propagation. If z remains the axis of motion, r defines the perpendicular distance from and ϕ the angle to that axis, the wave equation will become

$$\frac{\partial^2 u}{\partial r^2} + \frac{1}{r}\frac{\partial u}{\partial r} - 2ik\frac{\partial u}{\partial z} = 0 \tag{37}$$

with u independent of ϕ caused by the axial symmetry. One simple ansatz for the solution of (37) is

$$u(r,z) = A(z)\exp\left(\frac{-ikr^2}{2q(z)}\right). \tag{38}$$

With its complex functions $A(z)$ and $q(z)$ this amplitude looks like a Gaussian distribution. Substituting u in (37) by (38) leads to the following relationship for $q(z)$:

$$\frac{\partial q}{\partial z} = 1 \tag{39}$$

Equation (39) can be solved easily (setting the reference point along the z-axis to 0):

$$q(z) = q(0) + z \tag{40}$$

which is known as the *Gaussian beam parameter*. If one takes into consideration, that q is complex the exponential part of (38) becomes

$$\exp\left(\frac{-ikr^2}{2q}\right) = \exp\left(\frac{-ikr^2}{2}\left(\frac{1}{q}\right)_r + \frac{kr^2}{2}\left(\frac{1}{q}\right)_i\right), \tag{41}$$

where r and i refers to the real and to the imaginary part of $\frac{1}{q}$. The imaginary part of (41) is a phase variation $\varphi(r)$ induced by a spherical wave front (see figure 32). Relative to a plane for a fixed position z this phase delay becomes

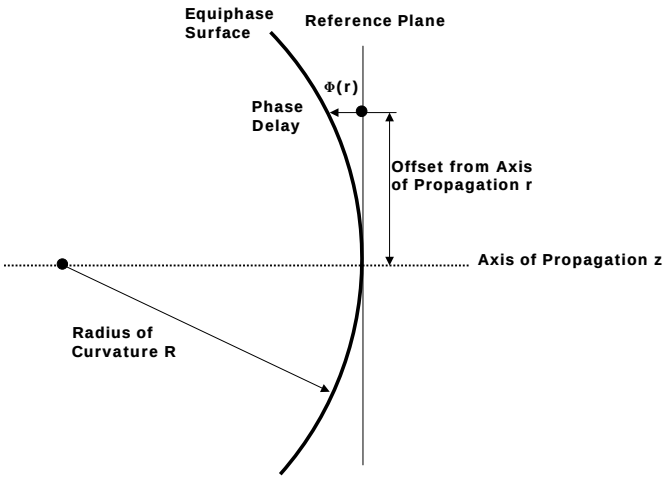

Figure 32: Visualisation of the simple solution of paraxial wave equation.

$$\varphi(r) \cong \frac{\pi r^2}{\lambda R}, r << R \tag{42}$$

with R being the radius of curvature. Thus, the real part of $\frac{1}{q}$ can be identified with the radius of curvature of the beam depending on the longitudinal position z

$$\left(\frac{1}{q}\right)_r = \frac{1}{R} \tag{43}$$

The real part of (41) contains a Gaussian function with the distance r from the axis of motion. A standard form of a Gaussian distribution is

$$f(r) = f(0)\exp\left[-\frac{1}{2}\left(\frac{r}{r_0}\right)^2\right] \tag{44}$$

with $f(r_0) = 1/e \cdot f(0)$ at $r = r_0$ (r_0 is also called the *standard deviation* σ of the Gaussian distribution). Transforming (41) into this form, q has to be expressed as

$$\left(\frac{1}{q}\right)_i = \frac{2}{kw^2(z)} = \frac{\lambda}{\pi w^2} \tag{45}$$

which leads to the definition of the *beam radius w* as the value of radius where the field is smaller by a factor of $1/e$ compared to the on-axis field. Going back to $z = 0$ the wave equation from (38) becomes

$$u(r,0) = u(0,0)\exp\left(\frac{-r^2}{w_0^2}\right) \tag{46}$$

where w_0 defines the beam radius at $z = 0$ called the *beam waist radius* or simply the *waist*. With this definition, expressions for the radius of curvature R and beam radius w as a function of the longitudinal position z can be derived:

$$R = z + \frac{1}{z}\left(\frac{\pi w_0^2}{\lambda}\right)^2 \tag{47}$$

$$w = w_0\left[1 + \left(\frac{\lambda z}{\pi w_0^2}\right)^2\right]^{0.5} \tag{48}$$

These equations form the basic parameters for the Gaussian beam propagation. As one can easily see, the waist is the minimum beam radius and at the position of the waist the radius of curvature is infinite which is the characteristic of a plane wave.

The radius of curvature changes during propagation. Close to the waist the beam is a plane wave with R going to infinity. Far from the source the wave becomes spherical. The *confocal distance* or *Rayleigh range* is defined as the distance, where the beam radius is increased by a factor of $\sqrt{2}$ with respect to the waist:The *confocal distance* or *Rayleigh range* is defined as the distance, where the beam radius is increased by a factor of $\sqrt{2}$ with respect to the waist:

$$z_c = \frac{\pi w_0^2}{\lambda} \tag{49}$$

With that the expressions can be rewritten in the following way

$$R = z + \frac{z_c^2}{z} \tag{50}$$

$$w = w_0\left[1 + \left(\frac{z}{z_c}\right)^2\right]^{0.5} \tag{51}$$

The beam can be divided into a *nearfield* with $z << z_c$ and a *farfield* with $z >> z_c$.

3.3.2 Undulator radiation as a laser-like beam

As mentioned in Section 2.1, there is a convenient concept for the radiation emitted within an undulator which was published in 2006 and 2007 [29, 39]. All concepts and equations in this section are taken from these publications.

The idea is to calculate from the far-field undulator radiation distribution a virtual source in the center of the device by simple Fresnel propagation. This source is comparable to the waist of a laser beam from which the undulator radiation field at any location behind the undulator can be determined. The theory is based on the ultra-relativistic characteristic of the electrons passing the undulator. Ultra-relativistic electrons emit highly directed radiation, which makes the paraxial wave equation introduced in section 3.3.1 naturally applicable. In optics dealing with visible light (like laser optics), however, the paraxial solution of Maxwell equation is only valid with the help of manipulations (e.g. insertion of apertures to limit the light propagation to a finite cone).

Note, that all equations in this subsection are in Gaussian units. This does not limit the utility of the expressions, because mostly the distributions are used in a relative context (e.g. relative distribution changes due to propagation or transmission through an optical system).

The radiation in an undulator is produced over the whole length L_U of the device, which leads to $\lambda_F = L_U$, where λ_F is the *formation length*[10] of the field. In paraxial wave theory, the far-field of radiation at $z_0 >> \lambda_F$ is the Fourier transform of the near-field at $z_0 \approx \lambda_F$. Let the observation angle of the undulator radiation be Θ with

$$\Theta^2 = \Theta_x^2 + \Theta_y^2$$

where Θ_x^2 and Θ_y^2 are angles measured from the undulator z-axis in the horizontal and vertical plane. Then one gets for the angular distribution of the electric field of the first harmonic in the far-zone

$$E_\perp(z_0, \Theta) = -\frac{K\omega e L_U}{c^2 z_0 \gamma} A_{JJ} \exp\left(i\frac{\omega z_0}{2c}\Theta^2\right) \mathrm{sinc}\left(\frac{\omega L_U \Theta^2}{4c}\right) \tag{52}$$

with the field being polarized horizontally. No vertical polarization exists in this approximation. K is the undulator parameter, $L_U = \lambda_U N$ is the undulator length, where N is the number of periods and $\mathrm{sinc}(x) = \sin(x)/x$. The frequency ω can be extracted from (22) and γ from electron energy. z_0 is here the longitudinal distance between the source and the point of observation. Finally, A_{JJ} is defined as

[10] The name comes from the fact, that within this length the radiation is emitted or the field is formed.

$$A_{JJ} = J_0\left(\frac{K^2}{4+2K^2}\right) - J_1\left(\frac{K^2}{4+2K^2}\right) \tag{53}$$

with J_n being the n-th order Bessel function of the first kind. The field distribution (52) is a spherical wave projected on a reference plane at z_0 with a phase factor (or phase delay) being dependent on Θ (compare with fig. 32). The peculiarity of the paraxial solution of Maxwell equation is the possibility to determine the field at the origin of the spherical wave (52) by propagating the wave backwards by applying Fresnel propagation. Doing this, the origin of far-field distribution ($z_0 = 0$) is found to be located in the center of the undulator. This source in the undulator center does not have any physical meaning, because realisticly the radiation is formated over the whole length of the undulator. Thus, it is a *virtual source*, which cannot be measured with a detector in situ, but imaged by an optical system in the far-field. This is due to the fact, that in far-field approximation it is not distinguishable, if radiation is emitted at the beginning or end of the undulator. Out of this concept one can calculate the axial-symmetric field distribution at the virtual source out of the far-field (52) getting

$$E_\perp(0, r_\perp) = i\frac{K\omega e}{c^2\gamma}A_{JJ}\left[\pi - 2Si\left(\frac{\omega r_\perp^2}{L_U c}\right)\right]. \tag{54}$$

The complete derivation is presented in [29]. The term $\mathrm{Si}(\cdot)$ indicates the sin integral function while $r_\perp$ is the distance from the z-axis on the virtual source plane. The field distribution (54) is the minimum transverse size with a planar wavefront. From this electric field at the virtual source, all distributions along the longitudinal axis behind the undulator can be determined.

All this leads to the fact that undulator radiation treated in the paraxial approximation is comparable to a laser beam. Because laser radiation is also highly directed, it is as well possible to determine the source from the far-field distribution. In contrast to undulators, lasers have a real source with a minimum transverse size due to diffraction which is called the laser waist. There are several similarities with a laser beam:

- The waist of the beam is located in the center of the device. In laser physics this device would be an optical cavity while in our case the virtual source is in the middle of an undulator with a waist defined by $w_0 = 0.9\sqrt{L_U\lambda/2\pi}$ (90% of the transverse size).
- The waist has a plane wave front and the transverse dimension of the waist is longer than the wavelength.
- In the previous section a Rayleigh range is defined by (49), which has its analog by an undulator source with $z_R = 0.8 \cdot L_U$.

To conclude, one can treat radiation from an undulator as a laser-like beam with a virtual source in the center of the device. Therefore, one can use codes like *ZEMAX* [40] originally developed for laser setups to propagate the wave front of a single-particle field through any optical system. Offsets or deflection angles in the electron motion with respect to the longitudinal axis result in an offset and deflection angle in the virtual waist plane.

3.3.3 *ZEMAX* as Simulation Tool

ZEMAX[11] is an optical design program which can simulate the propagation of a beam geometrically, with a Gaussian beam or with any user defined type of source. Therefore, *ZEMAX* is a program which can model, analyze and assist in the design of optical systems. The interface is organized in so called surfaces which can be just free space or an optical element. The first step after the implementation of different optical surfaces (lenses, mirrors or just apertures) is the use of geometrical optics. *ZEMAX* provides a functions called '3D Layout' showing the optical system by tracing rays geometrically through the surfaces. This function allows a check of position, direction and size of optical elements.

For beam propagation simulations the tool 'physical optics propagation' is the most important application. It is based on the fact, that propagation of light is a coherent process. As the wavefront travels through free space or any optically dense media, each part of the wavefront coherently interferes with all the other parts. Physical Optics Propagation (POP) is the ability of *ZEMAX* to use diffraction calculations to propagate the beam through the optical system surface by surface, including transfer of the beam through any ZEMAX surface type. When using POP, the beam is modeled using an array of points. At each point, the complex amplitude of the electric field is stored. The phase of these complex values determines the phase of the wavefront relative to a reference surface. The amplitude of the values determines the power of the beam. Vertical and horizontal size of the array change dynamically to fit best the beam during propagation.

To propagate the beam from one surface to another, either a Fresnel diffraction propagation (the propagating field is a spherical wave, originating at an aperture and moving along z) or an angular spectrum propagation algorithm (this technique expands a complex wave field into a summation of a finite number of plane waves) is used. *ZEMAX* automatically chooses the algorithm that supposedly yields the highest numerical accuracy. The problem at this point is, that one can not control, which tool is used for which surface and thus a certain skepticism remains towards of the numerical accuracy.

[11] Zemax Development Corporation, 4901 Morena Blvd. Suite 207, San Diego, CA 92117-7320 USA; www.zemax.com

The diffraction propagation and surface transfer algorithms work for any arbitrary beam; they are not limited to simple Gaussian beams. *ZEMAX* supports defining the initial beam as Gaussian or by data files with simulated sources (like numerical sources made with MatLab). Once the beam is defined, it may be inserted at any surface in the optical system.

The transfer function computed for all surfaces accounts for most important effects optical elements may have on the beam. These effects are for example

- The change in beam size due to diffraction or irregularities
- Beam behavior while passing apertures
- Polarization effects

Once the surface transfer function is applied, the beam may then propagate to the next optical surface. The surface by surface propagation proceeds through the entire optical system. The coordinate system of the beam travels along the chief ray. But it is due to user to define *coordinate breaks* or *tilts* rotating the coordinate system like it is required to keep the ray on track.

3.3.4 Optical Design

For the Zemax simulations done for this thesis, the initial beam was defined as a Gaussian waist. In Zemax, this waist w_0 is defined as [41]:

$$E(r) = E_0 \cdot \exp\left(-\frac{r^2}{w_0^2}\right) \tag{55}$$

with $r^2 = x^2 + y^2$ being the distance from axis and E_0 being chosen properly to yield the peak intensity in power per unit area as it is defined by the user. The corresponding Intensity $|E(r)|^2$ is therefore

$$I(r) = E_0^2 \cdot \exp\left(-\frac{2r^2}{w_0^2}\right). \tag{56}$$

To get the information about the content of the waist in terms of σ[12], the intensity has to be integrated over the surface element $\mathrm{d}A = 2\pi r \mathrm{d}r$. The total intensity is calculated with $r \to \infty$, the integrated intensity enclosed by the Gaussian waist is got by integrating from 0 to w_0. The fraction is thus calculated by

$$\frac{I_{w_0}}{I_{tot}} = \frac{\int_0^{w_0} I(r) \cdot 2\pi r \mathrm{d}r}{\int_0^{\infty} I(r) \cdot 2\pi r \mathrm{d}r} = 0.865 \tag{57}$$

[12] σ is the standard deviation of a Gaussian distribution.

Therefore, 86,5% of the total intensity is enclosed by the waist defined in Zemax, which corresponds to 2σ of a 2-dimensional axial-symmetric Gaussian distribution. For this, (56) becomes

$$I(r) = E_0^2 \cdot \exp\left(-\frac{r^2}{2\sigma^2}\right). \tag{58}$$

In section 3.3.2, the concept of the virtual source and the resulting treatment of undulator radiation as a laser-like beam was discussed. To simulate undulator radiation propagation with Zemax, using a Gaussian-beam approximation, requires a value of the initial waist. There are two possible approaches getting an initial waist. One is developed by O. Kozlov et. al.[13] and another way is derived in this thesis. The method of O. Kozlov et. al. uses the opening angle of undulator radiation given in section 2.2.3 as

$$\Theta = \frac{\sqrt{1+K^2/2}}{\gamma\sqrt{N}}.$$

This angle is used as the far-field divergence of a Gaussian beam. The relation between that divergence and the waist radius is

$$w_0 = \frac{\lambda}{\pi \cdot tan(\Theta)}.$$

With Θ being small, the angle is approximately equal to its tangent and thus, the two formula above can be combined to

$$\frac{\lambda}{\pi w_0} = \frac{\sqrt{1+K^2/2}}{\gamma\sqrt{N}}. \tag{59}$$

With the undulator equation $\lambda = (\lambda_U)/(2\gamma^2) \cdot (1+K^2/2)$ and the approximation $\sqrt{1+K^2/2} \approx K/\sqrt{2}$ for large K-Values, the $K^2/2$-term in (59) can be substituted and (59) becomes

$$\frac{\lambda}{\pi w_0} = \frac{\sqrt{\lambda\gamma^2/\lambda_u}}{\gamma\sqrt{N}} \quad \Leftrightarrow \quad w_0 = \sqrt{\lambda_U N}\sqrt{\lambda}.$$

With $\lambda_u N$ being the undulator length L_U, one finally gets for the initial waist

$$\frac{w_0}{1\,\mathrm{mm}} = \sqrt{\frac{L_U}{1\,\mathrm{m}}}\sqrt{\frac{\lambda}{1\,\mu\mathrm{m}}}. \tag{60}$$

[13] O. Kozlov et. al. have estimated an initial waist for Zemax simulations, but the derivation is not clear anymore. From personal communication only the basic ideas could be extracted. This was the main reason to determine the initial waist again.

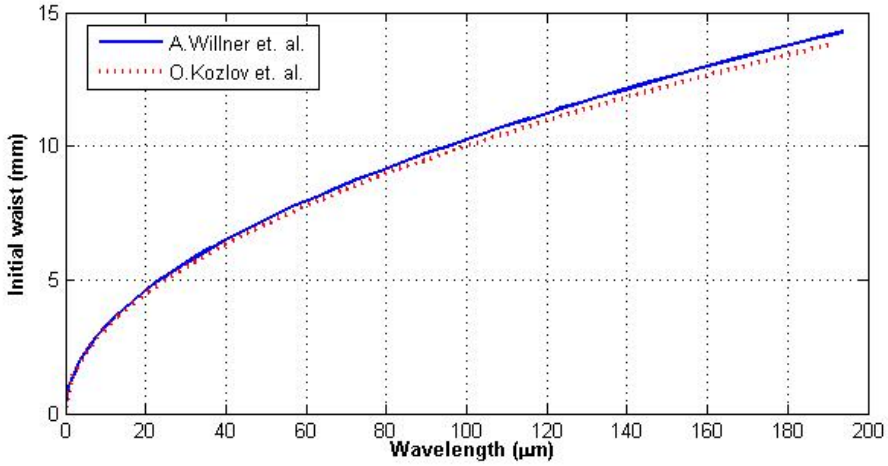

Figure 33: Initial waist determined by two different methods. Both curves are square root functions with basically the same scale factor.

O. Kozlov et. al. claim to get best approximation of far field intensity distribution with w_0 as the center of a spherical wave by substituting $\sqrt{L_U/\mathrm{m}}$ by a scale factor of 1.

In contrast to this empirical method, it is possible to calculate an initial waist from equation (52) in section 3.3.2 being the far-field of undulator radiation in dependence of the angle Θ and distance z from the source. The intensity is calculated from the electric field by

$$I(z,\Theta) = E(z,\Theta)\cdot E^*(z,\Theta)$$

where E^* is the complex conjugated of E. The integrated intensity is calculated by spherical integration

$$I_{int}(z) = \int_0^{\Theta}\int_{-\pi}^{\pi} I(z,\tilde{\Theta})\Phi\sin(\tilde{\Theta})\mathrm{d}\Phi\mathrm{d}\tilde{\Theta} = \int_0^{\Theta} I(z,\tilde{\Theta})2\pi\sin(\tilde{\Theta})\mathrm{d}\tilde{\Theta}. \qquad (61)$$

The total intensity is got by choosing Θ to be 2π. The next step is to find the angle $\Theta_{2\sigma}$ that yields 86.5% of the total intensity. Remember, the 86.5% fit to the 2σ radius of a 2-dimensional Gaussian distribution. Using this angle as the divergence of the initial waist, w_0 is calculated from

$$w_0 = \frac{\lambda}{\pi\Theta_{2\sigma}} \qquad (62)$$

Thus, in this method, the 2σ radius of the Gaussian distribution is applied to the

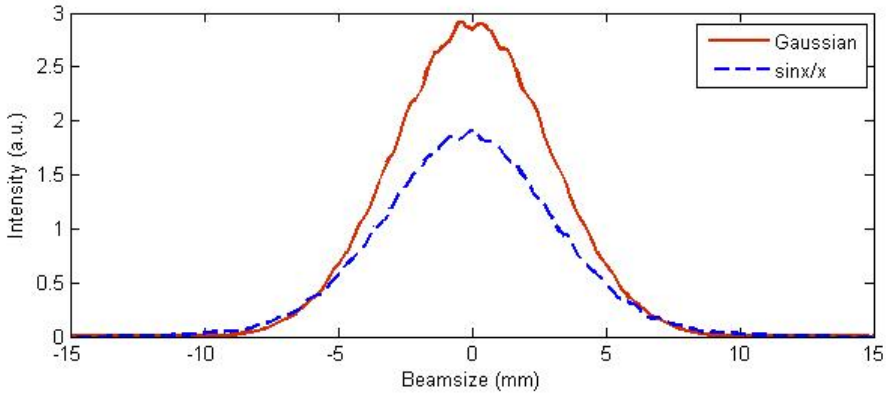

Figure 34: Comparison of the different Zemax sources propagated through an arbitrary optical setup. The Gaussian waist and the $\sin x/x$-source only differ by a scale factor.

far-field distribution of undulator radiation for getting the divergence of the initial beam waist.

Figure 33 shows the initial waist versus the undulator wavelength calculated with the two different methods. The curves have basically the same scale factor which leads to same results for both methods. The purpose of these considerations is to get a starting shape for beam propagation simulations. Figure 34 shows the comparison between the Gaussian waist and the virtual source presented in section 3.3.2 with its $\sin x/x$-shape. Both the Gaussian initial waist and the $\sin x/x$-source lead to profiles after propagation through an arbitrary system, differing only in a scale factor. The absolute transmission values are different, however. For the beam transmission in the infrared beamline, the crucial aperture is the electron beam pipe transporting the light from undulator to the first mirror. From simulations done for a wavelength of 100 µm, a 25% difference in transmission occurs comparing the two initial sources.

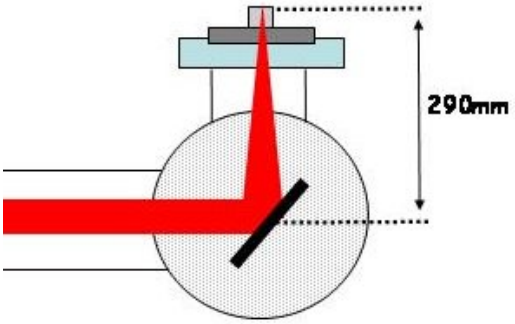

Figure 35: Out coupling at DP3. The distance between out coupling mirror and diamond window is 290 mm.

With the definition of the initial waist as the source in the simulation, the design of the optical system for the experimental station at DP3 can be devel-

oped. Figure 35 shows the outcoupling principle at DP3.
To avoid losses of intensity due to beam cut-off caused by the small aperture of the diamond window, the outcoupling optic has to be designed properly.

A common solution for such a problem is to choose a paraboloid as focusing mirror with focal length fitting to the distance to the diamond window from the mirror. Another solution would be a toroid or an elliptical mirror (the choice of the right mirror is made based on simulations). This leads to a very small beam size at the position of the window, if the focal point coincides with the position of the diamond window. At DP3 the distance between mirror and window is 290 mm. In addition to that, the beam should be deflected by 90 degrees. Therefore, an off-axis parabolic mirror (OAP) with an effective focal length of 290 mm is installed. Paraboloids focus all incident rays parallel to the axis to the same point (see figure 36).

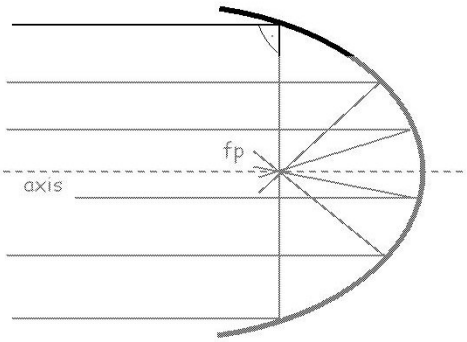

Figure 36: A parent parabolic mirror with focal point (fp) and incident axis. At DP3 a 90° deflection is needed and thus just a small region of parent paraboloid is used (black drawing). This part is then called off-axis paraboloid (OAP).

To avoid perturbing interference effects due to a finite thickness of the diamond (Etalon effects), the outcoupling window is wedged by an angle of 0.5°. In order to have a noticeable effect, the window has to be illuminated by a certain beam size. Therefore, it would be useful to have the waist not exactly on the window but slightly off target. Simulations with Zemax showed, that this is the case with a waist being slightly in front of the diamond window.

The spectrometer, however, has the following requirements concerning the preparative optics (see section 3.2):

- Incoming infrared beam has to have long a Rayleigh length and a waist behind the focusing mirror of spectrometer.
- Beam has to have a transverse spot size on gratings below 25 mm.
- Beam has to have horizontal polarization.

The two first items are fulfilled by the right choice of the second OAP picking up

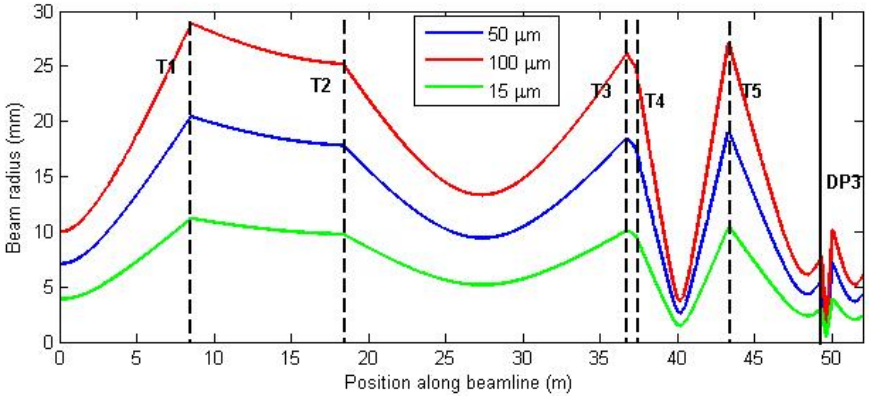

Figure 37: Beam radius over the whole infrared beamline up to DP3 for three different wavelengths. The 'T' stands for toroids as focusing elements.

the focus on the diamond window. For the third item, planar mirrors have to be used to rotate the vertical polarization of the radiation from the DP3 port.

The first step of the optical design within the experiment is to find the right focal length of the off-axis paraboloid (OAP) picking up the focus of the outcoupling mirror. For this, one has to choose a distance between the paraboloid (P2) and the detector of spectrometer. Two distances are fixed: The spacing between the two gratings is 415 mm from design and the gap between dispersive grating and mirror is 152 mm (see figure 29). For the planar mirrors, polarizer and possible filters one needs at least further 1000 mm, which leads to a distance between P2 and detector of around 1500 mm.

The first test for a Gaussian telescope is done with simple Gaussian optics without diffraction or apertures. Figure 37 shows the beam radius versus length of the beamline calculated by using the equations from section 3.3.1. Remember that the diameter of a Gaussian beam corresponds to 2σ. The beam does not arrive parallel at DP3. Thus, the out coupling mirror P1 with its focal length of 290 mm picks up a waist and focuses it to the diamond window. In addition to that, the waist is a little in front of the geometrical focus. This is the reason why best results are obtained with P2 being a little further away than expected from geometrical optics. A good solution found is a OAP with an effective focal length of 350 mm and a distance of 450 mm from the diamond window.

In figure 38 one can see the variation of the Gaussian telescope designed for DP3. The out coupling mirror with its focal length of 290 mm focuses the beam on the diamond window. Afterwards the focus is picked up by the second paraboloid with f=350 mm at a distance of 450 mm behind the window. The focus for the wavelengths of interest for the spectral analysis is not larger than 4 mm diameter

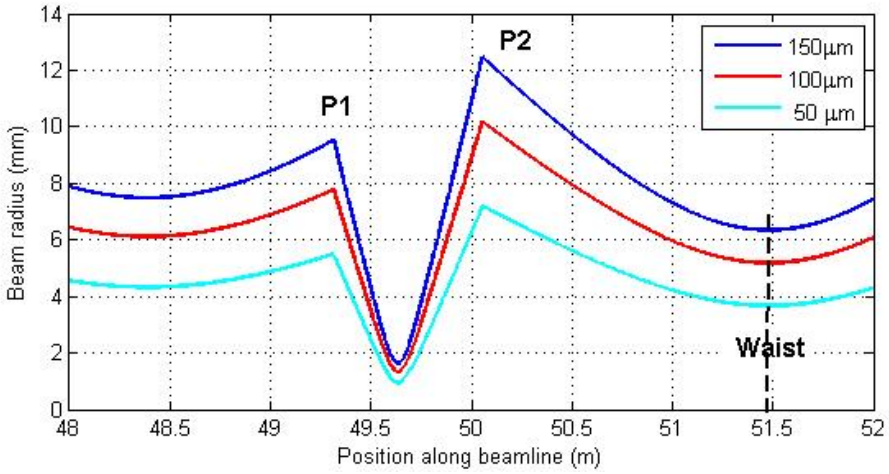

Figure 38: Gaussian telescope at DP3 with OAP P1 (f = 290 mm) as out coupling mirror focusing on diamond window and OAP P2 (f = 350 mm) as element picking up the focus. The distance to the window is 450 mm to get a larger Rayleigh length.

which is 20% of the whole aperture. The waist behind the second OAP (P2) appears at a distance of approximately 1400 mm, which is a little less than the estimated distance between P2 and the detector. Using these starting parameters from simple Gaussian optics, a detailed analysis has been done by simulations with ZEMAX.

Propagating the determined initial waist with Zemax through the whole infrared beamline and the experimental station at DP3 with the two OAPs found with simple Gaussian calculations, the following infrared beam characteristics are found:

- The waist of the infrared beam is situated at approximately 1900 mm behind the second OAP.
- The transverse beam size is 22 mm for 200 µm, 14 mm for 100 µm and 8.5 mm for 10 µm already at a distance of 1200 mm behind the second OAP.

These results give a lot of freedom in the spectrometer dimensions and arrangement of the optical system.

As mentioned in section 3.1, a vertical polarized infrared beam is provided at DP3. As long as the radiation is deflected by optical elements being within the oscillation plane, no change in the direction of polarization can be achieved. Thus, for turning the polarization, the beam needs to be vertically deflected. A

possible solution is a periscope, lifting the beam to a certain height and changing the polarization at the same time.

3.4 The Experimental Station

The usage of DP3 in the experimental hall instead of DP2 in the tunnel, which is also meant to be an electron diagnostic station, has several advantages. Experiments in the tunnel have to be designed for remote handling as access during machine operation is not possible. In addition, the instruments need to be protected against radiation damages. A setup which can be opened easily (for changing gratings, for example) is much more convenient.

But, there is also a disadvantage. The usage of DP2 instead of DP3 reduces the effort necessary for personal protection. Simulations have shown that the IR undulator radiation has high intensities especially in the short wavelength regime, which is dangerous for the retina of the eyes. Thus, precautions are necessary to avoid personal damages. In the tunnel, nobody has access during operation and therefore, no such precautions have to be taken into account.

Figure 39 shows the final setup of the experimental station at DP3. The radiation enters the setup with an angle of 11.3° due to the beamline design. Therefore, the preparative optical system has to correct for the angle in addition to the requirements already discussed in previous sections. This correction is necessary to ensure the right incident angle for the spectrometer gratings.

The first mirror of the setup is the parabolic mirror P2 picking up the focus of the outcoupling mirror. Afterwards, an optical chicane is implemented with two planar mirrors which does not affect the polarization but corrects for the angle. Then, a periscope with two further planar mirrors being upon each other lifts the beam to the height of the spectrometer being 200 mm above the incident height of the infrared radiation. In addition, the polarization is changed to horizontal one, as it can be seen in figure 40. The arrows represent the direction of polarization.

With this preparative optics developed in section 3.3, the infrared radiation fulfills the requirements of the spectrometer. Figure 41 shows simulated beam profiles at a wavelength of 100 µm for dedicated locations within the setup (compare with figure 39). An converging beam towards the spectrometer mirror is clearly achieved, the transverse diameter is below 25 mm on the first grating used as filter grating.

A polarizer is used, because the filter grating is very sensitive to falsely polarized radiation. If any vertical components in addition to the needed horizontal one arrives at the filter grating, higher orders occur leading to a spectrum not usable for spectral analysis. Thus, in order to avoid these higher orders, the polarizer is used. The better the linearity of polarization without polarizer, the lower the loss

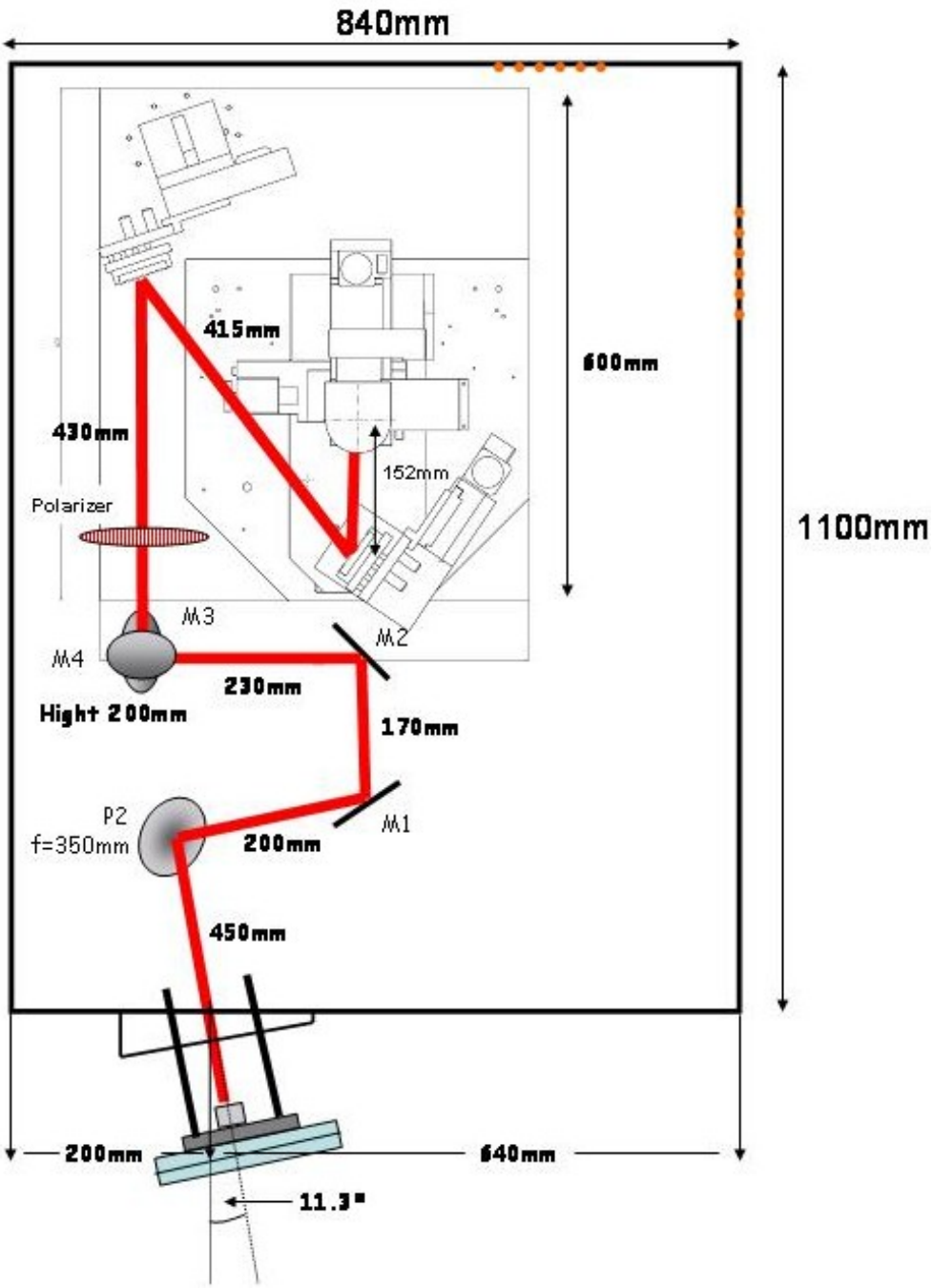

Figure 39: A sketch of the final setup at DP3. The incoming IR radiation is outcoupled through a diamond window and is deflected after 450 mm by P2, a parabolic mirror with f = 350 mm. For correcting the incident angle of 11.3 degrees, the beam passes an optical chicane with two planar mirrors. Then, a periscope out of two further planar mirrors brings the beam to its final hight of 400 mm and changes the polarization. In front of the filter grating of the spectrometer, a polarizer is installed.

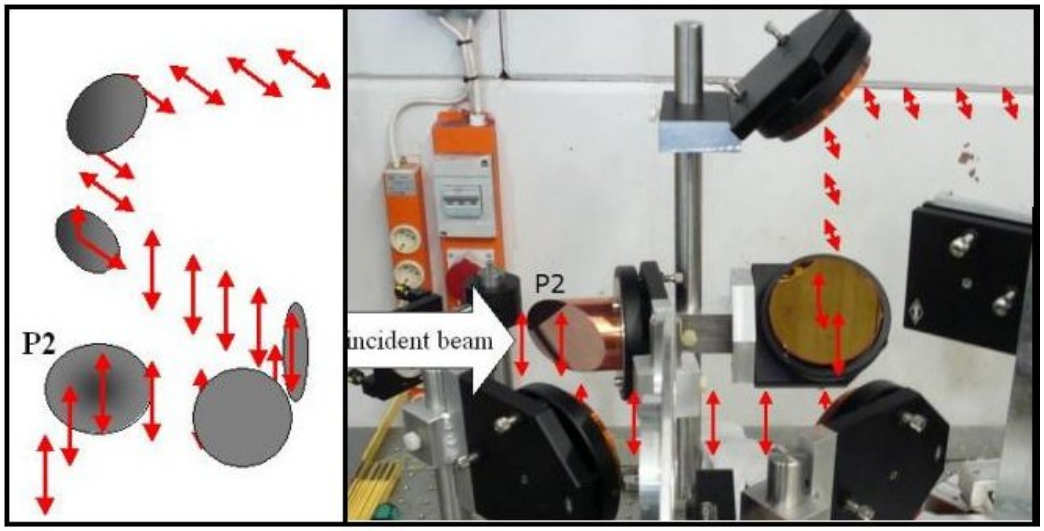

Figure 40: Change of polarization with optical chicane out of 4 planar mirrors. The angle of the beamline is corrected by the first planar mirror next to P2. With this optical chicane, polarization is horizontal as required by the spectrometer. First picture is a sketch of the optical system, the second one is a photo of real setup; the arrows represent the direction of polarization.

of intensity due to the polarizer.

Three gratings are installed on a holder, mounted on a linear mover, so that the gratings can be changed remotely. It must be made sure that always the right filter grating is assigned to the respective dispersive grating.

The whole setup is enclosed by a black plexiglas box. Because this material is transparent for infrared light, the box is lined on the inside with alluminium plates for radiation protection. This is important, because calculations showed very high pulse energies, which would classify the IR undulator as a class 4 laser [42].

The second intention installing a box is due to the need of reducing the water absorption within the setup. Air naturally contains water, which absorbs radiation with a strength dependent on the path length of the beam. Because a vacuum setup (which would be the best way avoiding water absorption) was not available, a version with flushing nitrogen was constructed. Pure nitrogen substitutes the air and thus reduces absorption. In figure 42 the water absorption lines for a path length of 1 m in air are plotted. In the wavelength regime from 1-200 µm, the absorption lines form a dense structure highly disturbing a spectral analysis. For comparison, the same lines after approximately 3 hours of flushing are shown as bright curve in figure 42. Purging the setup over more than 10 hours (e.g. over night) will minimize the influence of water.

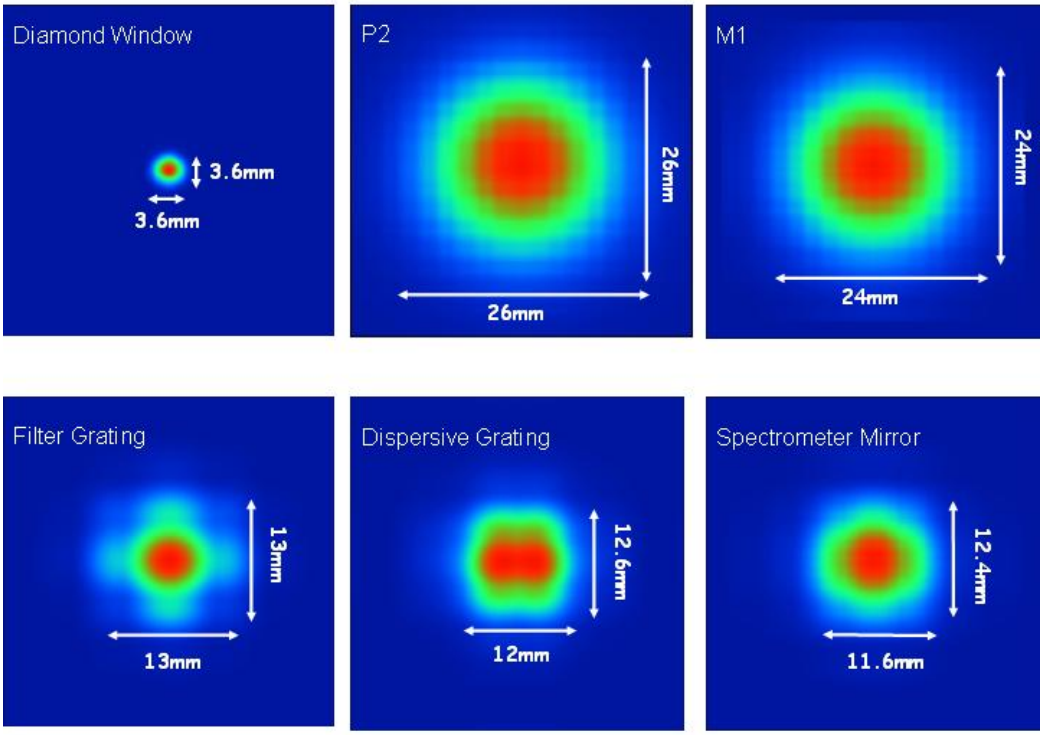

Figure 41: Simulated beam profile for several locations and 100 µm wavelength. The large divergence behind the diamond window is observable, as well as the beam convergence towards the instrument. Beam size at the positions of gratings is well below 25 mm, as required.

A picture of the whole experiment is given in figure 43. The beam entrance is at the left side, optical system, polarizer and spectrometer follow.

Even if only the zeroth order produced by the filter grating is used for the spectral analysis, nevertheless, higher diffraction orders appear in the dispersive section of the filter grating. To avoid disturbing effects due to reflection of these higher orders at the metallic wall of the box, absorber mats are inserted in the setup.

The spectrometer is controlled with a 'Beckhoff' control unit and driven with a code written with 'Matlab'. The possibility of changing gratings remotely gives the opportunity to scan over three grating ranges without opening the box. The work with a box purged with nitrogen is very time consuming which makes a vacuum setup desirable for future measurements at DP3.

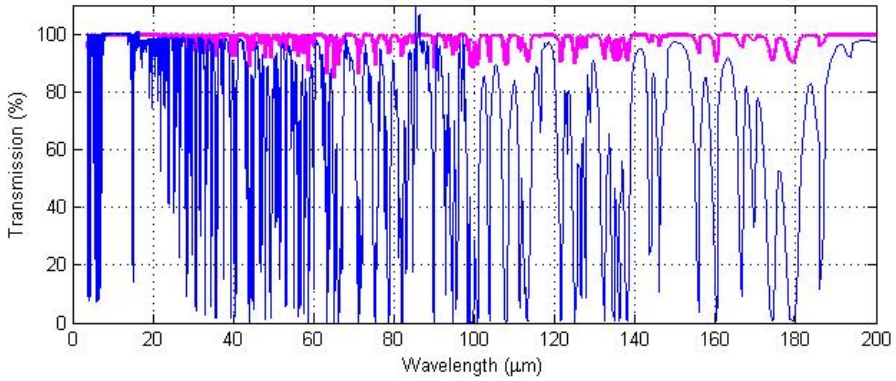

Figure 42: Water absorption lines for 1 m in air (courtesy of H. Delsim-Hashemi). The bright curve is the one for 3 hours of nitrogen purging.

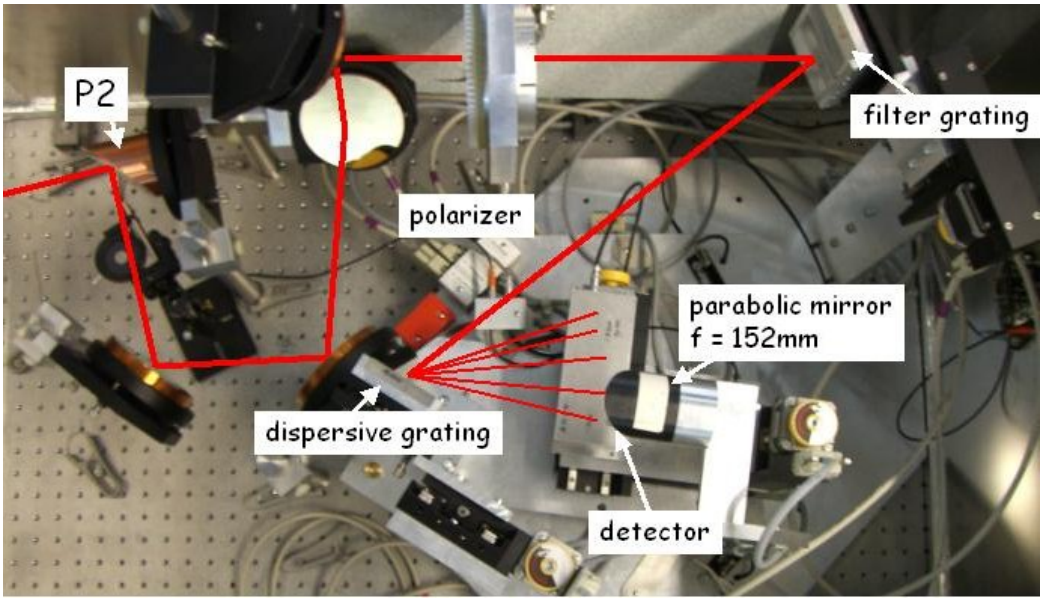

Figure 43: Picture of final set-up. Radiation enters at the left side, goes through the optical system and hits into the spectrometer.

4 Measurements and Results

After the first part of the work for this thesis has been successfully completed with the development of a new spectrometer and the construction of an experimental station at DP3, the second subject was the commissioning and spectral analysis of the FLASH infrared undulator.

The commissioning results are presented in the first section of this chapter, whereas the investigations done with the new spectrometer form the second section. As an additional measurement, transverse intensity profile scans were done at various locations at the experiment to investigate the accuracy of optics simulations.

4.1 Commissioning of IR Undulator

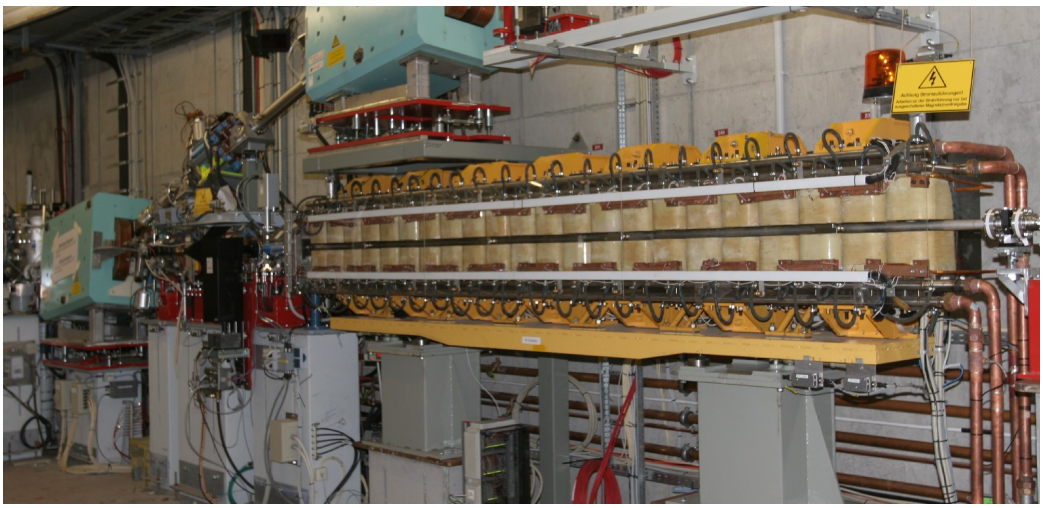

Figure 44: The infrared undulator in the FLASH tunnel, situated after the FEL undulators and in front of the electron dump.

After the preparative measurements described in section 2.2.2, the undulator was installed in the FLASH tunnel (see figure 44). The position of the undulator center is exactly at 240.295 m. Before the undulator could be used for experiments, it had to be commissioned during explicit shifts. The following goals had to be reached for final commissioning:

- Minimization of losses during beam transport through IR undulator.
- Response measurement of steerer magnets behind and in front of the undulator.

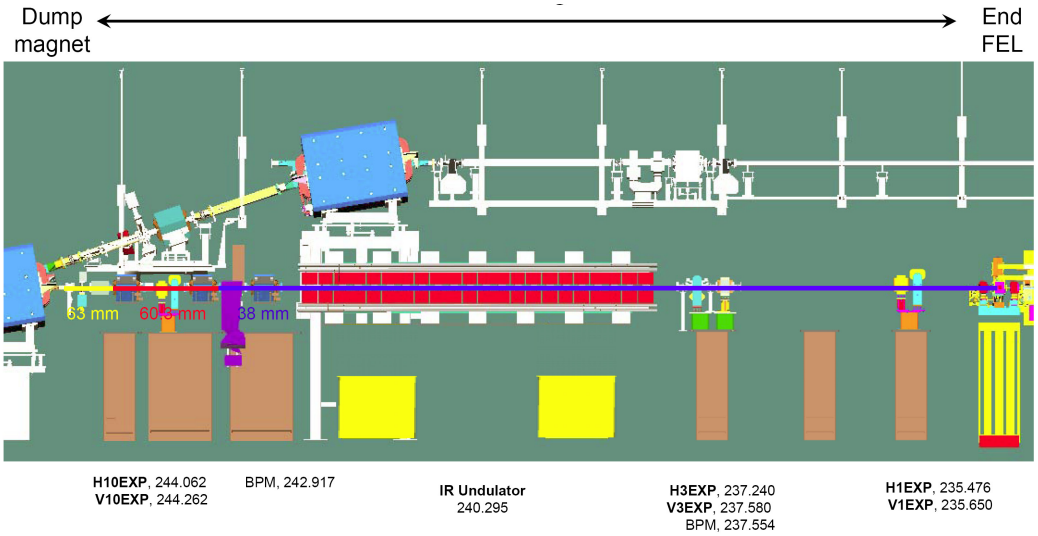

Figure 45: The EXP-Region of FLASH after the FEL undulators. Positions of Steerer magnets are marked, H stands for horizontal and V for vertical steerer. In addition, the BPM positions are given. All coordinates are centered positions in meter with the electron gun as reference.

- Measurement of vertical and horizontal steering range for tilt and offset in undulator.
- Implementation of a feedback system using Beam Position Monitors (BPMs) behind and in front of the undulator.
- Check of reproducibility of steerer set-up.

Figure 45 shows the whole EXP-region of FLASH which is defined as the area behind the FEL undulators in the tunnel. The IR undulator has been installed at 240.295 m downstream from electron source. In front of the undulator are two steerer pairs H1/V1 and H3/V3 and in addition to that a BPM slightly shifted from the position of V3 (H stands for horizontal and V for vertical steerer magnet). Steerer magnets are dipoles, which deflect the electron beam due to their magnetic field. The response measurements for the steerers, which show how many millimeters the beam moves by setting the magnet to a certain current, can be found in appendix A. In figure 46, the panel which is used to control the undulator power supplies and steerer magnets is presented. The panel shows a schematic sketch of the device with displayed numbers for the temperature and coil currents. The beam passes the undulator from left to right. The steerer control elements for H1/V1 and H3/V3 can be found in front of the undulator and for H10/V10 behind it. The BPM read outs are displayed at both ends of the undulator sketch.

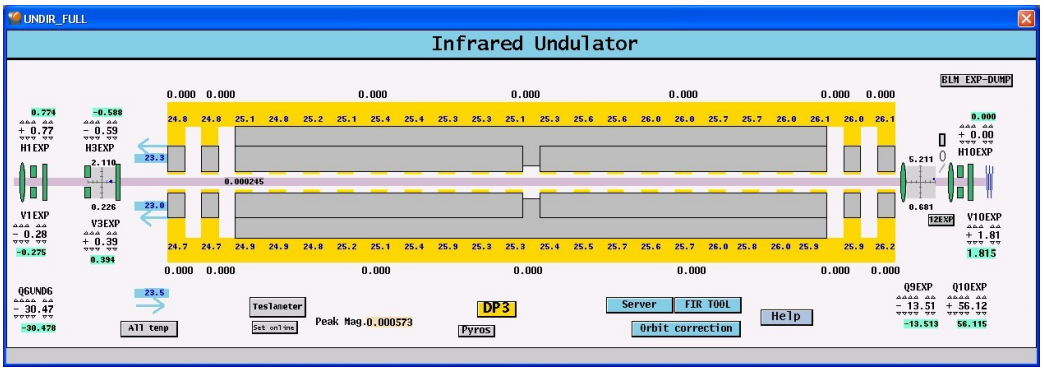

Figure 46: IR Undulator panel in control system of FLASH.

The first step of the undulator commissioning was to show that a beam transport through the undulator is possible without losses while the undulator is switched on and tuned to different K-Values. This was shown for several currents. High losses caused by the IR undulator due to electrons hitting the wall of beam pipe also result in signals on the beam loss monitors in the FEL section. This is due to particle showers produced by the electrons interacting with chamber wall.

The program operating the IR undulator (see figure 47) allows to choose a wavelength of radiation or a current for the main power supply. It is implemented in the machine control system DOOCS whereby the values can be read out by local programs written with MatLab[14], for example. The code of the undulator operation program drives all correction currents connected to a chosen main current or wavelength simultaneously. The wavelength is calculated from the current by using the corresponding magnetic field, the electron energy given by the energy server and the undulator period. Steerer settings were found in a first check for currents of 12 A, 50 A, 200 A, 435 A which leads to low losses in EXP area. The reproducibility was checked by going to -435 A and cycle the magnets afterwards. Going down to negative current destroys the hysteresis curve. After an initial cycling from zero to

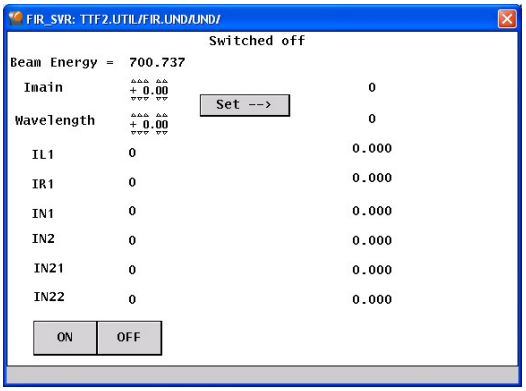

Figure 47: Server panel of DOOCS control system. One can set a value for current or wavelength.

[14]MathWorks Inc., see www.mathworks.com

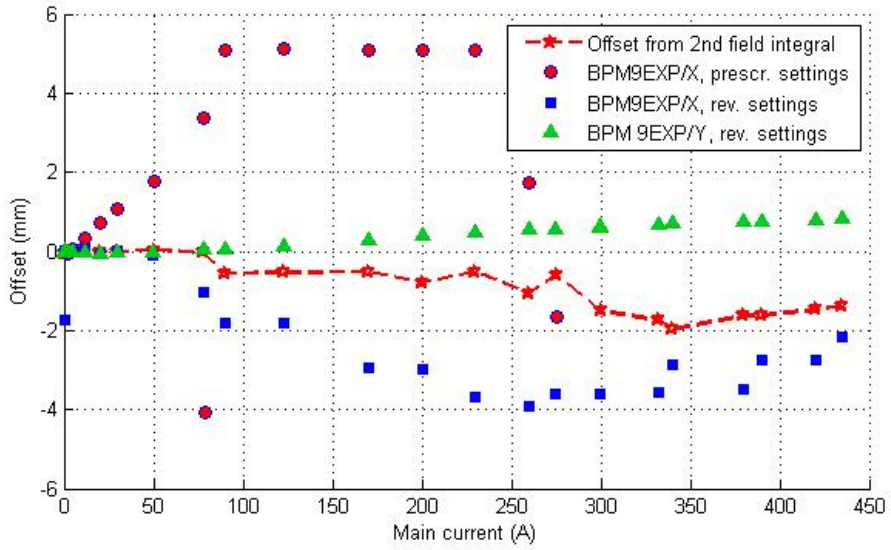

Figure 48: Offset measured with the BPM behind the undulator. The offset with the prescribed correction currents (circles) exceeds the linear range of the BPM. The offset with reversed settings (squares) has to be compared with the offset calculated from second field integral (stars). An unexpected vertical offset also occurs (triangles).

maximum current and back to zero should lead to almost the same BPM readings for given currents above, which was the case during this test within the measuring accuracy.

The currents of the correction coils used in the program differ from the ones found during magnetic measurements. All correction currents have the opposite sign compared to the prescribed quantities. This is due to the finding that the losses are smaller and thus the beam is less affected by the undulator with reversed settings. Reversing all correction currents has the same effect as reversing the main current. Thus, either the main current or the correction currents had the wrong polarity. In figure 48 the horizontal offset with the prescribed and reversed settings is shown. The curve for the prescribed values is flat between 80 and 230 A, because the BPM has a measurement range of ± 5 mm only. For values exceeding this range, the BPM shows its baseline which is at +5 mm. The occurrence of the baseline and the drop down of measurements points over 250 A imply a very large offset of the beam. For a perfect undulator the beam should not be affected by the insertion device. Field errors, resulting in non-vanishing field integrals, counteract this condition and lead to an offset which should be in our

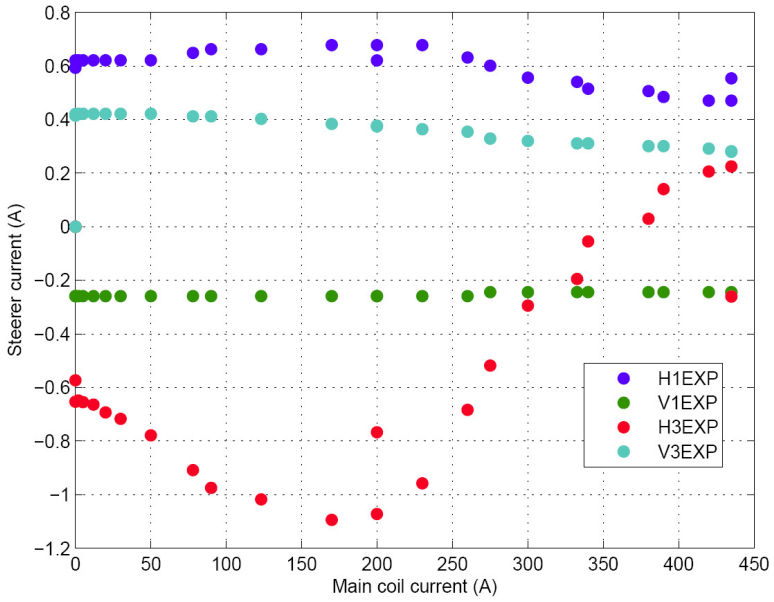

Figure 49: Steerer vs. undulator current to achieve zero offset in front of and behind the IR undulator.

case not greater than 2 mm (from the measured field integrals). The offset can be calculated from the second field integral by

$$\Delta x = \frac{ec}{E} \cdot I_2.$$

For comparison the calculated offset is inserted in figure 48. In contrast to the calculated maximum of 2 mm, the measured offset goes up to 4 mm even with the correction current reversed. Besides the horizontal offset measured with BPM 9EXP, the vertical BPM reading is also added to the plot in figure 48. Even though the vertical beam position should not be affected by the planar undulator, the BPM shows a vertical dislocation. A possible explanation could be a vertical focusing effect on the beam due to a misalignment of the beam trajectory. Note that a planar undulator has always a natural vertical focusing. But up to now, the vertical offset is not understood.

Such a great horizontal offset needs a strong correction. It is important to know, how the steerer magnets have to be driven for correcting this offset. The required steerer currents are shown in figure 49. As one expects from the plot in figure 48, the steerer H3 in front of the undulator corrects strongly the horizontal position.

The large offset is unexpected and, hence, the origin has to be investigated.

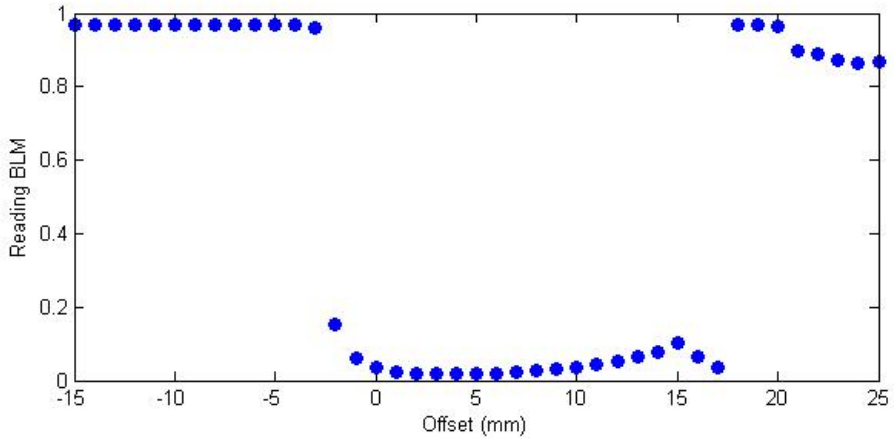

Figure 50: Horizontal aperture scan. Beam vertically centered on BPM. Signal of Beam Loss Monitor (BLM) shows an asymmetric region of free beam transport.

Being connected to the second field integral, the offset could be due to a misalignment of the electron path through undulator. To check this, an aperture scan is done by using both steerer pairs in front of the undulator H1/V1 and H3/V3. With equal but opposite fields in either both horizontal or vertical steerers, the beam can be displaced parallel to the incoming axis. Figure 50 shows a horizontal aperture scan with the result that the electron beam has much more space at one side of the 35 mm vacuum pipe compared to the other direction. This asymmetric behavior shows that the beam does not pass the undulator centered in the beam pipe by being centered on the BPMs at the same time. The aperture scan is done with help of a beam loss monitor (BLM) behind the undulator. BLMs basically detect the particle shower produced by interaction of the beam electrons with the vacuum chamber wall.

As a cross-check the vertical free aperture was also measured. Figure 51 shows two vertical scans, where one is done with the beam horizontally centered and the other with an horizontal offset of 10 mm. Only with the horizontal dislocation the vertical free aperture shows a value close to the expected 35 mm from chamber dimensions.

An inspection in the tunnel showed that the beam pipe in the undulator was bend in a banana-shape with its apex almost in the center of the device. After correction of beam pipe shape, the aperture scan was repeated and, as seen in figure 52, the aperture is much more symmetric and larger in comparison to the scan before the correction.

These investigations were done, because of an horizontal offset of the electron beam passing the undulator which was much larger than expected from field

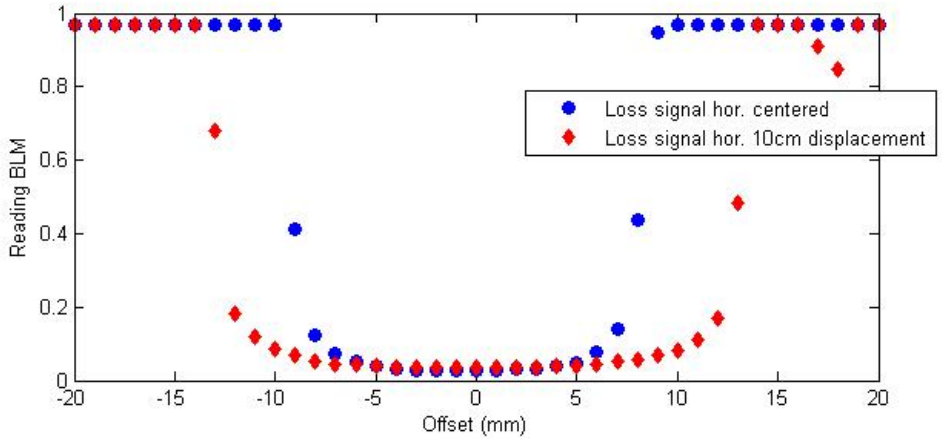

Figure 51: Vertical aperture scan. The curve with horizontally centered beam shows a very small free aperture. With horizontal displacement of about 10 mm the vertical aperture increases.

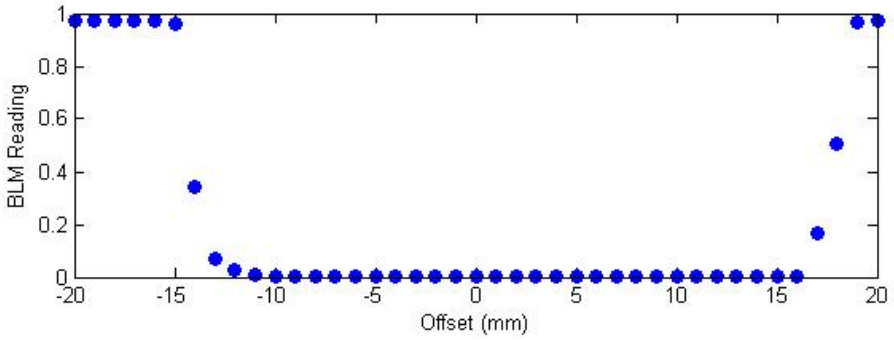

Figure 52: Aperture scan after the straightening of the vacuum beam pipe.

integral measurements. The remeasurement of the beam offset leads to an improvement of the result: Figure 53 shows the remeasurement of the offset. With a maximum offset of nearly 2.5 mm, the result matches reasonably well to the expected offset calculated from the second field integral.

To minimize losses in the electron pipe, a feedback was developed. This feedback program tries to stick to the values determined by the user for BPM positions in front of and behind the undulator by driving the steerer magnets simultaneously.

A measurement of the magnetic field produced by the main coils and by the different correction coils can be found in appendix B. The measurements were done with a hall probe fixed at a position outside the gap.

After the final commissioning of the IR undulator, first investigations into the infrared radiation of the device have been started.

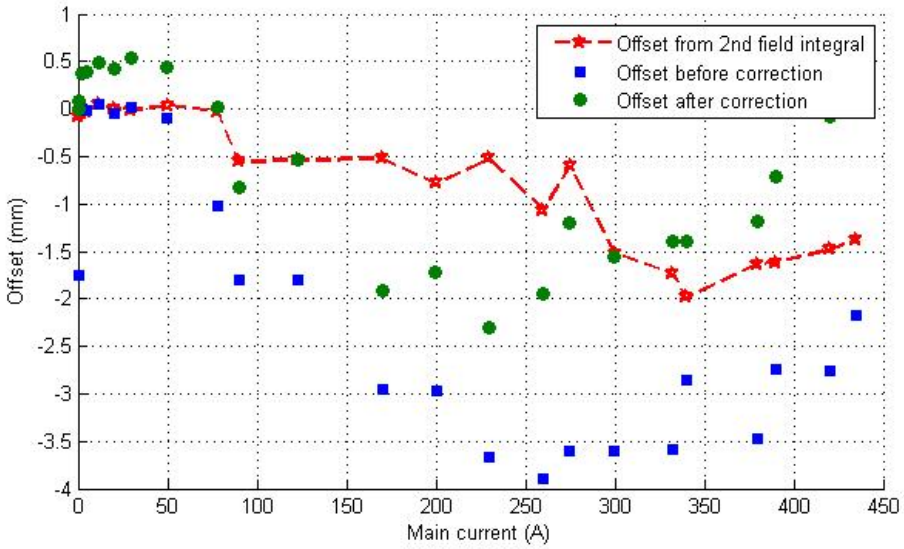

Figure 53: Offset behind the undulator (BPM 9EXP/X) after mechanical correction of beam pipe. As comparison the offset before straightening and calculated offset is plotted also.

4.2 Spectral Investigations into the IR undulator

4.2.1 Wavelength calibration

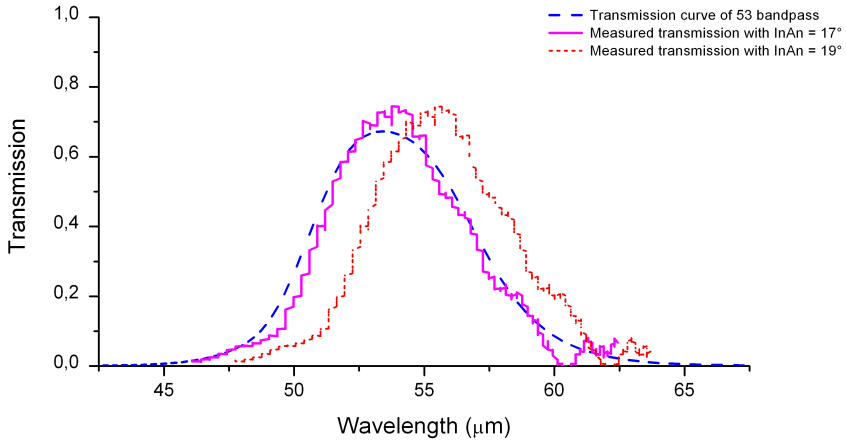

Figure 54: Wavelength calibration measurement. The dashed line is the filter transmission curve of band pass 53 µm, where the measured transmission is calculated from two spectra recorded with and without filter. The matching is found with an incident angle of 17°. As comparison, the transmission curve for an incident angle of 19° is also plotted.

The wavelength of dispersed radiation is calculated with (32):

$$\lambda = 1000/g \cdot (\sin\Theta_{in} + \sin(58° - \mathrm{Pos})).$$

The spectrometer is designed to have an incident angle Θ_{in} of 19°, which was checked with an alignment laser during installation of the spectrometer setup at DP3. But the invisible THz-radiation could have a different path through the optical setup which would result in a different incident angle. A wavelength calibration is necessary before the measurements starts. For this purpose, two spectra are taken with and without a bandpass filter under otherwise same conditions.

The undulator was tuned to 50 µm and the spectra were taken in air. As filter a 53 µm band pass was used. The transmission is calculated by dividing the spectrum measured with filter by the one recorded without. Figure 54 shows the result of wavelength calibration. Matching was found with an incident angle of 17°±0.5°. With this measurement, expression (32) for lambda becomes

$$\lambda = 1000/g \cdot (\sin(17°) + \sin(58° - \mathrm{Pos})). \quad (63)$$

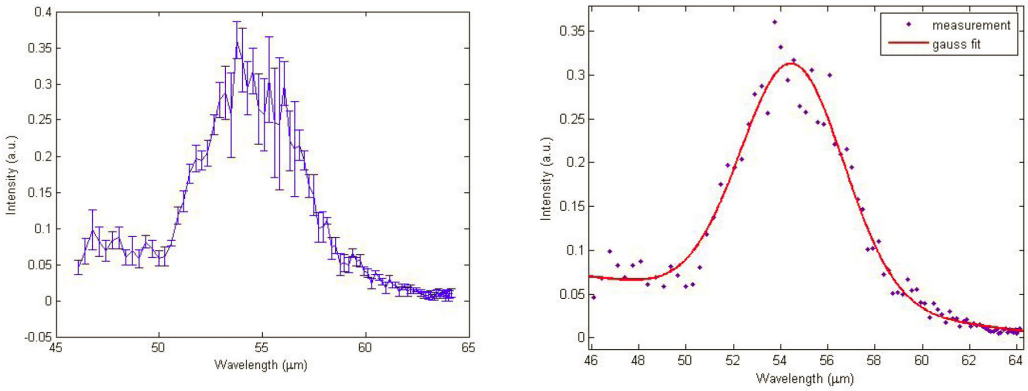

Figure 55: Undulator tuned to 50 µm at an electron energy of 696 MeV. Left plot shows recorded spectrum around the fundamental. Errorbars are due to fluctuations of the machine. The right plot shows the corresponding Gaussian fit.

To demonstrate the sensitivity of the calibration, the transmission curve connected to an incident angle of 19° is added in figure 54.

4.2.2 Wavelength shift

The first measurements were done for an investigation into the first harmonic of the undulator radiation. The infrared undulator was tuned to different wavelengths and spectra were recorded. Figure 55 and 56 show two example spectra with the undulator being tuned to 50 µm and 85 µm, respectively. On the left-hand side, the recorded spectra is plotted. Each measurement point is averaged over 8 shots, the errorbars indicate the standard deviation. The origin is mostly machine fluctuations. The spectra are corrected for grating efficiency and detector response. Additionally, the background measured with undulator being at zero current is subtracted. On the right-hand side, a corresponding fit is shown being a first order polynomial added to a Gaussian to increase the accuracy.

The FWHM of the peak in figure 55 is 6.4±0.7 µm, which results in a width of 11.8%±1.3%. In figure 56 the FWHM is 9.1±1 µm or 10%±1.4%. The errors are due to the wavelength calibration and the measurement of the angle between the normal of the dispersive grating and the zero-position of the rotatable spectrometer arm.

From section 2.1 one can calculate the width $\Delta\omega/\omega = 1/kN \approx \Delta\lambda/\lambda$ being around 11% for the fundamental ($k = 1$) with undulator period $N = 9$. Thus, the observed lines represent the fundamental of the spectrum.

The peak wavelengths determined from the fits are 54.4±1.3 µm (±0.5 µm), where the first error is due to statistics of the fit and the second error in brack-

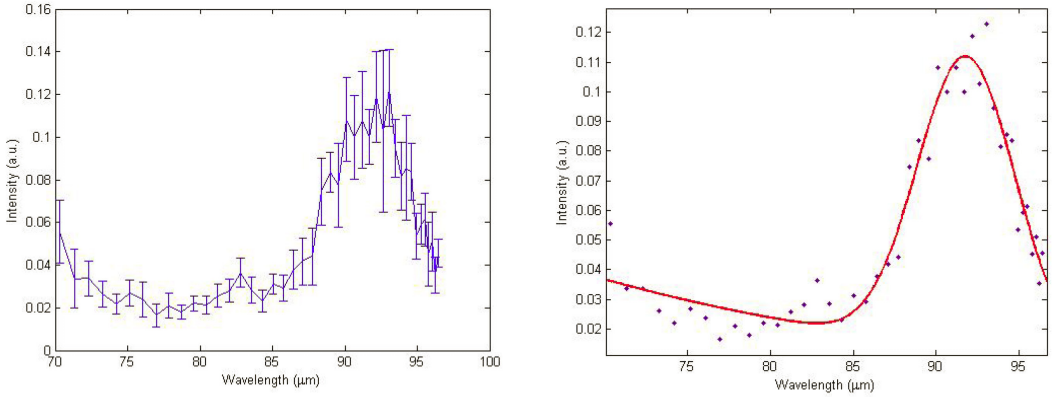

Figure 56: Undulator tuned to 85 µm, 507 MeV electron energy.

ets is the systematic error. The second spectrum shows a peak at 91.8±0.4 µm (±0.7 µm). The measured wavelength is shifted towards longer wavelengths compared to the undulator tune values of 50 and 85 µm. The fundamental for 50 µm is shifted by $9\% \pm 1\%$ and the fundamental for 85 µm appears at a wavelength $8\% \pm 1\%$ longer than expected.

The wavelength calculation is based on the undulator equation (21). The magnetic field depends on the current of undulator coils. If the assumed value of the current differs from the actual, a wavelength shift would occur due to a different K-Value. Investigations showed, however, that the reading of the coil current has an accuracy of about 10^{-4}.

Another parameter used for wavelength calculation is the electron energy. The IR undulator operation program uses the value from the energy server. This program provides a rms energy averaged over the whole bunch. The energy is determined as follows [43]: In front of the FEL undulator a dispersive section exists with two copper collimators to eliminate off-energy particles. Three BPMs are installed there, two in front of and one behind the dipole which bends the bunch into the dispersive section. The first two BPMs measure the incoming axis of the beam, which corresponds to the the center-of-mass (CM) position of the bunches. The BPM behind the dipole measures the CM position after the deflection, which depends on CM energy.

From section 1 it is known, that the bunch has a leading spike due to nonlinearity of longitudinal phase space distribution. From the FEL undulator it is well-established to introduce a so-called 'fudge factor' to match the electron energy to the measured FEL wavelength, because only the leading spike has the current required for the lasing process. The energy at the front end of a bunch is lower than the CM energy which leads to higher wavelength of the emitted photons. From experience, the fudge factor varies between 2 and 5%. These numbers

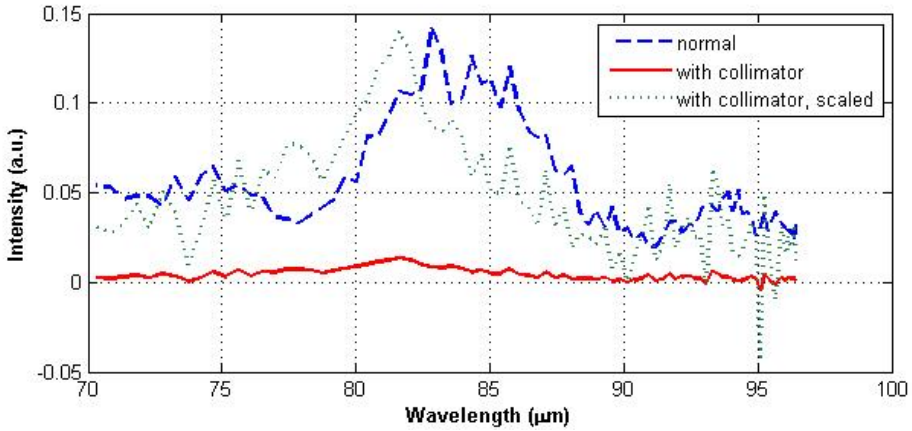

Figure 58: Spectra with undulator tuned to 76 µm, with measured wavelength 10% longer. The solid line is the spectrum recorded with collimator cutting the head of the bunch. To compare the peak wavelengths, the spectrum of the cutted bunch is also plotted with intensity scaled to match the usual spectrum.

depend on the quadrupoles and sextupoles (called 'optics' in accelerators) within the dispersive section. With these magnets the lasing region within the bunch can be changed without influencing the CM energy, because the emittance which matches the optical setting changes.

The radiation produced within the infrared undulator is dependent on the longitudinal form factor (frequency domain) or charge distribution (time domain) of the bunch. In contrast to the FEL spectrum, the infrared spectrum does not depend on transverse effects, so the emittance is not an important quantity for the coherent process in this wavelength regime. Within the leading peak of the bunch high current occurs and therefore a high charge density (compare figure 57). The short structure with high charge density leads to coherent radiation in the infrared regime. This implies, that the radiation produced within the IR undulator has a component which also originates from the leading peak of the bunch. The strength of the contribution depends on the form factor. The collimator of the first bunch compressor was used to cut the head of the bunch in the dispersive section. Figure 58 shows a comparison between spectra taken with undulator tuned to 76 µm. The

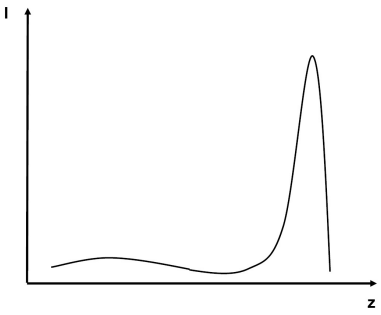

Figure 57: A rough sketch of the bunch structure with a leading head due to non-linearity in longitudinal phase space.

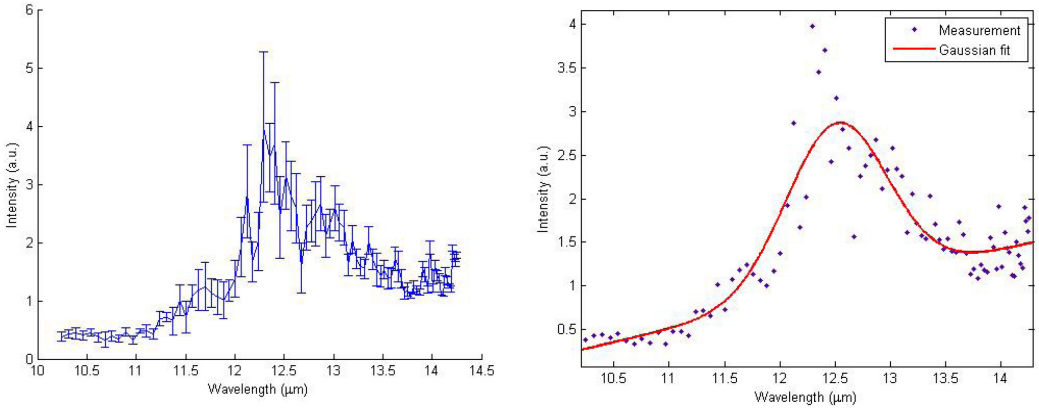

Figure 59: Spectrum with undulator tuned to 11.5 µm and electron energy of 699 MeV.

intensity decreases and a small peak can be found at a shorter wavelength than before. Note, that this technique has to be treated carefully, because the electrons can be in the head at the first bunch compressor and in a different part of the bunch after the second one. But nevertheless, the charge decreased at least by a factor of two during the insertion of the collimator, which indicated that a region of high current was cut. Additionally, the lasing was completely suppressed. The test gives an idea, that there is a dedicated region for the emission of strong infrared radiation.

The amount of the wavelength shift varies dependent on the status of the machine (compare figure 60 in section 4.2.3). Thus, the contribution of the error due to the difference between the CM energy and the energy of the radiating part of the bunch seems to be dependent on machine settings.

A further parameter which can lead to longer wavelengths is a non-vanishing observation angle. The central part of the IR beam is cut away by the aperture of the outcoupling mirror. From (21), the undulator wavelength shifts towards longer wavelengths with increasing observation angle. The distance between undulator and first mirror is 7.7 m. With an aperture of 10 mm this corresponds to a minimum angle of 0.6 mrad which leads to a wavelength shift of 0.1% for maximum K-Value and a shift up to 2.5% for small K (e.g. $K = 10$) and high electron energy (1 GeV). This implies an increasing influence of the aperture for decreasing undulator wavlengths.

Figure 59 shows an example spectrum for a shorter wavelength. For a tuned wavelength of 11.5 µm the fundamental is found to be at 12.5±0.1 µm(±0.1 µm), which corresponds to a shift of 9%±0.8%. The influence of the hole at an energy of 699 MeV and a K value of 16 is about 0.6%. For the rest of the thesis, the wave-

length calculated with the CM electron energy will be called 'tuned wavelength'.

4.2.3 Multiple peak spectra

The following measurements were done with the FEL operated in SASE-mode and an CM electron energy of 699 MeV. Figure 60 shows spectra recorded with tuned wavelengths of 50, 52.5 and 55 µm with appearance from top to bottom. As in previous figures, on the left side the real spectrum is presented, while the plot on the right side is the corresponding Gaussian fit. The most obvious difference to figure 55 is the occurrence of additional peaks. The upper spectrum corresponding to tuned wavelength of 50 µm shows a small additional peak next to the fundamental. With increasing wavelength the second peak sticks to the fundamental and moves about the same distance in µm. In addition, a third peak becomes visible and occurs completely in the last spectrum (55 µm). The displacement between the two peaks in the upper spectrum is $\approx 14\%$ and in the middle spectrum $\approx 13\%$. The last spectrum containes three full peaks which have distances of about 11% from each other.

Tuned wavelength	Fundamental/µm	Second peak/µm	Third peak/µm
50 µm	55.6±0.1(±0.5)	48.4±0.2(±0.5)	-
52.5 µm	58.3±0.1(±0.5)	51.4±0.2(±0.5)	-
55 µm	60.2±0.1(±0.5)	53.7±0.2(±0.5)	47.9±0.1(±0.5)

Table 2: Peak-wavelengths of spectra in fig. 60. Again, the first error is due to statistical accuracy of the fit, whereas the second one written within brackets is due to systematic errors.

The peak wavelengths determined with Gaussian fits are listed in table 2. The shift of the fundamental is higher compared to spectra in figures 55 and 56 being 11%±1.2% for 50 µm, 11%±1.2% for 52.5 µm and 9.5%±1.1% for 55 µm. This could be due to a different setting of the machine. As discussed above, the quadrupoles and sextupoles can change the FEL lasing-region within the bunch without changing the CM energy. A similar effect could be responsible for the change in the wavelength shift. In addition to that, the orbit of the electron beam can be different within the machine for each operation mode. This would lead to a change of angle of observation and thus to a different wavelength shift.

Note, that a tendency of decreasing wavelength shift and decreasing width of the peaks for increasing wavelength tune is observable. The fundamentals of the three spectra have widths of 10±1.3%, 7.2±1.3%, 8.1±1.3% from upper to lower spectrum. The decreasing width cannot be attributed to a known effect so far.

To understand the nature of the additional peaks, their width is compared with the fundamental in the last spectrum of figure 60. In figure 61 the additional

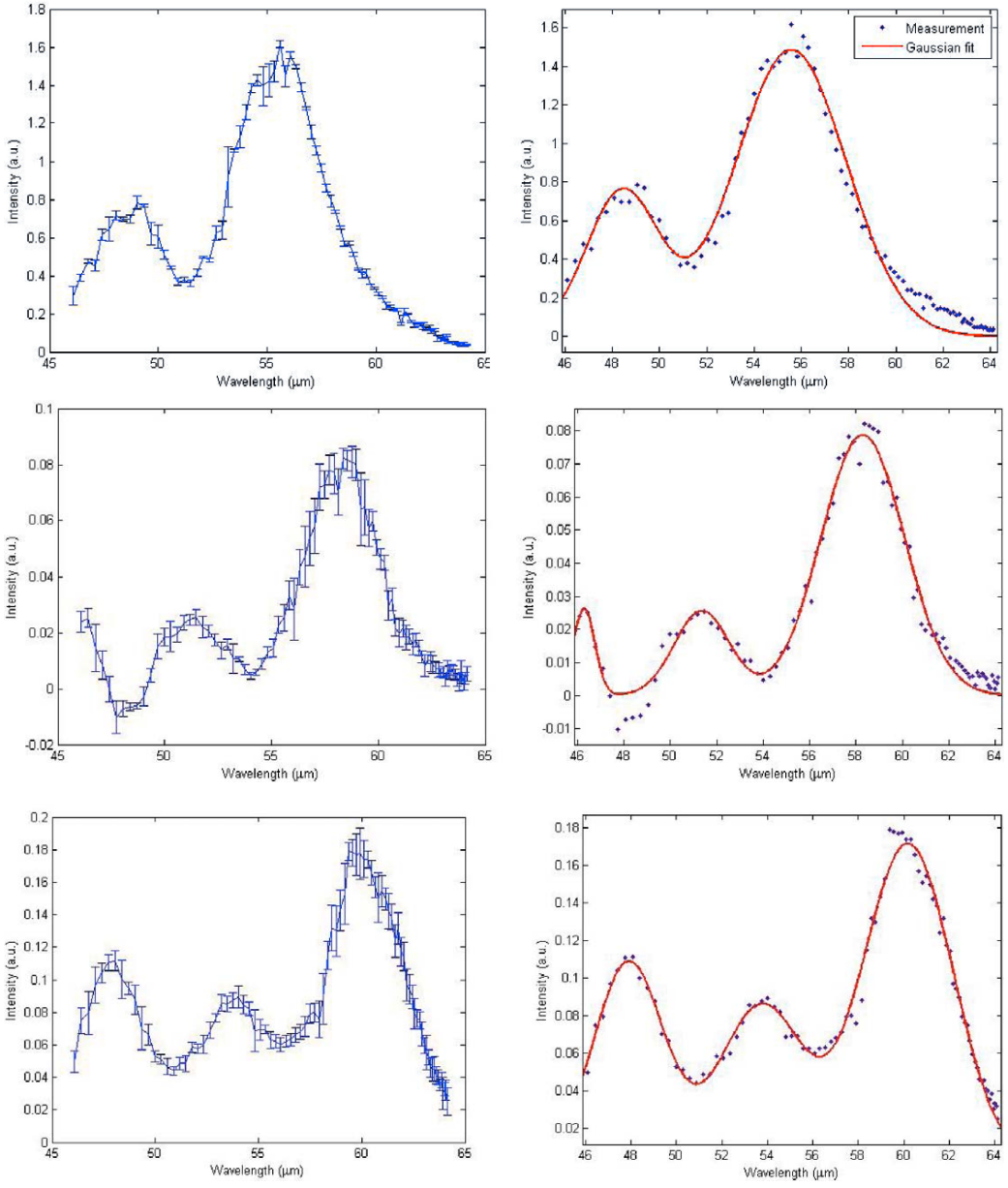

Figure 60: Spectra recorded for Undulator 50, 52.5 and 55 μm tuning and FEL working in SASE-mode with a CM electron energy of 699 MeV.

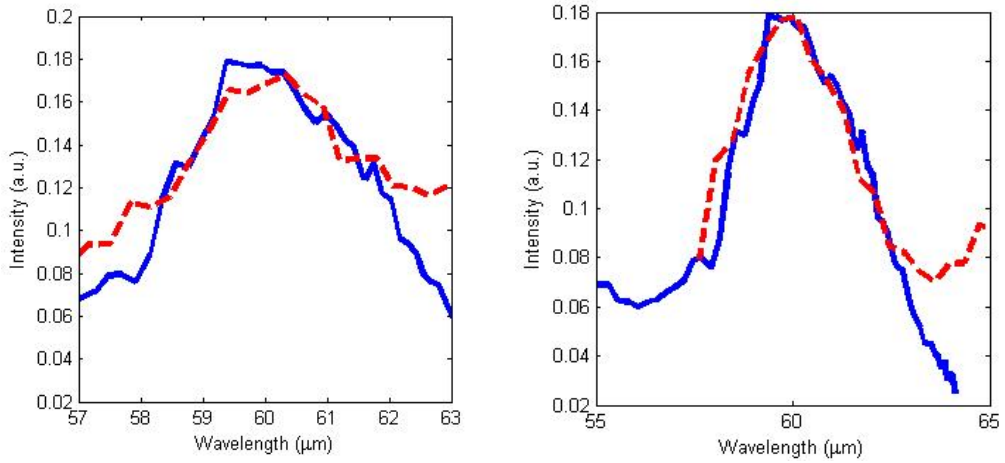

Figure 61: Comparison of different peaks. a) second peak is scaled to the position and height of fundamental. The width is the same. b) The third peak is scaled to the fundamental. The dashed line is the scaled additional peak whereas the solid line shows the fundamental.

peaks are scaled so that their peak value match the wavelength and intensity of the fundamental. As one can see, both peaks have a similar width as the fundamental of the undulator spectrum. This is confirmed by the comparison of the one-sigma-widths of the three Gaussians of the fit, which are all the same within the statistical accuracy.

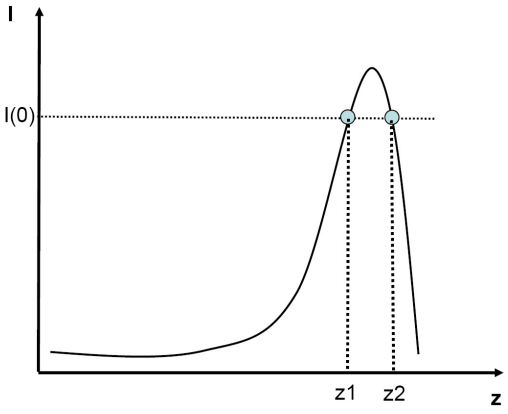

Figure 62: Sketch of bunch shape as a plot of current versus longitudinal position. Two possible regions of emission with same peak current but different energy.

Currently, two possible explanations are under discussion. On the one hand, several energies could occur simultaneously within the bunch and lead to multiple peaks in the coherent spectrum. On the other hand, the spectrometer is a scanning spectrometer and thus the different peaks could be due to discrete successive jumps in energy.

The first implies different regions of emission within the bunch. This means,

the lasing is not initiated by the peak of the bunch head but by two or more parts with the same contribution to the coherent spectrum (see figure 62). In the FEL process, this is due to the dependence of the matching not only on peak current but also on the emittance matching the optics of the FEL. The lasing-regions have different energy which leads to different wavelengths in the spectrum. This effect is actually sometimes observable in the FEL spectrum [44]. The infrared spectrum, however, does not depend on the emittance of the beam. The longitudinal form factor of the bunch, which is responsible for the coherent radiation, is not affected by transverse effects within the wavelength range investigated in this thesis.

Assuming that there are two regions in the bunch head emitting coherent radiation, the distance of approximately 10% between two peaks as seen in figure 60 leads to a difference in energy of approximately 5%. The collimator in front of the FEL has an acceptance of $\pm 3\%$ from CM energy. Therefore, the third peak appearing with fundamental moving towards longer wavelengths cannot be explained within this construction.

The second explanation, that the spectrometer cannot distinguish between simultaneously existing peaks or a discrete fluctuation of the position of the fundamental can have various origins:

- Discrete variations of the gradients within the acceleration modules due to variations within the power provided by the klystrons (the measurements presented in this section were done after re-commissioning of the last klystron providing the power for the last three accelerator modules).
- Artefacts produced within the experimental setup.
- Structures in the bunch shape which leads to such a spectrum.

For a further analysis of the additional peaks, the dependency on acceleration phase of the first accelerator module was measured. Figure 63 shows the reference spectrum with undulator tuned to 36 µm and a machine operated under SASE conditions with an CM electron energy of 696 MeV. As before, the spectrum was corrected for grating efficiency, detector response and background radiation. The main peak occurs at $(40.6 \pm 0.1(\pm 0.3))$ µm, the central peak at $(36.2 \pm 0.4(\pm 0.3))$ µm and the last one at $(32 \pm 0.4(\pm 0.4))$ µm.

The phase of the accelerating field determines the bunch compression. In figure 64 two plots show the dependence of the spectrum on acceleration phase. The background is not subtracted in this case, because the dependence of the background on acceleration phase was not measured. The plot on the left hand side shows the reference spectrum from figure 63 with the highest intensity in average. It looks different due to missing background subtraction. The two curves underneath are spectra recorded with increasing phase. Being one degree away

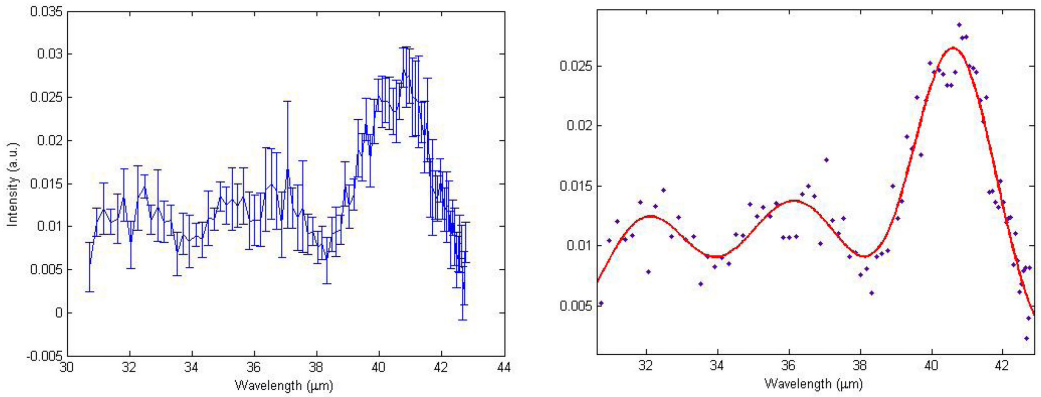

Figure 63: Spectra taken for undulator tuned to 36 µm. Machine was operating in SASE mode with an electron CM energy of 696 MeV. The same peak structure as for 55 µm can be observed.

from the SASE phase towards more compression, the peak intensity increases and the additional peaks are not noticeable anymore. Being 0.5 degree towards more compression (middle curve), the second peak and the fundamental are of similar amplitude, whereas the third peak is hard to detect. At the right hand side the same procedure was done in the other direction. Now, less compression leads to a decrease of intensity. The additional peaks seem to disappear, but the background is visible by the increasing flank towards shorter wavelengths and this could overlap the additional peaks.

The dependence of the additional peaks on the phase of the first accelerator module excludes the experimental setup as possible origin.

Another parameter is the charge of the bunch. In figure 65, spectra taken with charges of 0.5 nC and 1 nC are presented in a combined plot. The lasing process had its optimum at a charge of 0.6 nC. For the whole spectrum a broadening of the peaks is observable for lower charge and the position of the second peak seems to be dependent on the charge. Even though more intensity is observed for the case of 1 nC, the shape and factor of intensity growth do not follow a simple dependence on the charge. In practice, the altering charge changes the complete starting conditions within the gun. In the gun, the counteracting effects like acceleration, having a focusing effect on the electron bunch, and space charge effects are balanced (see section 1.1.1). By changing the charge, this balance is not achieved anymore without changing the parameters of the gun elements.

The spectrum in figure 59 was taken under the same conditions as the spectra in figure 60. Interestingly, no additional peak occurs. Possibly, it is dependent on the correlation with the SASE fluctuation, which was found out to be strong for wavelength larger than 30 µm and not existent for a tuned wavelength of 11.5 µm.

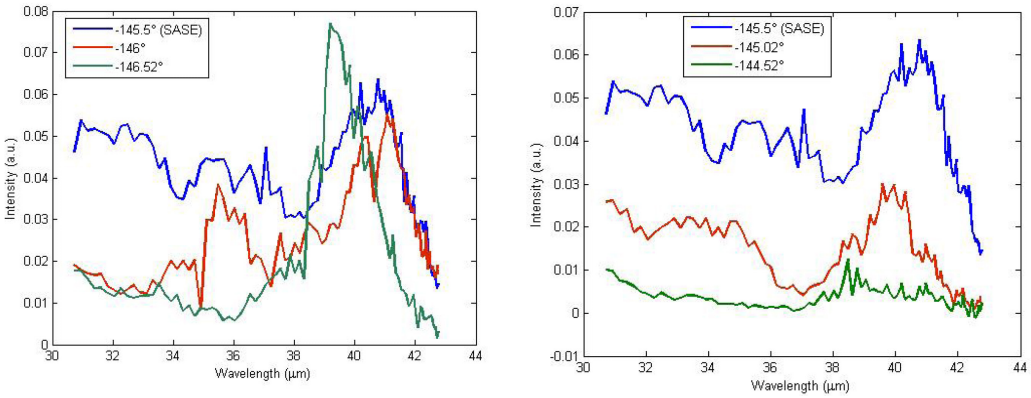

Figure 64: Lhs: Phase of first accelerator module is changed in two steps towards more compression. Rhs: Same procedure towards less compression.

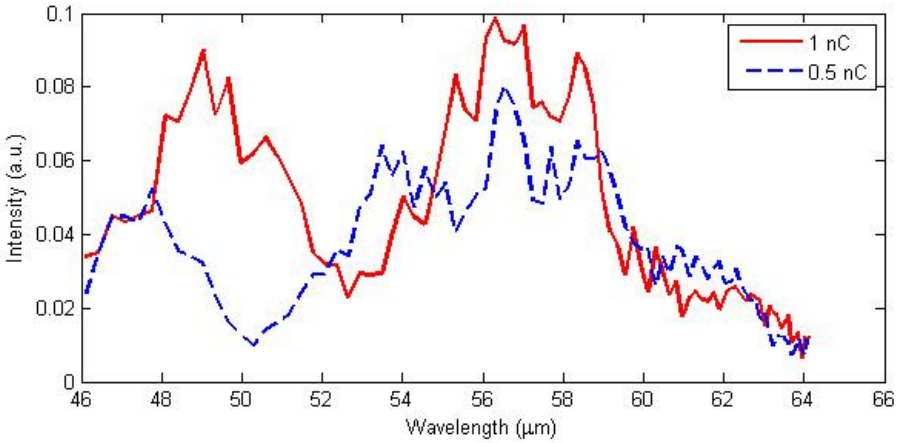

Figure 65: Spectra recorded for 0.5 nC (dashed line) and 1 nC (solid line).

To conclude, additional peaks occurred during shifts with an electron energy of 700 MeV and the machine operated in the SASE mode. So far, it was not successful to reproduce these spectra in a second study block, because technical problems prevented normal SASE operation. Therefore, it is not sure, if these peaks are really an effect connected to the lasing process or if they depend on other parameters of the machine. One possible unique circumstance of the machine status at the time, when the multiple peak spectra were taken, is the re-installation of the klystron connected to the last three accelerator modules.

However, it is the first time, that coherent spectra were taken behind the FEL undulators. The structure of the bunch could be very different to what is expected due to the high peak current needed for the lasing process. The infrared spectrum is sensitive to structures, which do not lase but radiate coherently by emitting spontaneous undulator radiation. From latest measurements at the transverse deflecting cavity at FLASH, situated in front of the FEL undulators, it is known, that due to the over-compression in the two bunch compressors fractions of the bunch with different energies overlap at the same longitudinal position [45]. The energy spread is about 1% from CM energy with the highest energy gradient in the head of the bunch. Over the length of the drift space to the FEL and the path within the FEL undulators the energy spread broadens due to longitudinal space charge effects and CSR which are particularly strong in the high current region [45, 46].

4.2.4 Full scan

A complete spectrum has been taken at 140 µm tune. To get absolute units, the intensity has to be corrected, in addition to the detector response and grating efficiency, with the transmission curve of the diamond window, the transmission of the polarizer (see Appendix C) and the resolution function of the spectrometer. The complete scan was made with different gratings which leads to gaps in the spectrum as their ranges do not overlap (see figure 66).

The spectrum shows a background increasing towards short wavelengths. The fundamental is not visible on that scale. The spectrum is presented in units of µJ/µm. In order to determine the energy content of a harmonic, one has to integrate over its wavelength range limited by the two intersections with the baseline. The energy content of the baseline has to be subtracted for an adequate energy determination.

Figure 67 shows the same spectrum as in figure 66 divided into sections determined by the grating ranges. The vertical scale is different for each of them. With a Gaussian fit the fundamental is found to be at a wavelength of $(151.8 \pm 0.9 \pm 1.1)$ µm with an additional second peak at $(131.6 \pm 0.9 \pm 1.3)$ µm. The fundamental contains an intensity of 240 ± 74 nJ. Even harmonics are observable in the spectrum as well. The second harmonic is calculated to be at 76 µm and a peak is actually found at a

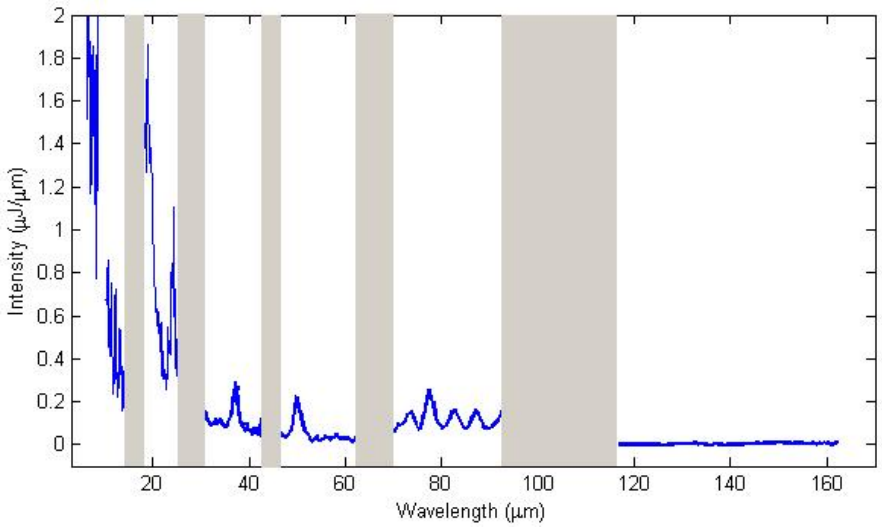

Figure 66: Full spectrum with fundamental at 154 µm. Higher harmonics are visible, whereas the fundamental is too small. A strong background is observable for short wavelengths. Spectrum is recorded with an electron energy of 500 MeV.

wavelength of (77.6±0.7±0.8) µm surrounded by smaller peaks of currently unexplained origin. This peak yields an energy of 270±120 nJ. A clear third harmonic occurs at (50±0.1±0.5) µm with an energy content of 210±130 nJ. Further peaks appear at (37.1±0.1±0.3) µm, which could be the fourth harmonic with a spectral content of 220±330 nJ and at (19±0.4±0.2) µm as possible eighth harmonic of the spectrum.

From undulator theory, only odd harmonics are expected due to a symmetric electric field observed on-axis. Two effects can lead to even harmonics: First, the undulator has only nine periods, increasing the influence of edge field effects. This influence leads to a non-harmonic path of the electrons resulting in even harmonics. Secondly, also the path within the usual magnetic field of the undulator is not harmonic due to field errors and constructive impurities. But simulations including edge effects show only a very weak second harmonic, higher even harmonics could not be reproduced at all [42]. Thus, the existence of such strong even harmonics are currently not understood. In the section of the spectrum between 10 and 14 µm, several peaks appear with no prominent one. This phenomenon is not well understood, either. A reproduction of this structure and a further investigation is necessary.

The fact that the fundamental contains the same energy than the higher harmonics is not expected. But note that no corrections for the beamline transmission are considered in the spectrum. Even though an exact transmission calculation for

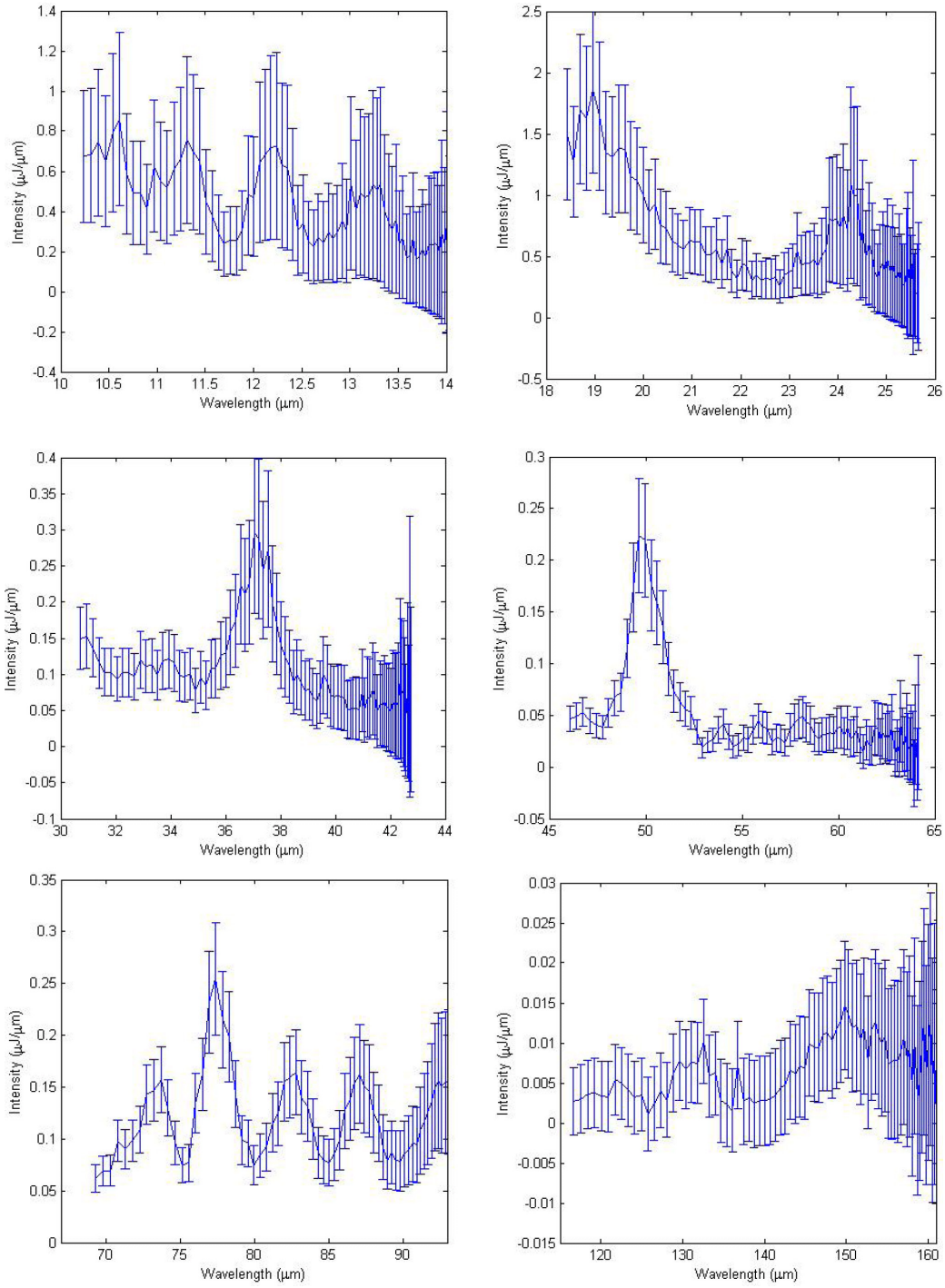

Figure 67: The full spectrum divided into sections determined by the gratings. The vertical scale varies for each spectrum.

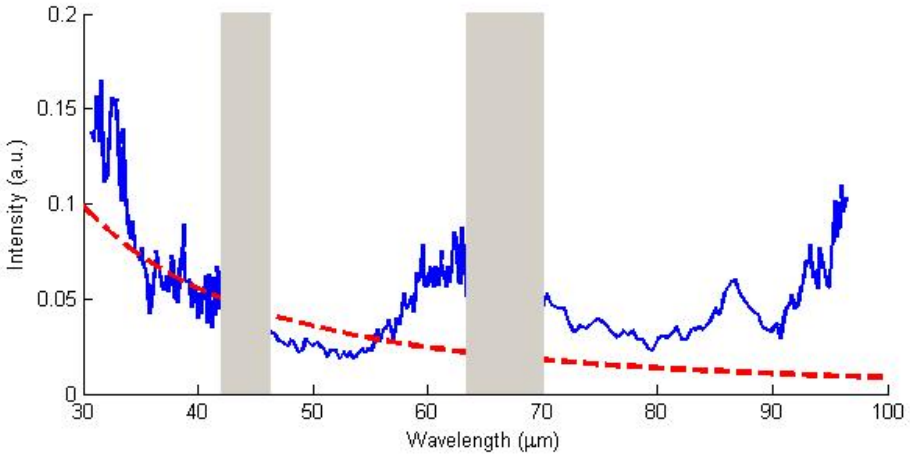

Figure 68: Background measured for three different gratings. Undulator at zero current, CMS electron energy at 682 MeV. Additionally, the simulated spectrum of dump magnet for a single electron is plotted (dashed line).

the infrared beamline is currently not available, an estimation of the influence is possible. The dominating aperture of the beamline is the electron pipe of the FEL, which is used by the electrons and the infrared light together until the electrons are dumped. The electron pipe has a diameter of 35 mm and it ends at a distance of approximately 8 m behind the IR undulator. A simulation with simple Gaussian optics show a cut of 24% of the intensity for a wavelength of 151 μm within the aperture. Higher harmonics are not affected within this approach. After the passage of this first aperture, no further cuts are expected, because the infrared beamline is large compared to the beam diameter. Correcting the intensity by this beamline transmission, the spectral energy of the fundamental increases to 300 ± 74 nJ.

4.2.5 Background studies

As seen in figure 66, a background dominating the short wavelength regime occurs in the infrared spectrum. To investigate this background radiation in more detail, spectra with undulator at zero current were taken. Figure 68 shows the background spectrum recorded with three different gratings. The increase towards shorter wavelengths is again clearly observable. A bump around 65 μm and a peak around 30 μm occur.

The shape of the background radiation spectrum seems to be similar to a synchrotron spectrum emitted by an electron beam which is deflected by a bending magnet. A candidate for a bending magnet producing this background is the

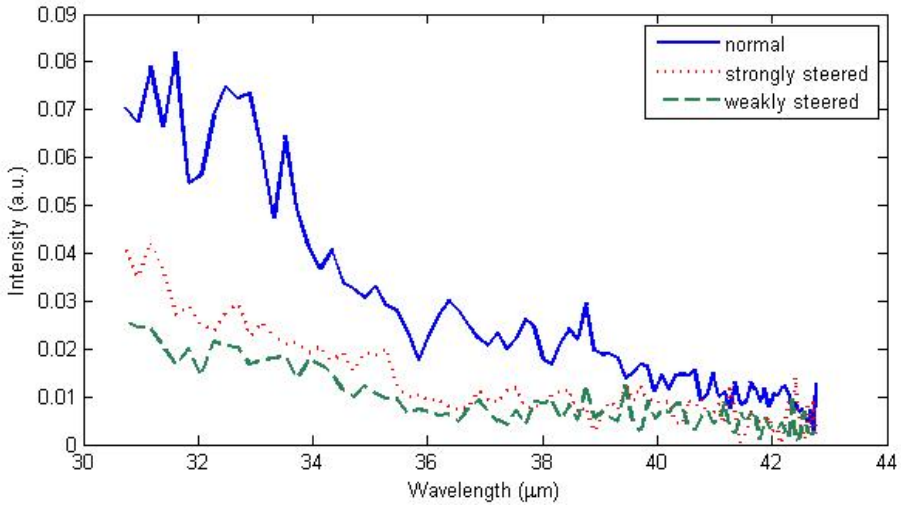

Figure 69: Background spectrum with undulator having zero current. The solid line shows the usual background, the dashed lines the spectrum without radiation from the last dipole magnet.

dipole magnet deflecting the electrons into the dump. For a comparison, a simulated single particle spectrum of the dump magnet is implemented in the plot in figure 68. The spectrum is simulated at the position of the outcoupling mirror, which is assumed to be a square of 60x60 mm and 1.35 m behind the dump magnet. The vertical scale is arbitrary to match the background spectrum. The increase towards short wavelengths is well reproduced with the simulation, whereas the structure on the spectrum can be due to the form factor of the bunch.

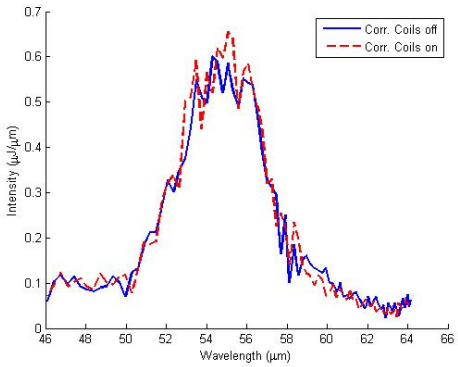

Figure 70: Spectra taken with and without correction coils. Tuned wavelength is 50 µm.

To further test this idea, radiation from the dump magnet was prevented by steering the electron beam into the beam pipe just before the magnet. This was achieved by using the vertical steerer magnets V1 and V3 (see figure 45) in front of the infrared undulator. Both magnets were set to small currents, so the deflection of each magnet is small, but the net deflection is sufficient to dump the electron beam into the beam pipe. Small deflection fields are de-

sirable to reduce synchrotron radiation from the steerer magnets. The background spectra taken with normal conditions and with blocked electron beam are shown in figure 69. To show the effect of strong steering, a spectrum taken with V3 set to a high current is implemented in the plot. Even though the intensity goes down, a contribution of this strong field is observable. For the slightly steered beam, the intensity decreases by a factor of 3 which indicates a high contribution from the last dipole magnet to the background spectrum. A weak background is still left, but this could be from steerer magnets or from radiators within the FEL section.

4.2.6 Influence of correction coils

In addition to machine parameters, undulator settings could also influence the spectrum. As seen in the commissioning phase of the undulator, the correction coils affect the transmission of the electron beam and are set to minimize the field integrals. Figure 70 shows, however, that these coils have no detectable influence on the first harmonic spectrum.

4.3 Beam Profile Measurements

The transverse beam size of the infrared radiation was investigated by scanning the intensity profile. For these profile measurements a x-y scanning device was used. A pyroelectric detector was mounted on two perpendicular linear movers. The undulator was tuned to 50 µm.

This provides the opportunity to compare the simulated profiles with the real beam shapes. The simulated profiles were propagated with Zemax with the initial Gaussian waist taken from figure 33. The simulation was done for a wavelength of 54 µm.

Figure 71 show comparative plots of the simulated and the measured profiles. On the right hand side, the horizontal cross section is presented, on the left the vertical. The waist close to the diamond window (see figure 39 for comparison) results in a large beam at the position of the paraboloid P2. Therefore, this location was chosen for the first comparison (a). The second location is in the middle of the optical setup at the position of M2 (b), the third location is in front of the filter grating, approximately 150 mm behind M4 (c). The intensities of the simulated and measured cross section is scaled so that the two peaks match.

It is noticeable that the profiles match well in the center of the beam, whereas at the edge a broadening of the real profile is observable. At the position (c) the best match can be found. Almost every measured profile shows an asymmetric shape. This is explainable, because the infrared radiation meets the outcoupling mirror P1 at DP3 not concentric. With P1 being a paraboloid, this leads to a deformation of the beam profile. This circumstance has not been concidered within

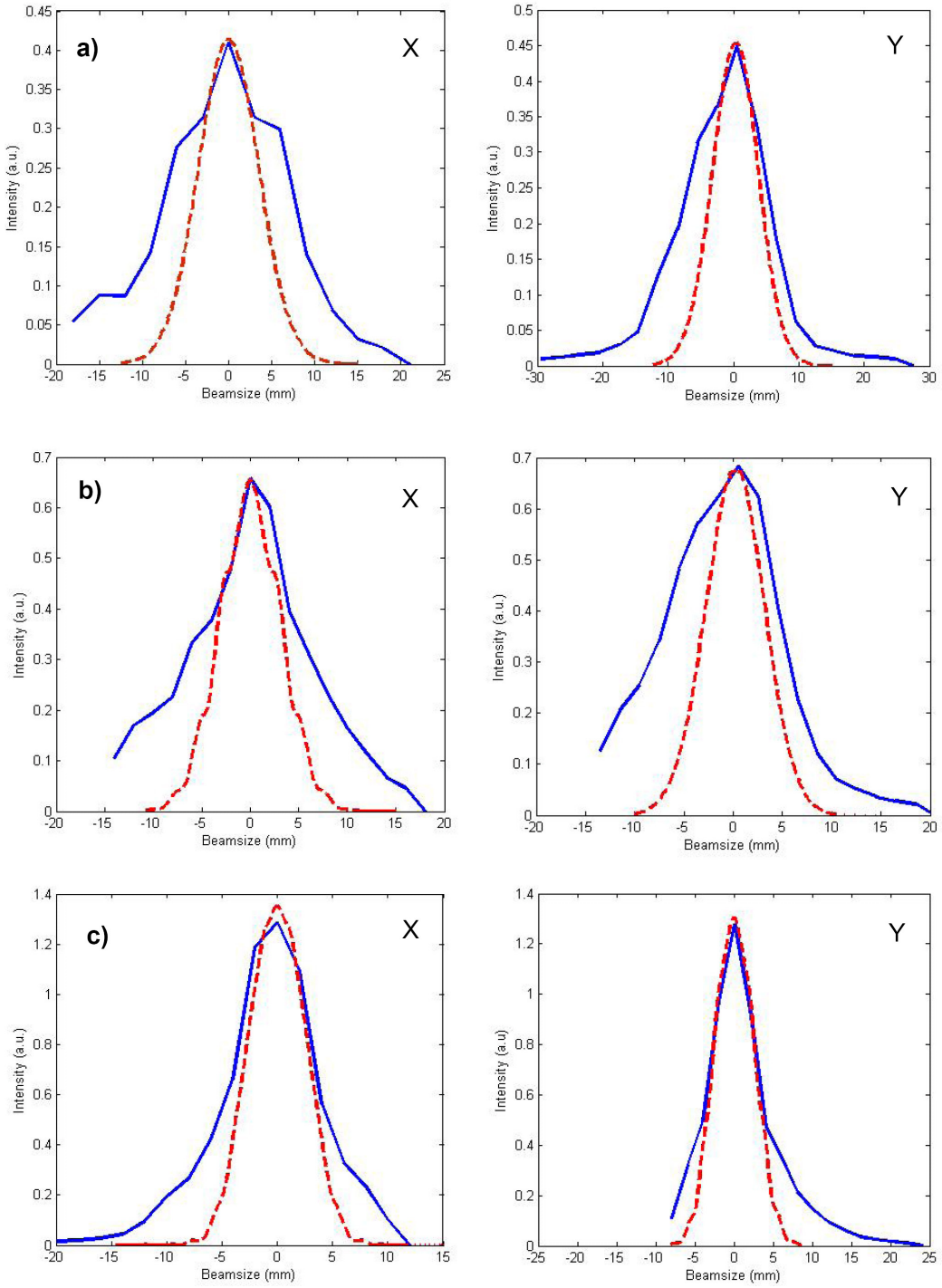

Figure 71: Comparison of simulated (dashed line) and measured (solid line) beam profiles at dedicated locations: a) at the position of P2, b) of M2 and c) at the position of the polarizer (150 mm behind M4). The drawing of the setup can be found in figure 39.

the simulations.

Besides the comparison of beam profiles at dedicated locations, the behavior of the beam during the passage of the optical setup is of high interest, because the requirements of the spectrometer listed in section 3.4 need to be kept. As one can see in figure 71, the requirements are fulfilled by the real profile: First, the beam converges on its way to the spectrometer and secondly, the beam size at the location of the polarizer is approximately 20 mm (corresponding to 2σ), which is below the tolerated maximum of 25 mm. Assuming that this agreement between simulations and real beam profiles occurs also for wavelength below or above a tuned wavelength of 50 µm, the requirements of the spectrometer are fulfilled for the whole wavelength range of the undulator.

5 Conclusion and Outlook

For first investigations into the FLASH infrared undulator as bunch diagnostic tool, a new spectrometer was designed and constructed. The instrument was then integrated in a newly developed experimental station at the third diagnostic port of the infrared beamline in the FLASH experimental hall. The optics design of the experimental setup was compiled with simulations to match the requirements of the diagnostic port and the spectrometer. The whole experimental station has been commishioned successfully.

After the installation of the infrared undulator in the tunnel of FLASH, the commissioning brought forward that the beam pipe was curved which resulted in a large offset of the beam behind the device. With the corrected vacuum chamber, the beam transport through the undulator could be improved; the offset induced by the magnetic field of the undulator is now within the expectations due to the preparative magnetic measurements. An undulator operation program was successfully implemented as a routine which drives the main and correction coils simultaneously. Either a wavelength or a current can be chosen to tune the undulator.

First spectra show a wavelength shift between 8 and 12% dependent on the machine operation status. Because the undulator operation program uses the center-of-mass electron beam energy to calculate the undulator wavelength, a certain wavelength shift is expected. The amount of the shift and its origin is not yet fully understood, however. From the FEL process it is known that the VUV radiation is emitted within the leading peak, which occurs due to the non-linear longitudinal phase space. Becasue the head of the bunch has lower energy than the center-of-mass, this leads to difference of calculated and measured wavelength. The correction factor varies, because the matching into the FEL, regulated by quadrupoles and sextupoles, can alter. Thus, the region of lasing can be changed without influencing the center-of-mass energy. Furher investigations into this explanation need to be done for a complete understanding of the wavelength shift.

In most of the measurement shifts, multiple peaks were observed in the infrared spectra. These peaks have a distance of around 10% from each other and they have the same width as the fundamental. The origin of the additional peaks is currently not understood. Neither discrete machine fluctuations nor intra bunch effects can be excluded. Clear is that no coherent spectra have ever been taken behind the FEL undulators and hence, the shape of the form factor can differ from what is expected from measurements done in front of the FEL section.

The full spectrum with undulator tuned to 140 µm shows a fundamental and strong contributions of higher harmonics. Even though it is not expected, even harmonics are well observable in the spectrum. So far, the occurrence of such strong even harmonics is not explainable. In addition to that, a background dom-

inating the short wavelength regime was measured. Further analysis showed that the origin of this background radiation is the last dipole of the accelerator, which deflects the electron beam into the dump.

Undulator parameters like the correction coils, which have a noticeable effect on the beam transport, do not have any effect on the coherent spectra.

Beam profile scans showed that the real profile differs slightly from the simulated ones especially in the side region. In the beam center a good agreement was found. The requirements of the outcoupling port and the spectrometer were kept by the real infrared beam.

The studies within this thesis led to the conclusion that the spectrum of the new infrared undulator is highly dependent on the machine parameters. The wavelength shift and the additional peaks are not fully understood at the moment. Further studies are necessary to investigate the role of the energy measurement, the quadrupoles and the acceleration modules. In addition, the energy spread within the bunch at the position of the infrared undulator needs to be investigated. If the multiple peak spectra are not reproducible during next study block, the status of the machine during the measurements done for this thesis need further analysis. For an adequate estimation of transported energy, the beamline transmission has to be calculated for several wavelengths. With DP3 being reserved for electron diagnostics from May 2008, a vacuum setup has to substitute the box purged with nitrogen. Higher accuracy and easier handling is expected from this modification.

In the future, the scan setup for intensity measurements should be installed at DP2 in the tunnel. Even though the concentration on intensity studies without spectral analysis is not reasonable yet, first investigations should start as soon as possible. So far, the second diagnostic port is not available which makes the diagnostic port in the experimental hall to the exclusive experimental station for electron beam diagnostics with the FLASH infrared undulator.

A Appendix-
Response measurements of steerer magnets

As one can see in figure 45, there are two steerer pairs in front of the undulator situated one and three meters behind the FEL. The steerer pair placed behind the IR undulator is 10m away. To get an idea of the effect of the steerer magnets on the beam, the BPM positions for different steerer currents were measured.
Figure 72 shows the response measurements for the steerer magnets H1 and V1.

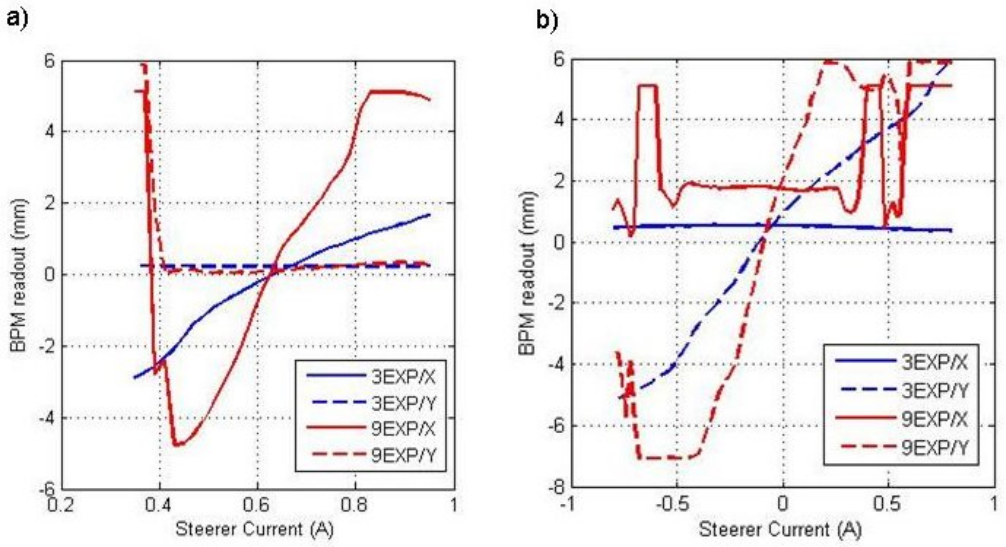

Figure 72: Response measurement of steerer pair H1 (a) and V1 (b). Horizontal and vertical dislocation is measured with BPM 3EXP and 9EXP.

The effect of the steerers can be observed on BPM3EXP in front of the undulator and BPM9EXP behind it. A calibrated BPM only gives an adequate position of the beam within the linear range of the instrument. The response of H1 is horizontally linear on BPM 3EXP due to moderate movement, BPM 9EXP, however, shows only a linear signal between approximately 0.43 and 0.82 A. Below and above this range, the position exceeds the linear limit and thus, no adequate read out can be achieved. If the beam leaves the displayable range of the BPM, the vertical read out is also not reliable anymore. Within the linear range, the vertical positions remains constant. For the response of V3, the vertical positions shows a linear range, in which the horizontal positions remain constant.

In figure 73, the response measurements of H3/V3 are presented. Reasonable results are only given by the BPM 9EXP behind the undulator.Again, only the linear range has to be taken into consideration.

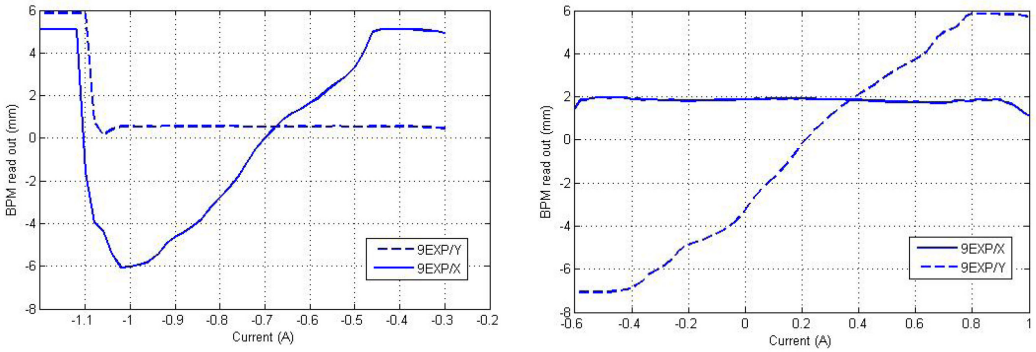

Figure 73: Response measurement for steerer pair H3/V3.

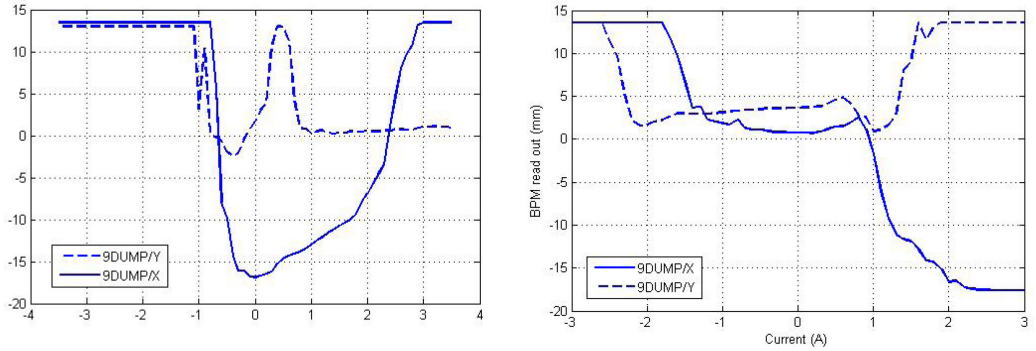

Figure 74: Response measurement of H10/V10. Displacement is measured with BPM in the Dump region. This BPM do not work adequately.

The response measurement for the last steerer pair H10/V10 did not lead to adequate results, because due to the position of these steerers only the BPM in the dump region is usable. This BPM did not work properly, as one can see in figure 74.

B Appendix- Magnetic field measurements of undulator coils

As an online tool, a Hall probe is installed at the IR undulator. It is mounted at the third coil on the side, where the electrons enter the device. It is installed for a quick check if problems occur during operation. In figure 75, the magnetic field produced by the main current is presented. Figures 76, 77 and 78 show the measurements of the correction coils. In figure 78 the influence of the position of the hall probe becomes obvious: the magnetic field measured in the gap of the main correction coils would be the same for both sides of the undulator, whereas now the right side is closer to the actual position of the hall probe than the left one. Thus, the difference of the magnetic field curves are an artifact.

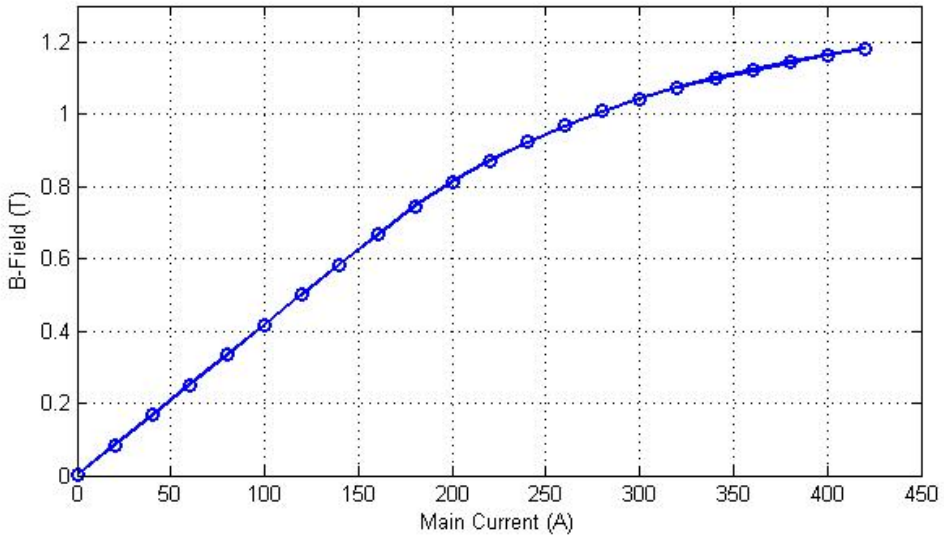

Figure 75: Magnetic field for main coils.

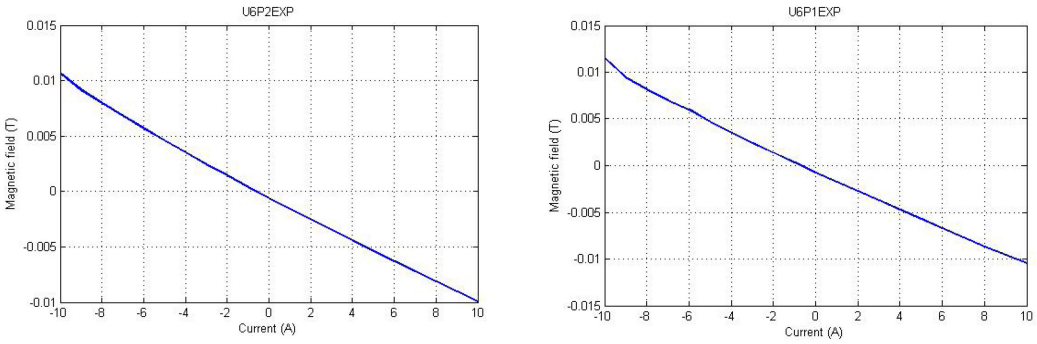

Figure 76: Magnetic field measurement for correction coils at the front end of the undulator, where the beam enters the device.

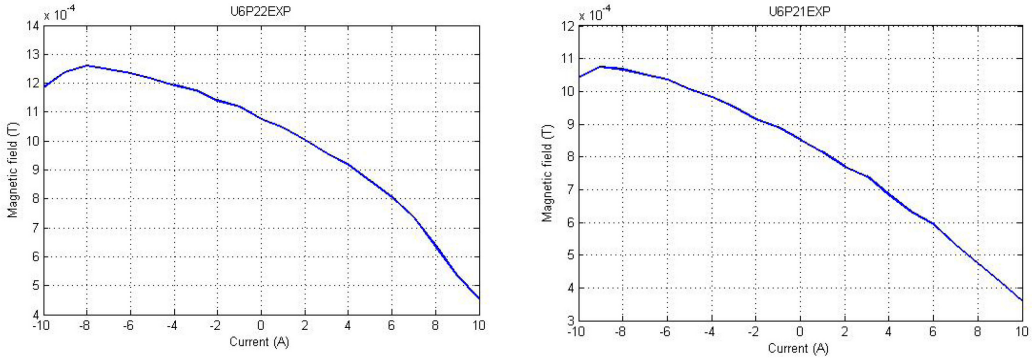

Figure 77: Magnetic field measurement for correction coils at the end of the undulator, where the electrons leave the device.

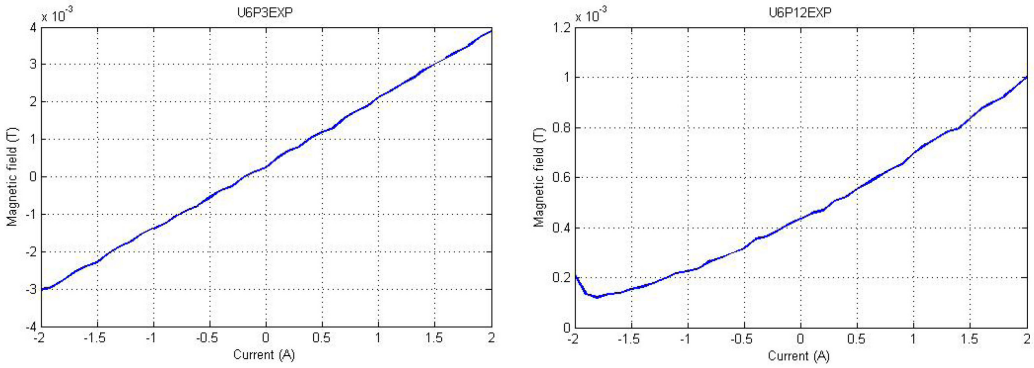

Figure 78: Magnetic field measurement for the main correction coils.

C Appendix- Transmission curve of polarizer P03

The usual polarizer used in the experimental setup (G30) has a good transmission down to 35 µm. Below this, a special polarizer has to be installed (P03). Its transmission for the electric field component perpendicular to the wires is given in figure 79.

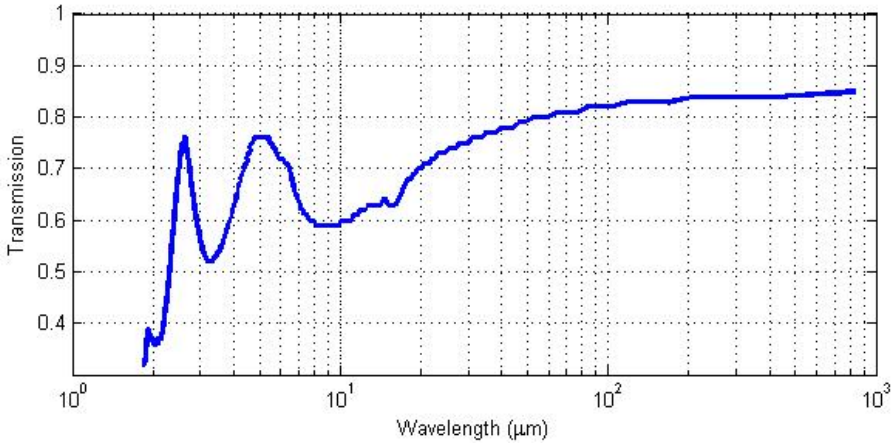

Figure 79: Transmission curve of polarizer P03, which was used for spectra reaching into the short wavelength regime. The transmission is valid for the field component perpendicular to the wire.

References

[1] Donald H. Perkins, *Hochenergiephysik*, Addison-Wesley (1991).

[2] J. Rossbach, *Linac based Free-Electron Laser*, TESLA-FEL Report **2004-08** (Hamburg, 2004).

[3] V. Ayvazyan et. al., *A new powerful Source for coherent VUV Radiation: Demonstration of exponential growth and saturation at the TTF FEL*, The European Physical Journal D - Volume **20**, Number **1** (2002).

[4] S. Schreiber, *FLASH*, Talk within FLASH Tutorial (2007), http://flash.desy.de/e409/e2219/e2224/flash-overview-cp.pdf.

[5] K. Honkavaara et. al., *Bunch Length Measurements at TTF with a Streak Camera*, TESLA-Report **2000-38** (2000).

[6] M. Hüning, *Analysis of Surface Roughness Wake Fields and Longitudinal Phase Space in a Linear Electron Accelerator*, DESY-THESIS **2002-029** (Hamburg, 2002).

[7] L. Fröhlich, *Bunch Length Measurements Using a Martin-Puplett Interferometer at the VUV-FEL*, TESLA-FEL Report **2005-02** (Hamburg, 2005).

[8] S. Casalbuoni et. al., *Far-Infrared Transition and Diffraction Radiation, PartII: The THz Beamline at the VUV-FEL Linac*, TESLA-FEL Report **2006-04** (2006).

[9] O. Grimm, *Coherent Radiation Diagnostics for Short Bunches*, in *Proceedings of PAC 2007* (New Mexico - USA, 2007), p. 2653-2657.

[10] V. Borisov et. al., *Simulation of Electromagnetic Undulator for Far Infrared Coherent Source of TTF at DESY*, in *Proceedings of EPAC 2006* (Edinburgh 2006), p. 3595-3597.

[11] H. Delsim-Hashemi et. al., *Broadband Single Shot Spectrometer*, in *Proceedings of the 27th International FEL Conference 2005* (Stanford, 2005).

[12] S. Schreiber et. al., *The Injector of the VUV-FEL at DESY*, in *Proceedings of 27th International FEL Conference* (Stanford, 2005), p. 545-548.

[13] S. Schreiber et. al., *Properties of Cathodes used in the Photoinjector RF Gun at the DESY VUV-FEL*, in *Proceedings of EPAC 2004* (Lucerne-Switzerland, 2004), p. 348-350.

[14] T. Limberg, *Design and Performance simulation of the TTF-FEL II Bunch Compression System*, in *Proceedings of EPAC 2002* (Paris-France, 2002), p. 811-813.

[15] R. Brinkmann et. al., *Tesla Technical Design Report, Part II: The Accelerator* (Hamburg, March 2001).

[16] Y. Kim, *Commissioning of TTF2 Bunch Compressors for generation of 20 femtosecond SASE Source*, in *Proceedings of the 27th International FEL Conference 2005* (Stanford, 2005).

[17] A. Kabel et. al., *Bunch Compressor II at the TESLA Test Facility*, in *Proceedings of the PAC 1999* (New York, 1999).

[18] A. Loulergue, *A simple S-chicane for the final Bunch Compressor of TTF-FEL*, in *Proceedings of EPAC 2000* (Vienna, 2000).

[19] A. Bolzmann, *Investigation of the longitudinal charge distribution of electron bunches at the VUV-FEL using the transverse deflecting cavity LOLA*, Diploma-Thesis (Hamburg, 2005).

[20] B.Beutner et. al., *Beam Dynamics Experiments and Analysis on CSR Effects at FLASH*, in *Proceedings of FEL 2006* (Berlin, 2006).

[21] O. Grimm, P. Schmüser, *Principles of Longitudinal Beam Diagnostics with coherent Radiation*, TESLA-FEL Report **2006-03** (Hamburg, 2006).

[22] J. Menzel, *THz-Spektroskopie zur Bunch-Längenmessung an der TESLA-Testanlage TTF*, Diss. (Hamburg, 2005).

[23] J.D. Jackson, *Classical electrodynamics*, John Wiley & Sons, Inc.- third edition (1998).

[24] F. Löhl et. al., *Measurements of the transverse emittance at the FLASH injector at DESY*, in *Physical Review Special Topics - Accelerators and Beam* **9/092802** (2006).

[25] B.M. Bolotovsky, E.A. Galst'yan, *Diffraction and diffraction radiation*, in *Phys. Usp.* **43** (2000), p. 755-775.

[26] Hideo Onuki et. al., *Undulators, Wigglers and their Applications*, Taylor and Francis (2003).

[27] J. Rossbach, *Beschleunigerphysik II*, Lecture at University of Hamburg (2005).

[28] K. Wille, *Physik der Teilchenbeschleuniger und Synchrotronstrahlungsquellen*, Teubner Studienbücher (1996).

[29] G. Geloni et. al., *Fourier Optics Treatment of Classical Relativistic Electrodynamics*, DESY-Report **06-127** (Hamburg, 2006).

[30] G. Geloni et. al., *A Method for Ultrashort Electron Pulse Shape-Measurement Using Coherent Synchrotron Radiation*, DESY-Report **03-031** (Hamburg, 2003).

[31] A. Alfeev et. al., *Simulations of Hamburg University Undulator for Far Infrared Coherent Source*, Internal Report (Dubna, 2005).

[32] O. Grimm et. al., *Magnetic measurements with the FLASH infrared undulator*, TESLA-FEL Report **2007-08** (2007).

[33] D. Meschede, *Gerthsen Physik*, Spinger-Verlag 21. Auflage (2002).

[34] S. Cunovic et. al., *Konzept für pump-probe Experimente mit synchronisierten Laser- und VUV-Fel Pulsen*, http://www.physik.uni-kiel.de/kfn/sni2006/Programm/Abstract.php?id=272 (2006).

[35] U. Fruehling, *Arbeitsbericht über den Zeitraum vom 01.10.2005 - 11.06.2007*, internal paper (Hamburg, 2006).

[36] M. Gensch et. al., *New infrared undulator beamline at FLASH*, Infrared Phys. Techn. (2008).

[37] Calculation done by H. Delsim-Hashemi, Desy (2008).

[38] Paul F. Goldsmith, *Quasioptical Systems*, IEEE Press Marketing (1998).

[39] G. Geloni et. al., *Fourier treatment of near synchrotron radiation theory*, Optics Communication **276 167-179** (2007).

[40] *www.zemax.com*

[41] *Zemax User's Guide*, Zemax Development Corporation, San Diego.

[42] O. Grimm, *personal communication*.

[43] C. Gerth, *personal communication*.

[44] R. Treusch, *personal communication*.

[45] M. Röhrs, *Investigation of the Phase Space Distribution of Electron Bunches at the FLASH-Linac Using a Transverse Deflecting Structure*, PhD Thesis, *to be published*.

[46] H. Schlarb, *personal communication*.

[47] J. Feldhaus et. al., *The Infrared Undulator Project at the VUV-FEL*, in *Proceedings of the 27th International Free Electron Laser Conference* (Stanford, 2005), p. 183-186.

[48] V. Ayvazyan et. al., *First operation of a free-electron laser generating GW power radiation at 32nm wavelength*, The Europ. Phys. Journal **D 37** (2006), p. 297-303.

[49] W. Ackermann et. al., *Operation of a free electron laser from the extreme ultraviolet to the water window*, Nature Photonics **Vol. 1/No. 6** (June 2007)

[50] H. Delsim-Hashemi, *personal communication*.

[51] M. A. Geitz, *Investigation of the transverse and longitudinal Beam Parameters at the TESLA Test Facility Linac*, DESY-Thesis **1999-033** (November 1999).

[52] M. Castellano et. al., *6-D Electron Beam Characterisation using Optical Transition Radiation and Coherent Diffraction Radiation*, in *Proceedings DIPAC 2001* (Grenoble 2001), p. 46-50.

Acknowledgments

First of all, I would like to thank Prof. Dr. Jörg Rossbach for providing the opportunity to work on an interesting topic with an emphasis on experimental physics. I am very grateful for the support and especially for the possibility to attend the Cern Accelerator School.

Above all, I want to express my gratitude to Dr. Oliver Grimm, who has avoided no trouble and effort to support me with my thesis. The work with him was distinguished by team spirit and mutual support and his door was always open, whenever a question or a problem occurred. I also want to thank him for his patience during the final stage of this thesis. His fruitful ideas and support substantially contributed to the outcome of this work.

I also would like to thank Dr. Bernhard Schmidt and Hossein Delsim-Hashemi for the aid and encouragement during my time at DESY. Especially the design and operation of the spectrometer would not have been that successful without their help and expertise. A special thank to Stephan Wesch and Christopher Behrens who helped me during the test measurements in the lab.

Furthermore, I am indebted to Dr. Katja Honkavaara whose honest review of my thesis gave important impulses which lead to an improvement of the whole structure of the thesis. Additionally, I would like to thank Ulrike Frühling for her introduction into Zemax and her patient support during the first months of my work at DESY.

At this point, one should not forget the important work of our constructing engineers and mechanicians. I am thankful to had the opportunity to work with Otto Peters, whose experience and creativity contributed to the design and construction of the experimental station in the experimental hall. In addition, I want to thank Bernd Beyer for the harmonic collaboration during the construction phase of the spectrometer.

For fruitful discussions I want to thank (aside the people mentioned above) Dr. Evgueni Saldin, Dr. Rolf Treusch, Dr. Christopher Gerth, Dr. Bolko Beutner, Prof. Dr. Peter Schmüser, Dr. Siegfried Schreiber, Dr. Michael Gensch and Lars Fröhlich.

Finally, I want to thank the complete FLASH crew for the great acceptance in the team and for the effort to operate the machine.

With this thesis my time as a student comes to an end. Thus, this is also the point in time to thank all the people supported me in the last five years. Most importantly, there is my mum, Irmgard Willner, who always encouraged me to enjoy my time as a student even though the studies in physics were sometimes hard and very time consuming. And there is my dad Ulrich Schäler, to whom this

work is dedicated, because he made my studies in Germany and Berkeley possible with his financial and mental support. He never dictated conditions connected to his contribution, but trusted all my decisions concerning the studies and life. I am very grateful for this absolute confidence.

Many thanks also to my brother, Roland Willner, who never missed a joke about physics and physicists but was always at my side, when the studies had their tough times. I also would like to express my appreciation to my friends, who have not seen me much the last months but anyhow gave me moral and mental support.